

Measurements of fluid flow in weld pools

PROEFSCHRIFT

ter verkrijging van de graad van doctor
aan de Technische Universiteit Delft,
op gezag van de Rector Magnificus prof.ir. K.C.A.M. Luyben
voorzitter van het College voor Promoties,
in het openbaar te verdedigen op dinsdag 3 mei 2011 om 15:00 uur

door

Chuangxin ZHAO

Master of Engineering in Guangzhou Institute of Energy Conversion,
Chinese Academy of Sciences, Guangzhou, China
geboren te Shangdu, Nei Mongol, China.

Dit proefschrift is goedgekeurd door de promotor:

Prof. dr. I.M.Richardson

Samenstelling promotiecommissie:

Rector Magnificus, voorzitter

Prof. dr. I.M. Richardson, Technische Universiteit Delft, promotor

Prof. dr. ir. C.R. Kleijn, Technische Universiteit Delft

Prof.dr. J.S. Smith, University of Liverpool

Prof.dr. ir. A.J. Huis In 't Veld, Universiteit Twente

Prof.dr. D.G. Eskin, Brunel University

Dr. F. Roger, ENSTA ParisTech

Dr. R.P.J. Duursma, Tata Steel

Measurements of fluid flow in weld pools

C.X. Zhao

PhD thesis of Delft University of Technology-with summary in Dutch

ISBN 978-90-77172-7-11

Keywords: Experiments, Weld pool, Visualization, Fluid flow

Copyright @ 2009 Chapter 4 by the American Physical Society

Copyright @ 2010 Chapter 5 by Elsevier

Copyright @ 2011 for the remaining chapters by C.X. Zhao

All rights reserved. No part of the material protected by this copyright notice may be reproduced or utilized in any form or by any means, electronic or mechanical including photocopying, recording, or by any information storage and retrieval system, without written permission from the author.

Printed in The Netherlands

CONTENTS

1	INTRODUCTION.....	1
2	BACKGROUND	5
2.1	FLOW PATTERNS AND THEIR DRIVING SOURCES	5
2.1.1	<i>The driving forces.....</i>	5
2.1.2	<i>Flow patterns.....</i>	6
2.2	CURRENT METHODS FOR STUDYING FLUID FLOW IN WELDING.....	9
2.2.1	<i>Experimental observations</i>	9
	Surface flow	9
	Internal flow	10
	Weld pool shape measurement	12
	3D measurement.....	13
2.2.2	<i>Numerical simulations.....</i>	14
	Weld pool free surface.....	15
	Laminar flow and Turbulent flow model	15
	Estimation of order of maximum velocity in the weld pool	15
2.3	PHYSICAL MODELING	16
2.3.1	<i>Some dimensionless numbers describing fluid flow</i>	16
	The Grashof number.....	16
	The Magnetic Reynolds number.....	17
	The Marangoni number	17
	Peclet number	17
	Bond number	18
	Prandtl number	18
2.3.2	<i>The physical model of Limmaneevichitr and Kou</i>	19
	Materials.....	19
	Apparatus	19
	Flow visualization	19
	Surface-active agent	19

2.4	SUMMARY	20
3	TWO DIMENSIONAL VELOCITY MEASUREMENTS	23
3.1	PIV (PARTICLE IMAGE VELOCIMETRY) AND ITS PRINCIPLE	23
3.1.1	<i>PIV introduction</i>	23
3.2	APPLICATIONS IN WELDING	24
3.2.1	<i>Experiment system arrangement</i>	24
3.2.2	<i>PIV calculation</i>	25
3.2.3	<i>A simple analyses for surface particle flow</i>	27
3.3	MEASURED CASE I, RESULTS AND DISCUSSION	29
3.3.1	<i>Effects of the natural oxide layer</i>	29
3.3.2	<i>Different interrogation windows used in PIV</i>	30
3.3.3	<i>Flow motion and velocity fields</i>	32
3.3.4	<i>Vortex forming and development</i>	35
3.3.5	<i>Discussion</i>	36
	Flow patterns	36
	Reynolds number	36
	Maximum velocity	37
3.4	MEASURED CASE II, RESULTS AND DISCUSSION	38
3.4.1	<i>Computational zone</i>	38
3.4.2	<i>Mesh selection</i>	39
3.4.3	<i>Flow instability</i>	42
3.4.4	<i>Flow motion and velocity field</i>	43
	Clockwise vortex	43
	Counter clockwise vortex	43
	Symmetrical flow	43
3.4.5	<i>Maximum velocity in the computational zone</i>	47
3.4.6	<i>Discussion</i>	47
	Surfactant effect	47
	Flow motions	48
	Interfacial phenomena	49
3.5	CONCLUSION	51

4	THREE DIMENSIONAL VELOCITY MEASUREMENTS	53
4.1	MEASUREMENT DESCRIPTION	54
4.1.1	<i>Experimental arrangement.....</i>	<i>54</i>
4.1.2	<i>Structure of the stereo adapter</i>	<i>55</i>
4.1.3	<i>Geometric relationship between the image and spacial coordinate systems.....</i>	<i>55</i>
4.1.4	<i>Stereo point reconstruction.....</i>	<i>58</i>
4.2	3D RECONSTRUCTION	58
4.2.1	<i>Calibration</i>	<i>58</i>
4.2.2	<i>Match and Correspondence.....</i>	<i>59</i>
4.3	RESULTS AND DISCUSSION	61
4.3.1	<i>Error analysis.....</i>	<i>61</i>
4.3.2	<i>Two and three dimensional velocity (measured case).....</i>	<i>63</i>
4.3.3	<i>Weld pool surface inclination and accuracy analysis.....</i>	<i>67</i>
4.4	SUMMARY AND CONCLUSION	68
5	OXYGEN ACTIVE AND TRANSITIONAL FLOW	71
5.1	INTRODUCTION	71
5.2	EXPERIMENTAL ARRANGEMENT	71
5.2.1	<i>Experimental system.....</i>	<i>71</i>
5.2.2	<i>EPMA oxygen concentration measurement</i>	<i>71</i>
5.3	RESULTS.....	74
5.3.1	<i>Observed flow bahaviour</i>	<i>74</i>
5.3.2	<i>Interface instability.....</i>	<i>76</i>
5.3.3	<i>Oxygen influences.....</i>	<i>78</i>
5.3.4	<i>Oxidation and oxygen distribution</i>	<i>80</i>
5.4	ANALYSIS AND DISCUSSION	84
5.4.1	<i>Surface tension and gradient.....</i>	<i>84</i>
5.4.2	<i>Flow motion transition.....</i>	<i>85</i>
5.4.3	<i>Influence of temperature and oxygen concentration</i>	<i>86</i>
5.4.4	<i>Development of temperature and oxygen concentration</i>	<i>89</i>
5.5	CONCLUSIONS	93

6	CONTACT LINE INSTABILITY.....	95
6.1	SPREADING AND WETTING THEORY	95
	Young's equation.....	96
	Smith's theory	96
6.2	EXPERIMENTAL DESCRIPTION.....	97
6.3	TEST CASES AND RESULTS	97
	6.3.1 Surface flow motion.....	97
	6.3.2 Marangoni film.....	97
	6.3.3 Chemistry mapping.....	103
6.4	DISCUSSION	104
	6.4.1 Thermal grooving and formation of a liquid net	104
	6.4.2 Oxygen influence and the formation of a Marangoni film.....	109
	6.4.3 Potential mechanisms for fingering flow.....	111
	6.4.4 Correlation between high and low temperature systems.....	114
6.5	CONCLUSION.....	115
7	CONCLUSIONS AND FUTURE WORK.....	117
7.1	CONCLUSIONS	117
7.2	FUTURE WORK	118
	REFERENCE	121
	SUMMARY.....	137
	SAMENVATTING	141
	LIST OF PUBLICATIONS	145
	ACKNOWLEDGEMENTS.....	147
	CURRICULUM VITAE	149

1 Introduction

Traditional fusion welding of metals and alloys is widely used in the construction of buildings and bridges, and in industries such as shipbuilding, aerospace, automotive, chemical, petrochemical, electronic, and power generation.¹ Recent developments of MEMS (Micro Electro Mechanical System) and NEMS (Nano Electro Mechanical System) have generated strong interest in micro and nano joining, and welding has important applications in microelectronics, medical devices, packaging of micro chips and joining of plastics. As a result, understanding and solving generic problems in welding and joining are of particular interest for current industrial applications.

Fusion welding can be carried out with a wide range of processes including oxy-fuel, arc welding and high-energy beam welding. With increasing energy density from oxy fuel welding to high-energy beam welding, the penetration and welding speed can be increased. This improves the fabrication efficiency and reduces the size of the heat affect zone and weld pool.

A series of complex physical and chemical processes are involved in fusion welding, including melting, fluid flow, vaporization, interfacial reaction and solidification; these processes occur simultaneously and make experimental measurements and numerical simulations difficult. Among these factors, fluid flow plays an important role in influencing the final geometry of the weld pool and the metallurgical structure; thus, understanding the fluid flow in the weld pool is important for controlling the final weld quality.

In addition to welding, brazing and soldering are widely used methods for joining metals or ceramics that employ a molten metal as the bonding material. The processes depend on a liquid metal flowing over surfaces to form a fillet between components or flowing into the gap between the components, and then solidifying to form a permanent bond. Thus, it is essential that the braze experiences high temperature attraction. Successful brazing depends not only on the characteristics of the liquid and the solid materials and of the vapour phase but also on the geometry and size of the joint.² This also makes understanding fluid flow important.

In a weld pool, the liquid metal often undergoes strong circulation and oscillation, the fluid dynamics in the weld pool can influence the final composition, geometry, structure, and properties of the welded joints. Prediction of these factors requires understanding of the liquid metal flow during welding.

Liquid metal flow influences heat transfer from the weld pool to the surrounding material, and convection of a weld pool often plays a more important role in heat transfer than heat conduction. The thermal cycle experienced during welding always attracts special

attention because knowledge of the temperature distribution is required to understand microstructures, residual stresses and distortion. Thus, knowledge of fluid flow can contribute to the understanding of temperature distribution as well as the kinetics of phase transformation and the development of the microstructure.

Liquid metal flow has an effect on mass transfer, including vaporization and mixing of the filler wire with the base material. For the former, vaporized metals escape from the liquid surface and can change concentrations of elements in the weld pool. For the latter, consumables are always expected to distribute homogeneously within the weld pool; however, the mixing procedure is limited by the flow properties of molten base metal and filler wire. For example, high strength 7000 series aluminum alloys, widely used in the aircraft industry and considered to be 'not recommended for fusion welding',^{3,4} are often joined by FSW(Friction Stir Welding).⁵⁻⁷ However, the weldability of 7000 series alloy can be improved by developing new consumables,^{8,9} containing small additions of scandium to modify the chemical and metallurgical properties of the fusion zone. Understanding mass transfer and its distribution is helpful for improving weld quality. Interest from industry in fluid flow during welding includes questions concerning how the flow influences the distribution of elements. Minor changes can make a significant difference to the weldability and properties of alloys.

Liquid metal flow has an effect on fatigue; for example, an unstable gas-liquid interface or vaporization can leave some gas bubbles or pores inside the weld pool. These can affect the lifetime of welded structures, since cracks can initiate at these locations. Industry has put significant efforts into measuring porosity and developing procedures to avoid the occurrence of pores and other weld defects.

Liquid metal flow also has an effect on the final weld appearance. A stable flow pattern can generate a smooth weld pool surface after solidification; however, many small bumps, or droplets mark the pool appearance when unstable flow occurs. Although researchers and engineers have observed instabilities and oscillations for quite a long time, there is still a shortage of information on how to generate a stable weld pool, since there are many forces influencing the fluid flow.

Liquid metal flow during welding is driven by surface tension, buoyancy, and when electric current is used, electromagnetic forces. Sometimes, aerodynamic drag forces of a plasma may also contribute to convection in a weld pool. Surface tension is often the main driving force,¹ and is influenced by temperature and surface active agents,^{10,11} which can change both the magnitude of the surface tension and its gradient. Two common surface active agents are sulphur and oxygen. Sulphur mainly comes from the base metals and oxygen from the environment.

Although both experimental and numerical studies have been employed to explore the fluid dynamics in the weld pool, numerical simulation is still the main approach. Simulations have provided detailed insight into welding processes; however, numerical simulations are limited in part due to shortage of thermo-physical data and the use of simplified models (for example flat surfaces or axial symmetry). Experimental measurements on real weld pools are still a challenge due to the high temperatures, small dimensions of the pool and strong illumination from the welding process.

In this thesis, an optical system combined with a high-speed camera is adopted to visualize flow patterns, and quantitative results on flow velocity fields are obtained by image processing. Together with the measurements on the final weld pool shape and its chemical properties, fluid flow and its influences are studied and described in the following chapters. The outline of this thesis is as follows; in chapter two, the three main experimental methods employed to measure fluid flow velocity are reviewed. The first is surface flow measurement, which is mainly based on camera observation; this is also the common method used for flow visualization. The second is internal flow measurement using high energy X-rays, when multiple X-ray views are obtained then computed tomography (CT) can be used to derive a three dimensional flow pattern. The last is physical simulation; this is based on similarity theory that two physical systems have similar properties when their dimensionless numbers are the same or reasonably similar.

In chapter three, two dimensional measurements of the surface velocity fields during TIG (Tungsten Inert Gas) welding are reported based on high speed visualization. The velocity field is obtained after analysing particle displacements. Whole surface flow fields are obtained; this is also the first time such whole surface velocities fields have been reported. Oxide particles are used as tracking media, and are assumed to have the same velocity as the liquid metal. Two test cases are considered; the first one visualizes the surface flow without surface active agents, where the flow is mainly an outward flow driven by a negative surface tension gradient. The second one is based on a case with surface active agents, where an inward flow occurs driven by a positive surface tension gradient. Inward flows form an interface, and induce frequent vortices at the rear of the weld pool. The surface deformation during inward flow leads to a concave surface; this makes two dimensional measurements unsuitable, thus, three dimensional measurements are necessary.

In chapter four, a three dimensional reconstruction method is introduced for laser spot welds, where only surface tension plays a significant role in driving the liquid metal flow. Two groups of mirrors are arranged in front of the high-speed camera to obtain images simultaneously from two different viewing angles. Three dimensional flow velocities are obtained by reconstruction based on the theory of machine vision. Although the accuracy is limited by the calibration, it provides a novel approach for three dimensional weld pool surface measurements based on only one high-speed camera. Suggestions for further improvements are also listed in this chapter.

How surface-active agents influence flow motion is described in chapter five, for laser spot welds under a controlled shielding gas environment with an oxygen concentration varying between 50 ppm and 20.9%. A transitional flow is observed when oxygen concentration is high enough to flip the outward flow to inward flow during the evolution of the spot weld. Oxygen appears in two forms; reactive oxygen contributes to the generation of oxides, and soluble oxygen acts as a surface-active agent to change the surface tension gradient. The occurrence of a transition from an outward to an inward flow depends on the relationship between temperature and the dissolved oxygen concentration in the weld pool. The role of each factor is examined separately and a simple theoretical analysis is employed to describe the experimental phenomena.

In chapter six, spreading of the weld pool boundary is reported for a case with a relative low laser power density (compared with the welding conditions reported in chapter 5). Experimental measurements of the liquid pool contact line show unstable patterns. Fingering flow is observed around the triple line with a thin film spreading ahead of the main pool. This fingering instability is thought to be induced by oxygen, which works as a surface active agent to affect the spreading boundary. Although the mechanism behind this phenomenon is still not clear, similar theoretical and experimental results employed for common room temperature liquids can be used to indicate potential reasons for such flow behavior in liquid metal systems.

Finally, general conclusions and suggestions for further investigations are given in chapter seven. X-ray visualization is recommended to examine the internal flow, since most of current reports are based on surface observations. Oxygen absorption is also suggested as an important subject to study in the future, because of its significant effect on surface tension. Interfacial phenomena such as free surface and triple line instability are highlighted as interesting projects for fundamental research.

2 Background

The intention in this work is to develop an understanding of fluid dynamic phenomena in the weld pool through experimental methods. Fluid flow has a significant influence on energy transport from the weld pool to the surrounding material, which in turn affects the geometry of the weld pool and the metallurgical structure of the heat-affected zone.¹ This can have important consequences for the resulting mechanical properties.

The subject of fluid dynamics in welding includes heat transfer, mass transfer, phase changes, melting and solidification. It is not essential to review all of them here, thus, some of the important problems and issues related to experimental fluid flow are selected and discussed in this chapter. Three main topics will be addressed:

- (1) The liquid metal fluid flow appears quite complex and is affected by many factors; complex flow motion can change the heat and mass distribution in the weld pool, in this section some reported flow patterns and their driving forces will be discussed.
- (2) In order to study the fluid flow phenomena quantitatively, experimental methods have been developed, although these always face some difficulties such as high temperatures, strong illumination and a small target. Both the methods and their contributions to surface velocity measurement are reviewed in this section.
- (3) Physical modeling is a method additional to direct experimental observation and numerical simulation, often consider when the latter cannot provide sufficient information on fluid dynamic phenomena. A physical model is reviewed in the last part of this chapter.

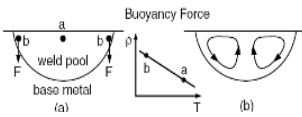
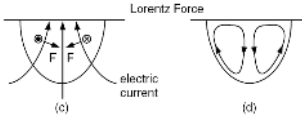
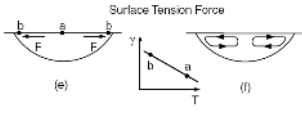
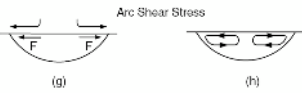
At the end of this chapter, some challenges related to the experimental investigations planned in the present work are outlined, and this thesis is based on addressing these challenges.

2.1 Flow patterns and their driving sources

2.1.1 The driving forces

The driving forces for fluid flow in the weld pools include the buoyancy forces, Lorentz forces, shear stresses induced by the surface tension gradient at the weld pool surface, and shear stresses acting on the pool surface due to the arc plasma as well as arc pressure. Kou⁵ describes these forces as presented in Table 2-1. These forces can induce complex flow motion in the weld pool.¹²⁻²⁷

Table 2-1 Driven forces during welding.

Driving force	Flow direction
<p>Buoyancy force</p> $F_b = \rho g \beta (T - T_{ref})^{18}$	<p>The density decreases with increasing temperature, the liquid metal is warmer at the weld pool center and cooler at boundary. Gravity causes the heavier liquid metal at the boundary to sink.</p> 
<p>Lorentz force</p> $\vec{F}_{emf} = \vec{J} \times \vec{B}^{19}$	<p>The converging current field, together with the magnetic field it induces, causes a downward and inward Lorentz force. The liquid metal is pushed downward along the pool axis and rises along the pool boundary.</p> 
<p>Surface tension</p> $\tau = \frac{\partial \gamma}{\partial T} \frac{\partial T}{\partial r} + \frac{\partial \gamma}{\partial C} \frac{\partial C}{\partial r}^{20}$	<p>The surface tension γ of a pure liquid metal decreases with increasing temperature. An outward shear stress is induced at the pool surface by $\partial \gamma / \partial T < 0$. Flow in the opposite direction if $\partial \gamma / \partial T > 0$.</p> 
<p>Shear stress by plasma jet</p>	<p>The plasma moving outward at high speeds along a pool surface causes the liquid metal to flow from the center of the pool surface to the pool edge and return to the centre below the pool surface.</p> 

2.1.2 Flow patterns

To date, surface observation is still the main method employed to study flow patterns. A study of flow motion on the weld pool surface based on arc welding has been reported by Woods and Milne,¹² who observed flow patterns on the bottom surface of full penetration

welds by following small oxide particles using cine photography. They also observed simulated model experiments with pools of mercury, and suggested that the motion in the weld pool is caused primarily by the action of Lorentz force, a subsidiary cause of motion is the action of the arc plasma jet on the surface of the weld pool.

Ercer¹³ made observation of pulsed current GTA welds on Fe-26Ni using high speed photography. Three types of pool motion were noted; radial flow was dominant in the early stages of the high and low pulses. Ercer explained that this behaviour was attributed to sudden changes in arc pressure, with faster flow velocities corresponding to larger time rates of change in current. The appearance of two symmetrical rotational flows was induced by electromagnetic effects. The surface oscillation was attributed to changes in arc pressure.

Hall^{14,15} used a video system with a high speed CCD camera with zoom lens to observe melting and solidification on the leading and trailing edges of moving GTA welds in stainless steel. The solid-liquid interface and ripple formation were studied by analysing the recorded images, the oscillation frequency was about 75 Hz, and the maximum interface velocity was 74.4 mms^{-1} . It was found that the flow oscillation has impact on the microstructure and chemical element distribution in the weld pool.

Kraus¹⁶ studied weld pool flow motion by measuring the weld pool surface temperature with an optical spectral radiometric/laser reflectance experimental method, and reported single, double or multiple cell radial and multiple cell angular flow as shown in Figure 2-1. He explained that the circulation on the surface is toward the centre and downward into the interior of the weld pool to create a narrow, deep weld pool (Figure 2-1a) when a positive surface tension gradient occurs on the surface. For a negative surface tension gradient, the circulation on the surface is away from the centre, forming a shallow, broad weld pool (Figure 2-1b). When a positive and negative surface tension gradient occur on the same surface, as shown in Figure 2-1c, double cells can appear. The counter rotating flow condition shown in Figure 2-1d is explained by electromagnetic force domination in the inner region, and surface tension, dependent on temperature and surface active elements in the outer region.

Kraus also discussed the multi-cell condition as shown in Figure 2-1e, he explained that this condition may be uniquely associated with higher current welds, and this pattern may be similar to Bernard cells, but driven by a different combination of forces. It is known that Bernard cells²³ are primarily driven by surface tension and buoyancy forces, whereas these weld pool convection cells, which are known to be driven by surface tension and electromagnetic forces, may be driven by buoyancy forces as well when dealing with high welding currents and large weld pools. Kraus explains that since buoyancy forces account for the break up into multiple cells in the Bernard patterns, this force may also account for the multiple cells present in the angular direction of such weld pools. Later, Zacharia *et.al*¹⁷ validated some of Kraus's experimental results by computational modelling. The computed weld pool shapes fit the experiments very well; however, velocity validations were not provided because of the difficulty involved in performing the experiments.

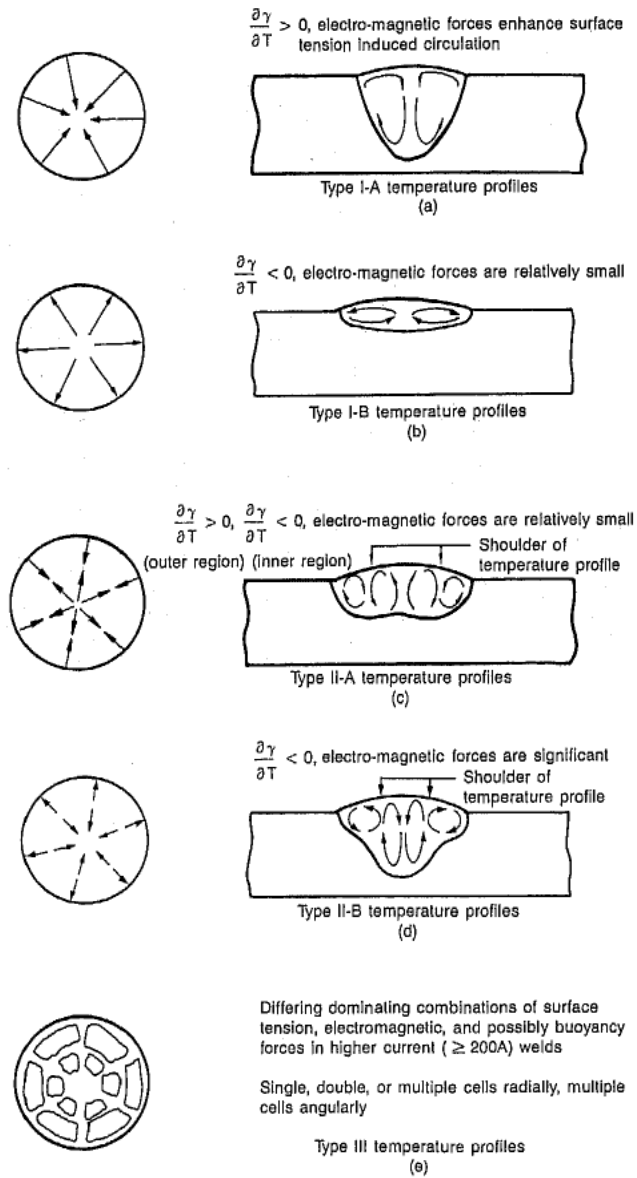


Figure 2-1 Weld pool circulation patterns as related to surface temperature profile types.¹⁶

2.2 Current methods for studying fluid flow in welding

2.2.1 Experimental observations

Surface flow

Although experimental visualization faces several obstacles, a number of successful cases have been reported. The oscillation and oxide particle movement on the weld-pool surface make it possible to visualize the surface flow. A CCD optical arrangement was used to visualize the weld-pool by Henrikson,^{24,25} who successfully observed weld pool surface flow during TIG welding on stainless steel. Surface vortex flow has also been described by Henrikson, and one of his results is shown in Figure 2-2. Using PTV (Particle Tracking Velocimetry), Henrikson^{24,25} reported surface particle velocities up to 0.13 ms^{-1} .



Figure 2-2 Surface flow observation by Henrikson²⁴

Nearly the same method was used to study surface flow by Delapp,²⁶⁻²⁷ who examined 1020 cold rolled steel plate, 304 stainless steel and 1018 carbon steel. His results show that the average velocity is $9 \times 10^{-3} \text{ ms}^{-1}$ and the maximum and minimum velocities are 0.0225 ms^{-1} and 0.00074 ms^{-1} respectively, with a Reynolds number around 107.

Delapp²⁶⁻²⁷ studied solidification and surface flow during gas tungsten arc (GTA) welding. Surface flow velocities were calculated based on tracking tracer particles on the free surface and vortices were observed. Although individual particle velocities were too fast to track by eye, an axial circulating flow pattern was noted. Often this consisted of a pair of counter rotating eddies on the weld pool surface. A schematic representation of this is shown in Figure 2-3. The axial flow is similar to flows reported by Woods and Milner,¹² who demonstrated that axial pool circulation is indicative of electromagnetically induced flow. The radial particle flow is consistent with observations by Heiple,²⁸ who observed that radial pool circulation is indicative of surface tension driven Marangoni flow.

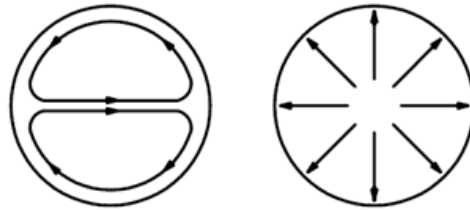


Figure 2-3 (a) Schematic representation of the double recirculation surface flow pattern observed on some moving weld pools. (b) When travel stopped the particles moving in the double recirculation pattern rapidly moved outward along a radial path to the periphery of the weld pool.²⁷

Internal flow

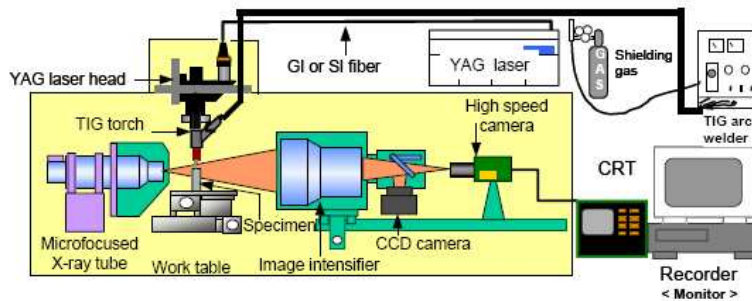
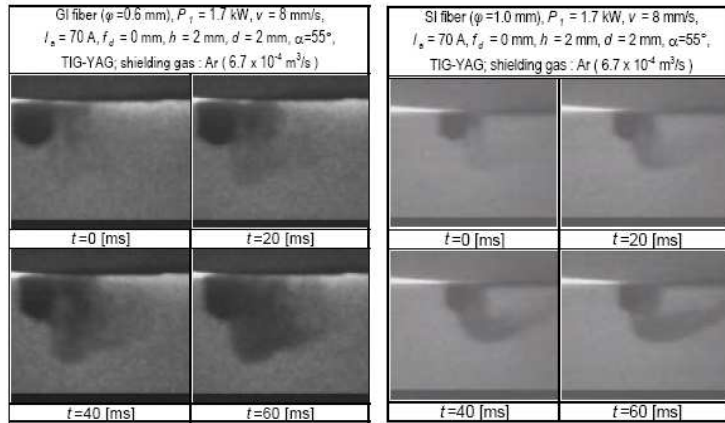


Figure 2-4 Experimental set up of X-ray transmission imaging system for observation of phenomena during hybrid welding.²⁹

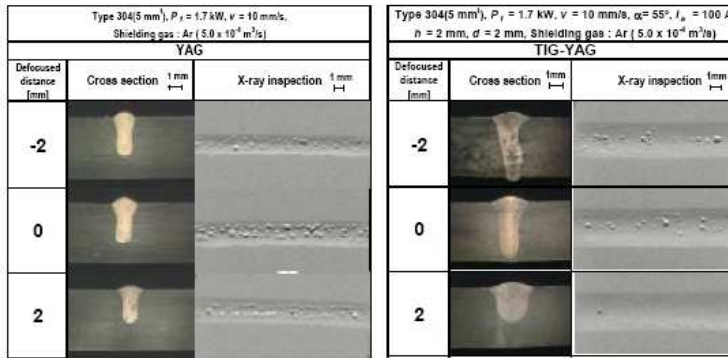
Since the metal is opaque for normal light, X-ray transmission methods have been used to observe molten metal flow behavior during laser and hybrid welding at the Joining and Welding Research Institute of Osaka University.²⁹⁻³³ The experimental configuration is shown in Figure 2-4.

During welding, a CCD camera and a high-speed camera were used to observe the arc plasma and a laser-induced plume. Keyhole behavior, bubble formation, melt flows and molten pool shapes were also observed through X-ray real-time transmission, as shown in Figure 2-5. For clear visualization of pool geometry, a platinum wire was placed in a hole on the surface of type 304 steel plate, and tungsten particles were also set between square butt-joint faces to elucidate melt flows in the pool. By using this system, Naito *et al.*³⁰ captured porosity formation in weld pools (see Figure 2-5a for a graded index GI fiber and Figure 2-5b for step index SI fiber). They also observed the molten pool shape and melt flows during TIG-Nd:YAG welding with an X-ray transmission imaging system (Figure 2-5c and Figure 2-5d), with platinum and tungsten markers. Figure 2-5e and Figure 2-5f show results when GI fiber and SI fiber were used respectively.



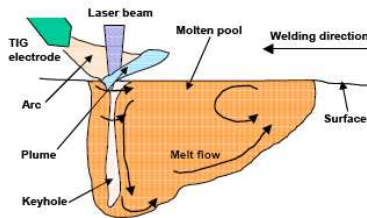
(a)

(b)

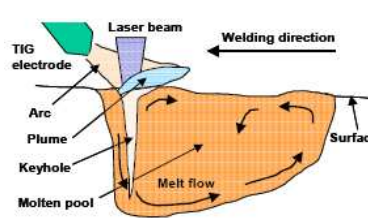


(c)

(d)



(e)



(f)

Figure 2-5 (a) and (b) X-ray visualization results, (c) and (d) cross sections (e) and (f) schematic representation of keyhole and liquid flow in a molten pool.²⁹

Weld pool shape measurement

Methods adopted to view the surface of the weld pool, include using the electrode tip to block the bright core of the arc from overpowering the exposure of a camera and selecting an optimal band pass filter to simultaneously eliminate the radiation from the electric arc and from the weld pool, based on an analysis of the light spectrum. Using additional illumination often helps to improve visualization qualities.

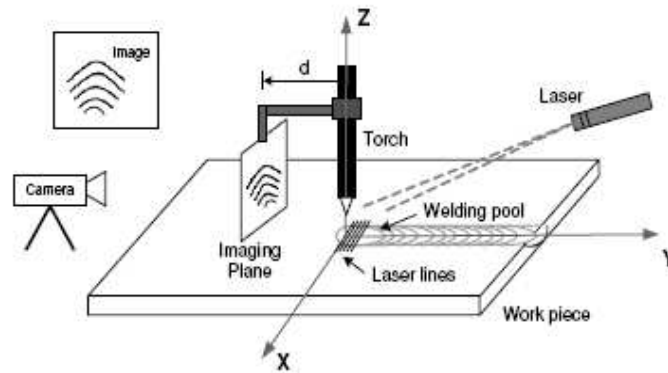


Figure 2-6 Laser illumination system.³⁴

Zhang *et al.*³⁴ measured weld pool surface variations using an additional laser; their experimental configuration is shown in Figure 2-6. The laser can generate multiple lines, which are reflected by the weld pool surface to a known image plane, the clear image is shown in Figure 2-7. By studying variations of these lines, the variations of the weld pool surface can be obtained.

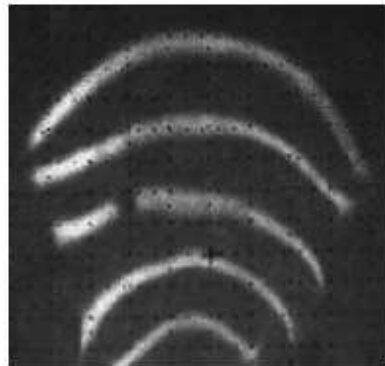


Figure 2-7 Reflected laser lines on the imaging.³⁴

Due to the effect of radiation from the weld pool, the image quality is influenced by the camera position (top, front or back). This method was further developed by Song and Zhang^{35,36} to measure the weld pool surface shape experimentally. They combined the results with a mathematical model to determine the shape from the measured reflections. Smith and Baflour³⁷ developed a real time vision system to observe the weld pool from the topside. Beardsley³⁸ presented a system for process monitoring of laser beam welding based on a CMOS-camera. The system observed the welding process online and coaxial to the laser beam and was used to investigate the geometrical parameters of the keyhole. Pietrzak,³⁹ Brzakovic *et al.*⁴⁰ have developed coaxial arc weld pool viewing systems using the electrode tip to block the bright core of the arc from overpowering the exposure on the CCD target. All of these methods contributed to understanding liquid metal flow behavior during welding.

3D measurement

Unfortunately, 2D information cannot represent the real shape of weld pools, 3D measurement is therefore necessary. Although detection of a 3D weld pool online is an ongoing research subject, current methods of 3D measurement can be divided into two kinds. One is 3D reconstruction from 2D images based on machine vision mechanisms,⁴¹⁻⁴⁶ such as the case shown in Figure 2-8, where a 3D reconstruction system is shown for imaging the topside and underside of a weld pool simultaneously in the same frame. These two images can be used to reconstruct 3D information. The other approach is model reconstruction based on some mathematical assumptions,⁴⁴ as illustrated in Figure 2-9, where laser light rays that hit the liquid metal surface of the weld pool will be reflected and generate a dot matrix on an image plane after reflection. A mathematical model for the three-dimensional surface measurement was established.

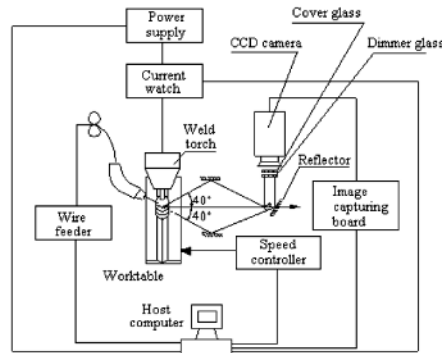


Figure 2-8. 3D construction weld system.⁴¹

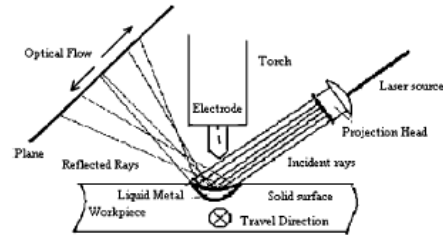


Figure 2-9 Proposed observation approach.⁴³

Since 3D surface geometry of the weld pool is an important parameter for reflecting the penetration, many other 3D measurements have been attempted. Zhang *et al.*⁴¹ used a structured-light-truncated method to detect the average sag depression depth of a weld bead from, which full penetration control was obtained in GTAW. Furthermore, Kovacevic and Zhang⁴² developed a sensing system using a high shutter speed camera, assisted with pulsed laser stripes, to detect the 3D shape of a weld pool surface. To develop a cost-effective system for real-time control applications, Saeed *et al.*⁴⁴ proposed a sensing technique that only used a high-speed CCD camera and laser, and which did not require synchronization between the camera and laser. Zhang *et al.*⁴⁶ reconstructed the 3D shape based on a mathematical model, which used the maximum width, the length of the pool tail, the height of the rear of the pool and the projection of the rear angle onto the workpiece plane as model parameters. Because this method needs boundary extraction and image processing algorithms, it is limited to post processing.

Normally, 3D reconstruction needs at least two images from different views, more information can be captured by this method, but complex experimental systems are needed, such as using two cameras or other similar optical path arrangements. Moreover, calibration and reconstruction algorithms are also quite complex. Using two cameras will be more accurate than one camera. But the system can be inconvenient for industrial applications. Therefore, single camera measurements have become more widely adopted by researchers based on suitable mathematical assumptions, such as those of Zhang *et al.*⁴² and Zhao *et al.*⁴¹

2.2.2 Numerical simulations

In comparison to experimental developments, numerical models have evolved much more rapidly for the study of welding. CFD (Computational fluid dynamic) models have contributed to quantitative understanding on physical mechanisms during welding, such as heat transfer from heat sources⁴⁷⁻⁴⁹ to the liquid metal, resultant temperature distributions; mass transfer between the environment and the weld pool, or between the filler wire and the weld pool, and final chemical distributions. CFD is also a practical tool employed in industries. Three main issues related to CFD models are reviewed here.

Weld pool free surface

An important boundary condition is the free surface, because the weld pool surface shows strong oscillation in many cases.⁵⁰⁻⁵² Simulations based on flat surface assumptions are not suitable when weld pool surface deformation occurs; therefore, a free surface must be considered in the boundary conditions.^{53,54} The volume of fluid (VOF)⁵³⁻⁵⁸ method is commonly considered in weld pool simulations, such as heat and fluid flow in GMA butt welds,⁵⁹ GMA weld pools with consideration of droplet impact,⁶⁰ and the influence of two free surfaces during full penetration welding.⁶¹

Laminar flow and Turbulent flow model

It is still not clear if the flow is laminar or turbulent in a weld pool, but it is suggested that judgments for turbulence or laminar flow should consider several factors, such as irregularity, diffusivity, large Reynolds number, three-dimensional vorticity fluctuations, and dissipation.⁵⁵ The presence of vorticity in Delapp²⁶ and Hensikon's²⁴ surface observations means that the flow is rotational, although a rotational flow is not necessarily turbulent. Thus, numerical simulations based on laminar models cannot be correct since visual observation of weld pools indicates unsteady behavior. Malinowski-Brodnicka *et al.*⁶² supported the concept that the pool circulation could be turbulent. To examine laminar flow or turbulence in the weld pool, Choo and Szekely⁶³ first contrasted experimental result with numerical simulation based on different models, which suggested that turbulence models provide better comparison with experimental results in terms of the weld pool shape.

Hong *et al.*⁵⁴ demonstrated that a fluid flow model based on laminar flow can over-predict the pool depth, for a GTA weld in a 304 stainless steel. When turbulence is considered, the calculated pool depth decreases and agrees better with the observed results. Yang and DebRoy⁶⁵ studied turbulent heat transfer and fluid flow during GMA welding of HSLA-100 steels; their computed fusion zone geometry was in good agreement with the experimental data.

Estimation of order of maximum velocity in the weld pool

The flow in the weld pool is driven by surface tension, buoyancy and electromagnetic force when an electric current is used. In some instances, aerodynamic drag forces of the plasma jet may also contribute to the convection in the weld pool. Zhang²⁰ computed the maximum velocity in a GTA weld pool as shown in Table 2-2. The maximum velocity for the buoyancy driven flow is much smaller than that for the electromagnetic and Marangoni driven flow.

Different driving forces play important roles in dissipating heat and determining the temperature distribution in a weld pool. Therefore, to accurately simulate the weld heat transfer and fluid flow and to understand the physical mechanisms driving flow in the weld pool, experimental measurements should provide validation.

Table 2-2 Order of the maximum velocity in the GTA weld.

Description	Maximum velocity (mm/s)
Buoyancy force ⁶⁷	2.7
Electromagnetic force ⁶⁷	21
Marangoni force ¹	140

2.3 Physical modeling

When direct measurement is difficult or sometimes even impossible, physical model simulation is used to provide information to study the behavior of a system. By using physical models, access can be gained to basic data which is impossible or quite expensive to obtain for real objects. The development of fluid mechanics has depended heavily on experimental results because so few real flows can be represented adequately by analytical methods alone. Solutions of real problems involve a combination of analysis and experimental information.

2.3.1 Some dimensionless numbers describing fluid flow

According to the theory of dimensional analysis, similar dimensional numbers have similar properties. During welding, interesting parameters are flow velocity, temperature and shear forces, which influence heat and mass transport. There are several characteristic numbers which can be used to describe useful flow properties.

Dimensionless numbers can characterize the relative importance of some factors, or help to predict the size and shape of the FZ (Fusion zone) and HAZ (Heat affection zone). For instance, if the electromagnetic force is the dominant driving force, a deep and narrow pool shape is expected. In contrast, if the surface tension gradient force with negative $\partial\gamma/\partial T$ is largely responsible for the liquid motion, the resulting weld pool is expected to be wide and shallow. The following dimensionless numbers are used to evaluate the relative importance of the driving forces.

The Grashof number

$$Gr = \frac{g\beta L_b^3 \Delta T \rho^2}{\mu^2}. \quad (2.1)$$

The Grashof number (Gr) defines the ratio of buoyancy to viscous force, where g is the acceleration due to gravity, β is the thermal expansion coefficient, ΔT is the difference between the pool peak temperature and the solidus temperature of the material, L_b is a characteristic length for the buoyancy force in the liquid pool, ρ is the density, and μ is

the liquid viscosity. A high Grashof number indicates a buoyancy dominated flow.

The Magnetic Reynolds number

$$Rm = \frac{\rho\mu_m I^2}{4\pi^2 \mu^2} \quad (2.2)$$

The magnetic Reynolds number (Re) defines the ratio of electromagnetic force to viscous force, where ρ is the density, I is the arc current, μ_m is the magnetic permeability and μ is the liquid viscosity.

The Marangoni number

The Marangoni number (Ma) is used to describe the ratio of surface tension gradient force to viscous force.

$$Ma = \frac{\partial\gamma}{\partial T} (\Delta T)L / \mu\alpha, \quad (2.3)$$

where $\partial\gamma/\partial T$ is the thermal gradient of surface tension, ΔT the temperature difference between the center and edge of the pool surface, L the characteristic length, which can be taken as the pool radius, μ the dynamic viscosity and α the thermal diffusivity.

Once the values of Gr , Rm and Ma are determined, the relative importance of the driving forces, *i.e.*, surface tension gradient, electromagnetic, and buoyancy forces, can then be judged by the combination of these dimensionless numbers. For example, the ratio of the electromagnetic force to the buoyancy force is given by:

$$R_{M/B} = \frac{Rm}{Gr}. \quad (2.4)$$

The ratio of the surface tension gradient to the buoyancy force is expressed as:

$$R_{S/B} = \frac{Ma}{Gr}. \quad (2.5)$$

Zhang²⁰ computed useful dimensionless numbers as shown in Table 2-3. The buoyancy force is negligible compared to the electromagnetic and surface tension gradient forces. The surface tension gradient force plays a more important role than the electromagnetic force, since $R_{S/B}$ is greater than $R_{M/B}$. Therefore, for the particular set of conditions examined, a wide and shallow pool shape is expected, which is consistent with the experimental observation.

Peclet number

$$Pe = \frac{Lu}{\alpha} = \frac{Lu\rho C_p}{k} \quad (2.6)$$

The Peclet number (Pe) gives the ratio of heat transport by convection to that by conduction. Here L is the characteristic length, u is the characteristic velocity, α is the thermal diffusivity ($k/\rho C_p$), ρ is the density, C_p is the specific heat, k is the thermal conductivity. When Pe is much larger than one, heat transport occurs primarily by convection, and heat conduction in the weld pool is not of primary importance. However, for metals with high thermal conductivities, at low velocities and for small pool sizes, the value of Pe can be low ($Pe \ll 1$), and accurate calculations of heat transfer can be realized using relatively simple conduction calculations.¹

Bond number

The Bond number (Bo) is often used as a qualitative indication of the strength of buoyancy convection relative to that of Marangoni convection.

$$Bo = \frac{\rho g L^2}{\gamma} \quad (2.7)$$

where ρ the density of the melt, g the gravitational acceleration 9.80 ms^{-2} , L the characteristic length taken as the radius of the weld pool and γ the surface tension.

Prandtl number

The Prandtl number (Pr) represents the ratio of viscous to thermal diffusion rates and is used in heat transfer in general and free and forced convection calculations in particular.

$$Pr = \frac{C_p \mu}{k} \quad (2.8)$$

where C_p is the specific heat, μ is the dynamic viscosity and k is the thermal conductivity. The lower the thermal conductivity, the higher the Prandtl number.

Table 2-3 Dimensionless numbers in the GTA welding.

Dimensionless number	Description	Value
Gr	Ratio of buoyancy to viscous force	30
Rm	Ratio of electromagnetic to viscous force	7.0×10^4
Ma	Ratio of surface tension to viscous force	9.4×10^4
$R_{M/B}$	Ratio of electromagnetic to buoyancy force	2.3×10^4
$R_{S/B}$	Ratio of surface tension to buoyancy force	3.1×10^4

2.3.2 The physical model of Limmaneevichitr and Kou

Flow visualization is an important method to study the flow field in a fluid, but it is limited to the pool surface in welding because the molten metal is opaque. Even at the pool surface, such observation can still be difficult because of the brightness of the arc. The model weld pool was first introduced to study fluid flow inside a weld pool by Limmaneevichitr and Kou.⁶⁸⁻⁷¹ Using physical models, they visualized the fluid flow inside the model pool, measured the surface temperature and studied the effect of surface active agents. They showed that physical modeling is an efficient method to simulate a real weld pool.

Materials

Sodium nitrate $NaNO_3$ was selected as the material for flow visualization for the following reasons. Firstly, $NaNO_3$ has a transparent melt, a surface tension that significantly varies with temperature, a low melting point and well documented physical properties. Secondly, the Marangoni number Ma for the simulated $NaNO_3$ weld pool is close to that for steel and aluminum weld pools. Similarity in Marangoni convection between two fluid systems can be expected if the Marangoni numbers are close to each other. Finally, $NaNO_3$ has a radiation transmission range of 0.35-3 μm and is, therefore, opaque to CO_2 laser radiation.

Apparatus

The apparatus for flow visualization shown in Figure 2-10 consists of the following components. First an essentially hemispherical pool of $NaNO_3$ was held in a glass tube (10mm ID). Second, a much larger $NaNO_3$ melt was held in a square glass beaker (40mm×40mm in side) to keep the pool from freezing and becoming opaque. Third, a CO_2 laser beam was shone at the center of the pool surface to induce Marangoni convection. Fourth, a 20mW He-Ne laser light sheet was passed through the meridian plane of the pool as an illuminator to reveal the flow pattern.

Flow visualization

A laser light-cut technique for flow visualization was used. Alumina particles 20 μm in diameter were employed as tracers although the density of aluminum is greater than that of the $NaNO_3$ melt. In fact, aluminum particles ($\rho = 2.7 \times 10^3 \text{ kgm}^{-3}$) are often used for flow visualization in water, which is even less dense than $NaNO_3$ ($\rho = 1.9 \times 10^3 \text{ kgm}^{-3}$).

Surface-active agent

Heiple *et al.*^{10,11} proposed that, when a surface active agent is present in the liquid metal in small but significant amounts, $\partial\gamma/\partial T$ can be changed and a deep weld pool can be formed. Examples of surface-active agents in steel and stainless steel are *S*, *O*, *Se* and *Te*. Limmaneevichitr and Kou⁶⁹ added C_2H_5COOK which is a surface active agent for the $NaNO_3$ pool and reversed the direction of Marangoni convection. The C_2H_5COOK acts like *S*

in a weld pool (which reduces the surface tension of liquid steel), and reduces the surface tension of NaNO_3 . The NaNO_3 pool shown in Figure 2-11 contains 2 mol% of $\text{C}_2\text{H}_5\text{COOK}$ and its surface flow is inward.

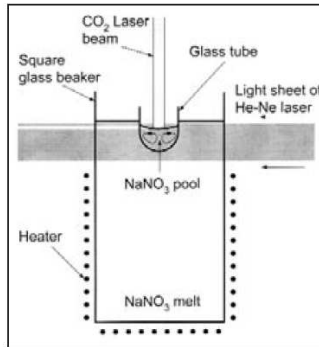


Figure 2-10 A transparent system for physical simulation of Marangoni convection in a weld pool.⁶⁹

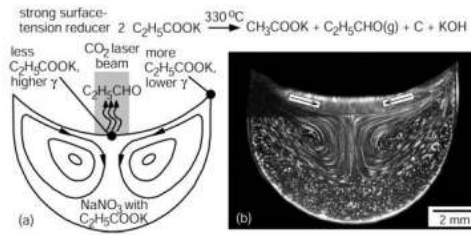


Figure 2-11 Marangoni convection with an inward surface flow in a NaNO_3 pool containing 2 mol % $\text{C}_2\text{H}_5\text{COOK}$ as a surface-active agent.⁶⁹

2.4 Summary

Although considerable work has been carried out to observe fluid flow during welding, and some methods have even been applied to evaluate the shapes of weld pools, there is still a shortage of information concerning quantitative flow behaviour. This is important because fluid flow affects energy transportation, which determines the final geometry of weld pools. Although surface flow patterns have been studied, and some flow velocities are reported in the literature, the flow velocity field on the whole surface has not yet been reported. Tracking a few particles in a flow is not enough to represent the real flow motion.

There are reports of quantitative experimental measurements involving real time visualization of the surface flow field in the presence of surface active elements. As is known, surface active agents can change the surface tension and surface tension gradient significantly; which can also induce complex interfacial flow phenomena.

Unsteady weld pool formation is important for understanding the melting progress and solid-liquid interface dynamics. No quantitative experimental data to support current numerical simulations has yet been reported. Thus, it is necessary to study the flow quantitatively. However, some problems may be encountered due to the complexity of fluid dynamics in welding. Some important unsolved questions are address here:

The flow boundary of weld pools is dynamic, liquid metal is melted continuously, which makes it difficult to define the real boundary for on-line measurement.

Quantitative velocity cannot be measured directly; some tracers must be added to the weld pool. However, these will lead to particle surface interactions, which should be understood well; otherwise the evaluated velocity can be in error.

Furthermore, quantitative evaluation needs an efficient geometric transformation since weld pools always have a 3D surface shape and the curvature can be significant. 2D computations for velocity or flow descriptions are not sufficient for accurate results. These aspects are addressed and assessed in this thesis.

3 Two dimensional velocity measurements

To date, most of the reported experimental results concerned with fluid flow in liquid weld pools evaluate the surface flow by tracing single particles, rather than the whole flow field. In this chapter, the whole surface flow field for a gas tungsten arc (GTA) weld pool has been computed based on a study of the movement of the natural oxide layer on a 316L stainless steel substrate. The surface flow is reconstructed from high-speed camera images using particle image velocimetry (PIV).

3.1 PIV (particle image velocimetry) and its principle

3.1.1 PIV introduction

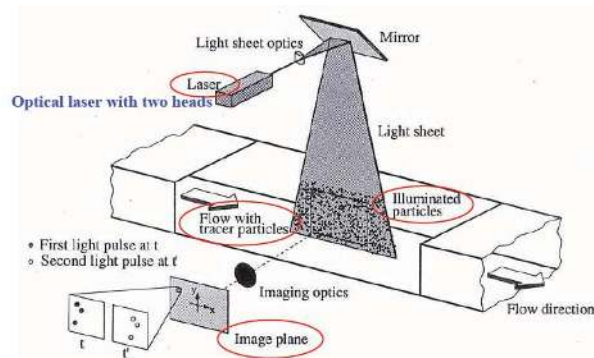


Figure 3-1 Experimental arrangement for PIV⁷²

Particle Image Velocimetry (PIV) is a nondestructive technique for simultaneously measuring the velocities at many points in a fluid. The fluid is seeded with tracer particles and the region under investigation is illuminated. An image of the illuminated region is captured and then, a short time Δt later, a second image is taken (see Figure 3-1). Suitable analysis of these images yields what is referred to in the literature as an instantaneous velocity vector map.⁷²

Particle displacements are determined by comparing the two flow images; these displacements are divided by the time interval Δt to extract the instantaneous velocity field data. By ensemble averaging many instantaneous measurements, velocity or turbulent statistics of the flow can be obtained.

3.2 Applications in welding

3.2.1 Experiment system arrangement

A CMOS high-speed camera (Phantom V5) was used to capture the surface flow motion. The camera was placed at the back of the weld pool looking in the welding direction (see Figure 3-2). A 1 nm optical band pass filter (wavelength $\lambda = 632$ nm) was placed in front of the Nikon 70-300 mm camera lens to reduce the strong interference from the arc light as well as to improve image contrast. An additional laser light (10 mW He-Ne 632 nm) was focused on the weld pool to provide sufficient illumination. The camera observation angle was about 60° to the plate normal and the laser illumination was placed at the approximately the same angle. The welding traverse system comprises a three orthogonal axis stepper motor driven system, which was arranged as shown in Figure 3-2.

For simplicity, welding was carried out using the gas tungsten arc process with a commercial welding torch and DC power source. A 2.4 mm diameter 2% thoriated electrode was employed ground to a 60° included angle, extending 6 mm from a 12 mm internal diameter shielding cup. Argon shielding gas was supplied at a rate of 11 l min^{-1} and the arc length was maintained at 3 mm for all experiments. Bead on plate welds were made on 316L stainless steel samples of size 2 mm x 200 mm x 100 mm. The chemical composition and physical properties are listed in Table 3-1. Tungsten powder and natural oxides were examined for use as tracer particles to evaluate the surface flow.

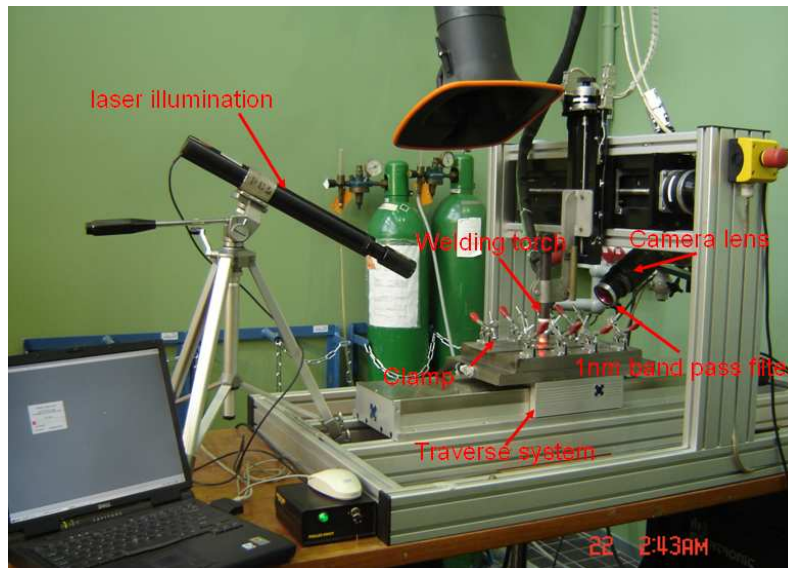


Figure 3-2. Experimental arrangement.

Table 3-1 Composition and properties of 316 L stainless steel.

Component	Wt. %	Physical Properties	Value
C	Max 0.03	Density	7660 kgm^{-3} (920 K) ⁷³
Cr	16-18		7840 kgm^{-3} (570 K) ⁷³
Fe	62-72	Melting Point	1644-1672 K
Mn	Max 2	Solidus	1644 K
N	Max 0.01	Liquidus	1672 K
Ni	10-14	Specific Heat	$738 \text{ Jkg}^{-1}\text{K}^{-1}$ (1500 K) ⁷³
P	Max 0.045		$657 \text{ Jkg}^{-1}\text{K}^{-1}$ (1050 K) ⁷³
S	Max 0.03	Viscosity	$0.006 \text{ kgm}^{-1}\text{s}^{-1}$
Si	Max 0.075	Surface tension coefficient	$0.3 \times 10^{-3} \text{ Nm}^{-1}\text{K}^{-1}$ ⁷⁴

3.2.2 PIV calculation

Particle Image Velocimetry⁷⁵⁻⁷⁷ is a well-established non-intrusive technique to quantitatively measure instantaneous two-dimensional velocity distributions in fluids from the motion of tracer particles suspended in these fluids. In contrast to techniques which are based on tracing individual particles, the features of the velocity fields are resolved for so-called interrogation areas in PIV.

Interrogation areas contain, in general, multiple particles and the size of these areas defines the spatial resolution. Processing of images is briefly described in Figure 3-3. After division of the images into interrogation areas, associated areas in successive images are cross-correlated. The position of the highest peak in the cross-correlation plane of two associated interrogation areas yields the displacement vector for that particular area in the flow. A two-dimensional velocity field is finally obtained by dividing the displacement vectors of all interrogation areas by the time between the successive images.

An adaptive multi-pass algorithm is commonly used in the evaluation of PIV images, it consists of several steps. In the initial step, the velocity field is estimated for relatively large interrogation areas containing relatively large numbers of particles. In subsequent steps, calculations are repeated for decreasingly smaller interrogation areas using the estimated velocity fields from previous steps.

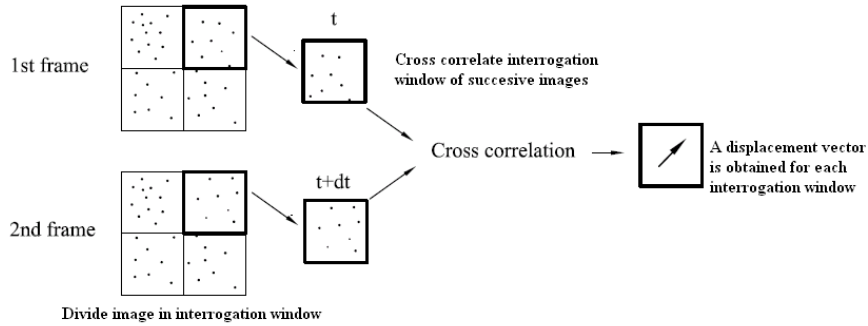


Figure 3-3 Illustration of the basic principle of PIV.

In this work, commercial software (Davis 6.2, LaVision) was used to process the images. Videos from the high-speed camera were decompressed and converted into images of a standard bitmap format. These images were processed using an adaptive multi-pass PIV algorithm.

For initial assessment of the window size, an estimate of the maximum velocity on the weld pool surface is required to ensure that particles remain substantially within a window between successive images. For this purpose, a maximum velocity of 1 ms^{-1} was assumed. The calibrated relationship between the image coordinate system and real world system was used to compute the maximum distance on the images moved between successive high-speed camera images. The principal processing steps for velocity field calculation are described in Figure 3-4.

After computing the flow field for a given window size, the results were manually compared with the original video to determine whether the derived flow field details match those visually apparent in the original image. This semi-subjective check is included because an erroneous computational flow field can appear when the interrogation window becomes too small. If a reasonable correlation is evident, then a smaller sized interrogation window is selected and the velocity field calculation is repeated to improve resolution. If the results for successive window sizes converge, then the results are stored and the sequence is terminated. If no reasonable flow field is obtainable, new images are chosen as the computational object and computation starts again.

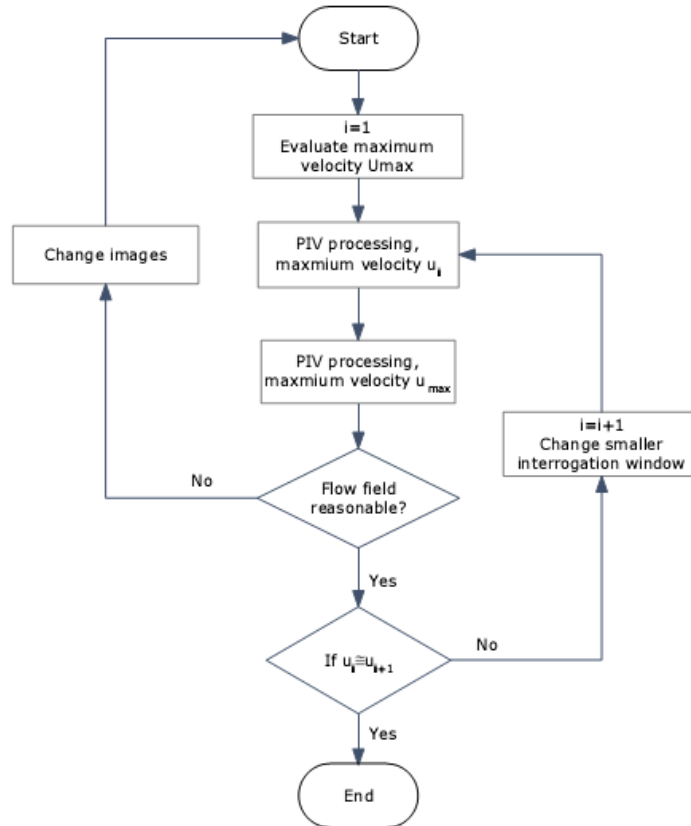


Figure 3-4 Flow chart showing processing steps for velocity field determination where increasing i indicates a smaller mesh size.

3.2.3 A simple analyses for surface particle flow

Since welding is a high temperature process, it is difficult to choose appropriate seeding particles. Tungsten powder was examined; however, it was observed that the shielding gas appeared to have a larger influence on the flow properties than the surface motion. Tungsten does not readily wet in steel, the shielding gas can significantly affect particle movements if the metal powder floats on top of the weld pool surface, as indicated schematically in Figure 3-5a. For the partially submerged particle, Figure 3-5b, the viscous forces acting on the metal powder particle are proportional to the dynamic viscosity of the fluids. The viscosity of argon⁷⁸ (at 2000 K) is about $9 \times 10^{-5} \text{ kg m}^{-1}\text{s}^{-1}$ and that of the liquid steel (at 1870 K) is about $6 \times 10^{-3} \text{ kg m}^{-1}\text{s}^{-1}$; the viscous force acting on the particle due to the liquid metal is therefore about two orders of magnitude greater than that due to the argon gas. The inertial forces, proportional to the flow velocity⁷⁹ and

density $\rho_{\text{argon}} (T=2000 \text{ K}) \sim 0.2 \text{ kg m}^{-3}$, $u_{\text{argon}} \sim 100 \text{ m s}^{-1}$; $\rho_{\text{steel}} \sim 7.6 \times 10^3 \text{ kg m}^{-3}$, $u_{\text{steel}} \sim 0.05 \text{ m s}^{-1}$ show a one order of magnitude difference. This suggests that the partially submerged condition (Figure 3-5b) is reasonable for tracing surface flow, because the arc gas force is much smaller than that of the liquid metal. The exposed section of the particle is reasonable for reflecting the incident laser light to the camera. When the particle is practically submerged (Figure 3-5c), the visible exposed section is too small to reflect sufficient laser light, detection of the particles in the images becomes difficult and flow information is lost.

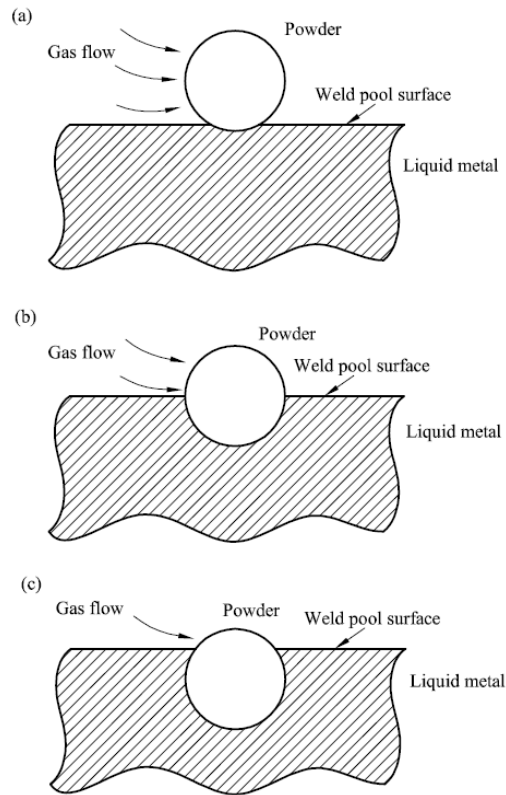


Figure 3-5 Three kinds of possible states for metal particles floating on the weld pool surface.

Wetting between powder and liquid metal is difficult to measure or control in weld pools and added powders often agglomerate, which makes it difficult to obtain a homogeneous distribution of tracer particles on the pool surface. Tungsten powder was therefore abandoned in favour of tracking natural oxide particles, which have compatible chemical properties with the base material. Prior to welding, the natural oxide layer is typically thin and is broken into small particles on the pool surface during welding. The distribution of

the oxide particles is relatively uniform compared with powder additions and can follow the surface flow sufficiently for PIV processing. Smaller particles have better tracking properties, current natural oxide particles have quiet small response time and are added to follow the flow according to the characteristic response time equation⁷²

$$\tau = \frac{\rho_p d_p^2}{18\mu} \quad (3.1)$$

where the τ is response time, ρ_p is the particle density, d_p is the particle diameter and μ is the viscosity. The response time τ is in the scale of 10^{-6} seconds for $d_p = 10 \mu\text{m}$ with liquid properties shown in Table 3-1. Henrikson²⁴ reported successful observation of flow vortices on the weld pool surface using natural oxide particle tracing.

3.3 Measured case I, results and discussion

3.3.1 Effects of the natural oxide layer

It is reported that oxygen concentrations can substantially alter the surface tension,^{11,80} which can make a significant difference to the final weld pool shape. To determine whether the natural oxygen diffusion can affect the surface tension, transverse cross sections of weld pools were measured as shown in Figure 3-6 a and b. In both cases, the left side shows the final weld pool shape from a weld in the presence of a natural oxide layer. The right side shows the cross section of a weld made under nominally identical conditions after surface cleaning with a tungsten carbide paper immediately prior to welding, to remove as much of the excess oxide layer as possible. For a current of 80A, the weld pool shape and size is virtually unchanged. For a fully penetrating weld made at 120A, some difference is observed (see Table 3-2); one reason could be that both the topside and bottom side oxide layers play a role and these can influence pool oscillation dynamics.⁵⁰⁻⁵² For the partially penetrating condition, it may be concluded that for the conditions and material examined, the presence of the natural oxide does not substantially influence the fluid motion.

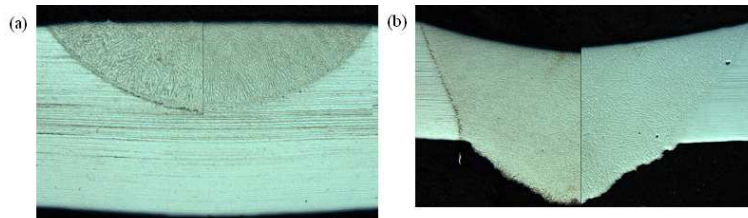


Figure 3-6 Weld pool shapes for bead on plate welds on 2mm thick 316L stainless steel at (a) 80 A and (b) 120 A. The left hand side of each image shows welds made on a sample with a natural oxide layer, whilst the right hand sides show welds made on cleaned surfaces.

Table 3-2 Measurement of the geometry of the weld pool (in μm) with and without a natural oxide layer.

Surface condition	80 A, 4 mm/s		120 A, 4 mm/s	
	with oxide layer	without oxide layer	with oxide layer	without oxide layer
Topside width	3411	3483	5352	5480
Bottom side width	-	-	3858	3588
Depth	938	894	2473	2572

3.3.2 Different interrogation windows used in PIV

Displacement fields were compared for four different sizes of the final interrogation window using two instantaneous images chosen from a welding case worked with a current at 80 A and welding speed of 4 mm s^{-1} . Figure 3-7 a-d show the results for interrogation windows of 32×32 , 16×16 , 12×12 and 8×8 pixels respectively. It can be seen that details of the flow information are lost in Figure 3-7a when comparing the results to Figure 3-7 b-d, whilst many false vectors are observed in Figure 3-7d. The statistically averaged maximum velocity vectors based on these interrogation window sizes are plotted in Figure 3-8 for 50 consecutive vector fields. It can be seen that meshes at 32×32 or 8×8 pixels cannot describe the flow field accurately. The former is too coarse and detail is missed, whilst the latter is too small and delivers erratically varying velocity maxima; the computed flow field is therefore considered unreasonable. Thus, the results from the meshes of 16×16 or 12×12 pixels can be chosen to represent the surface flow.

Some errors can be expected in the measured results because the evaluation is based on a two dimensional flow field, whereas the real weld pool is three dimensional. The real velocity is $u = [(u_x)^2 + (u_y)^2 + (u_z)^2]^{0.5}$, the third dimensional velocity u_z was assumed to be much smaller compared to the in-plane velocities.

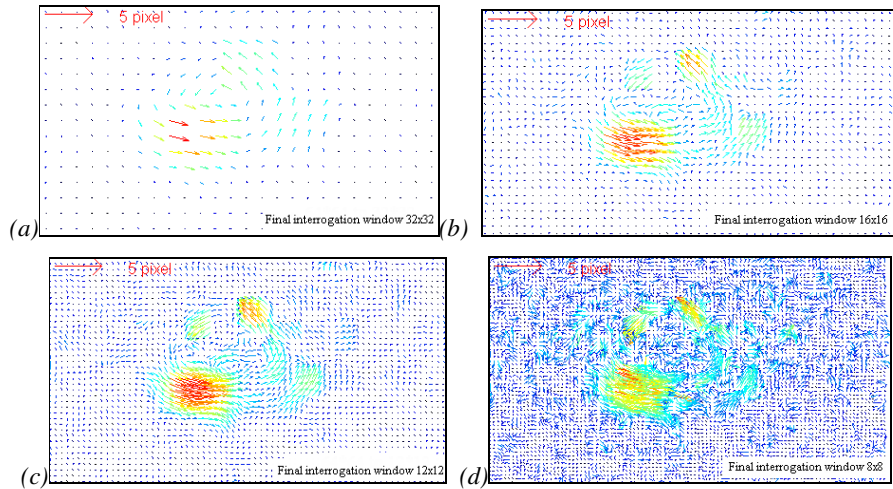


Figure 3-7 Instantaneous displacement fields for different sizes of the final interrogation window. The initial size of the interrogation windows was 64 pixels \times 64 pixels for all cases. The time between successive images was 0.002 seconds.

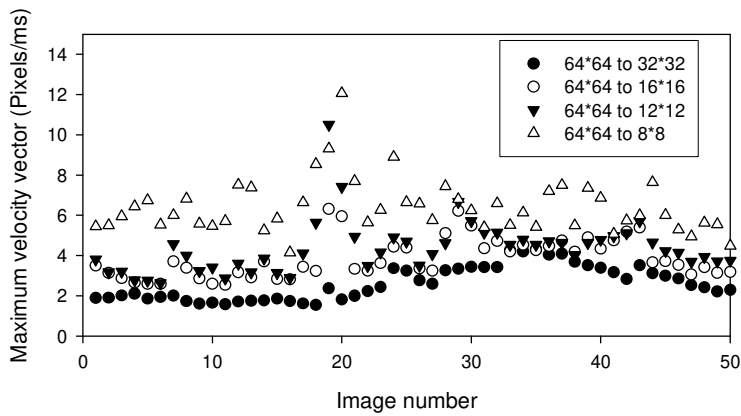


Figure 3-8 Maximum velocities computed from four different final interrogation windows for a set of 50 instantaneous velocity fields. The initial interrogation windows were 64 pixels \times 64 pixels.

3.3.3 Flow motion and velocity fields

As already indicated, fluid flow in the weld pool is a complex process since buoyancy, the Lorentz force, surface tension and arc shear stress can all drive the fluid flow. The electromagnetic force and surface tension are expected to dominate for the arc welding conditions examined.²⁰ The Lorentz force arises as a result of the current flow and self induced magnetic field. The surface tension is affected by the surface properties of the liquid metal, including the temperature distribution and the surface chemistry.

Three kinds of flow motion have been captured during welding; they are an outward surface flow, an inward flow and a multi-cell flow, some examples of which are shown in Figures 3-9 to 3-13. The images were acquired at a frame rate of 500 frames per second and evaluated with a final window size of 16 pixels \times 16 pixels. The weld pool region is masked as the computational zone (size 344 pixels \times 177 pixels) from the original image (size 512 pixels \times 512 pixels). Nearly all of the flows involve a rotational motion. For example in Figure 3-9 and Figure 3-11, the liquid metal is not moving directly from the centre of the pool to the boundary or from the boundary to the centre but follows a spiral path. At the beginning of a weld, the surface flow field is unsteady and changes frequently from one condition to another. After the welding condition reaches a steady state, two kinds of flow motion are mainly observed, *viz*: outward flow and rotational outward flow, as shown in Figure 3-9 and Figure 3-10, where the latter appears more often than the former. Possible reasons for unsteady flow are variations in arc forces due to surface changes at the tungsten cathode, variations in surface chemistry driven by the fluid flow, unsteady Marangoni forces induced by variations in the surface temperature distribution and unsteady Lorentz forces due to changes in the current path through the weld pool.

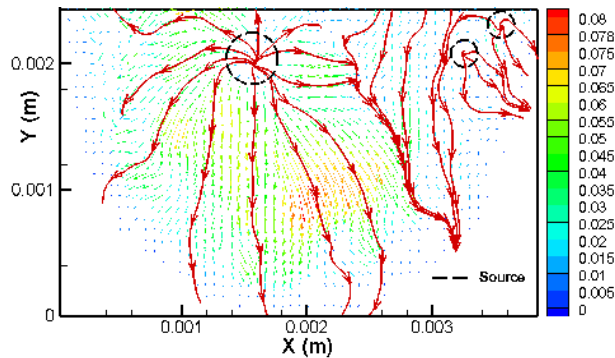


Figure 3-9 Outward fluid motion. The colour scale indicates the absolute velocity in ms^{-1} .

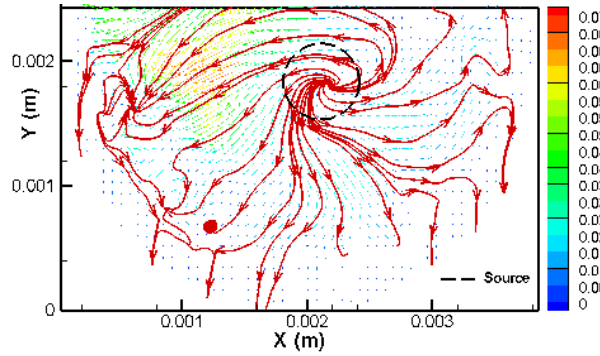


Figure 3-10 Rotational outward fluid motion. The colour scale indicates the absolute velocity in ms^{-1} .

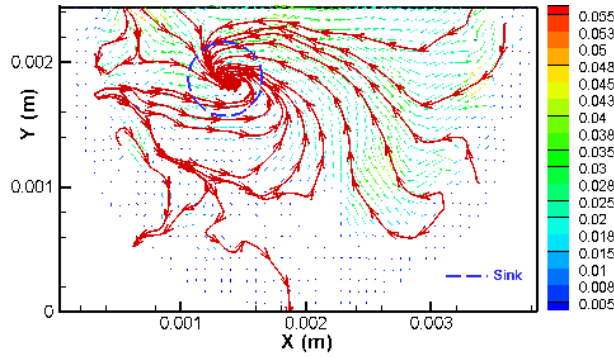


Figure 3-11 Inward fluid motion. The colour scale indicates the absolute velocity in ms^{-1} .

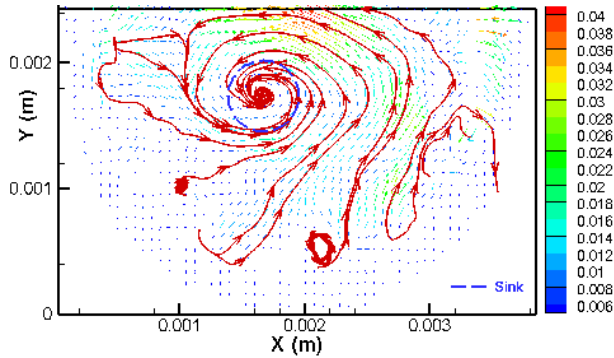


Figure 3-12 Rotational inward fluid motion. The colour scale indicates the absolute velocity in ms^{-1} .

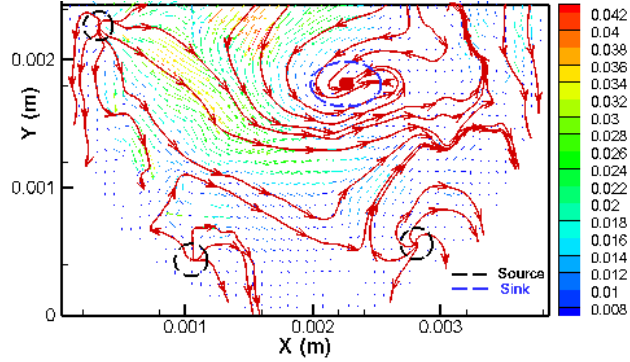


Figure 3-13 Multi-cell fluid motion. The colour scale indicates the absolute velocity in ms^{-1} .

After processing the velocity field, the maximum and average velocities on the weld pool surface were derived together with a Reynolds number as shown in Figure 3-14.

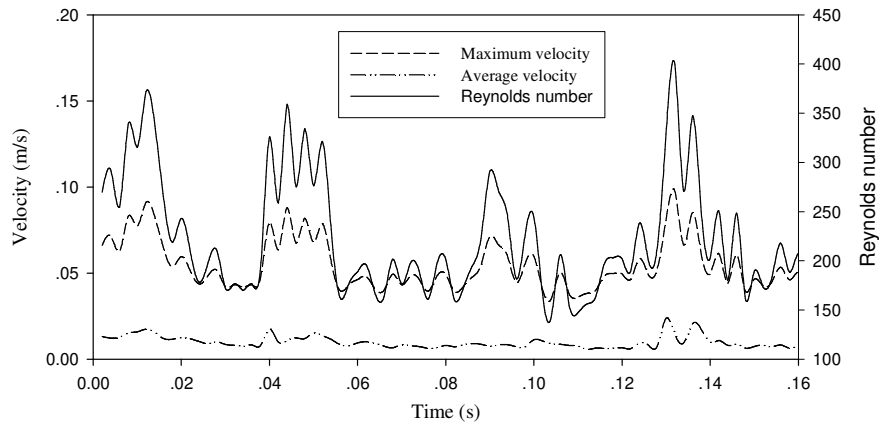


Figure 3-14 Velocities and Reynolds numbers calculated for a weld made at 80 A and 12 V, the welding speed is 4 mms^{-1} . Density, viscosity and characteristic length are 7660 kgm^{-3} , $0.006\text{ kgm}^{-1}\text{s}^{-1}$ and 3.5 mm respectively.

Velocity and Reynolds numbers, Re , were calculated from consecutive images, the latter being evaluated based on the maximum velocity according to

$$Re = \frac{\rho u_{\max} L}{\mu}, \quad (3.2)$$

where ρ is the density of the liquid metal in the weld pool, u_{\max} is the maximum velocity, L is a characteristic length and μ is the liquid metal viscosity (see Table 3-1).

Identification of the characteristic length can be problematic as the above expression is only strictly valid for flow in a pipe. The validity of a Reynolds number ascribed to a weld pool surface flow is questionable and caution should be exercised when interpreting the meaning. For the purposes of the present calculations, L is identified with the width of the pool, which is reasonable provided the flow involves a cooperative motion. For smaller scale flow features, L should be identified with a characteristic length of the feature. Use of the weld pool width will therefore overestimate the Reynolds number and values quoted in this work should be regarded as upper bounds.

3.3.4 Vortex forming and development

Rotational flow is maintained throughout nearly all of the weld progression, with alternating clockwise and counter-clockwise induced vortex development. This can be understood in terms of departure from an equilibrium condition. As shown in Figure 3-15a the left side and the right side flow from the centre to the boundary of the weld pool should be symmetrical when the magnetic field and surface tension are symmetrical between the left and right side. However, in many welding situations, slight perturbations lead to an asymmetry of the flow. With reference to Figure 3-15b, if the left hand vector I is stronger than the right hand vector II, a counter-clockwise vortex develops until it can block the outward flow from the centre of the pool. Subsequently, the outward flow pushes this vortex towards the rear of the weld pool, a new clockwise vortex develops from the right hand side flow (see Figure 3-15 e-f), and the behaviour is repeated (see Figure 3-15 f-j). The average frequency of this vortex formation process is observed to be in the range from 17 to 33 Hz.

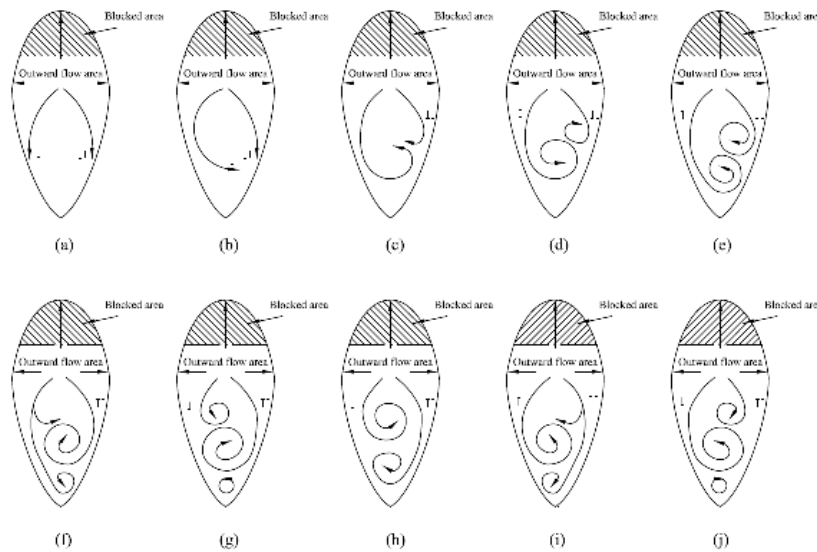


Figure 3-15 Schematic of vortex development.

3.3.5 Discussion

Flow patterns

Three major classifications of surface flow were observed; an outward flow field, an inward flow field and a multi-cellular field, all of which showed rotational flow for the majority of welding conditions examined. The multi-cellular field was observed at the start of the weld, whilst unsteady rotational flow dominated for the majority of the time. The unsteady flow field shows alternating vortex formation, development and dissipation at frequencies of a few tens of Hertz.

Rotational flow motions have been reported for most of the direct experimental observations; such as the circulation patterns reported by Lawson and Kerr,^{82,83} and weld pool shapes reported by Woods and Milner.¹² These authors also used a physical model (mercury) to study the flow motion of the simulated weld pool. The multi-cell flow motion shown in Figure 3-13 was captured at the start of a weld. Similar behaviour has also been reported by Kraus.¹⁶ who measured the surface temperature of a 200 A weld pool and showed a radial and angular dependence in the temperature profile.

Reynolds number

In order to describe fluid motion and its effects on heat transfer phenomena and ultimately the mechanical properties of the weld produced, a number of mathematical models have been developed, based on laminar⁸⁴⁻⁸⁷ or turbulent⁸⁸⁻⁹⁰ flow. Although many models have provided important physical insights into the mechanisms of weld pool development, it is still unclear whether the flow is laminar or turbulent. For numerical simulations it is necessary to choose a suitable model; laminar models or turbulent models⁹¹ can lead to significantly different results. In most cases, laminar flow has been assumed in the weld pool models,^{92,93} but this is questionable for two reasons: Firstly, the predicted weld pool depths are significantly larger than the measured penetration for comparable welding conditions, as reported by Choo and Szekely⁶³ and Hong *et al.*,⁹² whereas both of their turbulent models show better agreement. Secondly, visual observations of weld pools indicate unsteady, chaotic behaviour, which is associated with the transition to turbulence.⁶³ Thus both models and visual observations suggest that the flow in weld pools may not be fully laminar.

Evaluation of the Reynolds number⁹⁴ is commonly used to judge whether flow is laminar or turbulent. Malinowski-Brodnicka *et al.*⁶² measured the flow velocity in AISI 310 stainless steel weld pools and estimated the Reynolds number to be around 3,000. Comparing this value to the critical Reynolds number for pipe flow, $Re \approx 2300$ ⁹⁴ they suggested that fluid flow in their welds was probably turbulent. Choo and Szekely⁶³ reported typical Reynolds numbers around 4700 based on their turbulence model simulation. Nevertheless, relatively low Reynolds numbers (~107) have been reported by Delapp^{26,27} based on experimental observations. Some Reynolds numbers for weld pool flows reported in the literature are listed in Table 3-3. Normally, the Reynolds number was computed using the maximum velocity in the weld pool as the characteristic velocity, and the depth or width of the weld pool as the characteristic length.

In addition, different criteria for laminar to turbulent transition are often employed. Aboutalebi *et al.*⁹⁶ suggested that flow becomes turbulent if the Reynolds number is greater than 100; thus, arguments concerning whether flow is laminar or turbulent are based on criteria that are by no means universally established.⁹²

Even if the critical Reynolds number for the onset of turbulence is 2300;⁹⁴ the transitional Reynolds number may be much lower. The previous experimental studies of Atthey⁸⁴ and Joshi *et al.*⁹⁷ suggested that the effects of turbulence become prominent when the Reynolds number exceeds 600. The maximum value of Reynolds number shown in Figure 3-14 ranges from 250 to 400, which means that the flow is unsteady but not turbulent for the conditions examined in this study. The flow evolution observed on the pool surface also supports the unsteady characterisation.

Table 3-3. A summary of reported Reynolds numbers during welding.

Methods	Year	Re	Vmax(ms ⁻¹)	Materials	Results
Exp ⁵⁶	1990	3000	0.500	AISI310	Turbulent
Exp ^{26,27}	2005	107	0.0346	Carbon steel	
Num ⁸⁴	1980	200-600	0.105		Laminar
Num ⁸⁵	1983	2000-3000	1.259	Carbon steel	Laminar
Num ⁸⁶	1985	1300	3.000	AA6061	Laminar
Num ⁸⁷	1985	1400	0.250	AISI304	Laminar
Num ⁶³	1994	4700	0.7	AISI304	Turbulent
Num ⁹¹	2004	3000	0.08	Steel	Turbulent
Num ⁹⁵	1998	11000	1.22	Type 304	Turbulent

Maximum velocity

It is interesting to compare the measured velocities, with the prediction of Chakraborty *et al.*⁹⁸ based on a scaling analysis of the momentum and heat transport in gas tungsten arc weld pools. These authors find a maximum velocity due to surface tension flow of

$$u_{\max} = \sqrt{\frac{\partial\gamma}{\partial T} q / \rho\mu c_p} \quad (3.3)$$

where $\partial\gamma/\partial T$ is the temperature dependent coefficient of surface tension ($Nm^{-1} K^{-1}$), q is the effective heat flux (Wm^{-2}), and c_p is the specific heat capacity at constant pressure ($Jkg^{-1}K^{-1}$)

For the case⁹⁹ shown in Figure 3-6, the current is 80 A, the voltage is 12 V, and a process efficiency of 60% is assumed. The width of the weld pool is 3.5 mm, and using the physical properties from Table 3-1; the maximum velocity on the weld pool surface is 0.7 ms^{-1} . The measured velocities are on average an order of magnitude below this prediction, which may be related to the observed rotational motion, the temperature and hence surface tension gradient on the weld pool surface or the averaging procedures employed to derive the expression for u_{max} .

3.4 Measured case II, results and discussion

For measured cases II, the influence of a surface active agent was examined. The plate was first welded at a current of 80 A to induce oxygen dissolution in the weld pool. After cooling, the sample was re-welded along the same weld line. The high-speed camera was employed to capture the oxide particle motion, which was used to explore unsteady inward surface flow determined from oxide particle motion on the weld pool surface. The velocity field and vortex development based on PIV measurements are reported in this section.

3.4.1 Computational zone

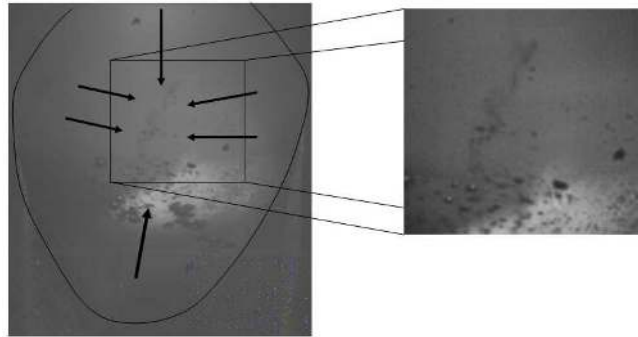


Figure 3-16 (Left) an image from the high speed camera showing the weld pool with arrows indicating the mean particle flow directions; (Right) a picture extracted from the left image that covers the interfacial region which forms the computational zone.

Since the surface tension gradient is negative in the presence of sufficient oxygen, an inward flow motion occurred, which induced particle movement from the boundary to the centre of the weld pool. This condition made it feasible to focus on the interfacial zone around the weld pool centreline, as shown in Figure 3-16. The picture on the left of this figure shows a view of the whole weld pool; particles moving from left and right meet at, or close to, the centreline; along a line that is designed as the interface. From the high-speed videos, it is observed that the inward flow fields result in unsteady flow at the interface, which may move some distance from the centre of symmetry line of the weld

pool. The right hand image shows the computational zone, which covers virtually the whole interface area. This region was chosen to capture the localised flow motion details.

Known scale meshes are used to calibrate the ratio between the real world system and the image pixel system. In the welding direction, 1 mm in a real world system corresponds to 48.90 ± 0.34 pixels on the high speed camera frames; perpendicular to the welding direction, 1 mm corresponds to 68.84 ± 0.42 pixels. Estimated standard deviations were computed from a group of calibration meshes.

3.4.2 Mesh selection

Four meshes were chosen to calculate the flow field and these are shown in Figure 3-17. The initial interrogation window is 64×64 pixels; Cases were tested for a fixed initial interrogation window and the final interrogation window size of 32×32 , 16×16 , 12×12 , and 8×8 pixels. Although the flow motion looks similar using these four different meshes, some information is lost in Figure 3-17a since the mesh is too large to capture the detailed flow information; however for smaller meshes as shown in Figure 3-17d, some fake vectors are computed, since there are no particles in some of the interrogation windows, which increases the velocity error; thus, only the final meshes at 16×16 pixels shown in Figure 3-17b and 12×12 pixels shown in Figure 3-17c are considered further here.

Statistical variations are shown in Figure 3-18 and Figure 3-19, which compare results obtained using the four meshes mentioned above. Figure 3-18 indicates the variation of the non-rejected vectors from one hundred successive vector fields. Fake or error vectors can be calculated if there are not enough particles or the image quality is poor in a mesh cell. For the present measurements, the particle distribution is not homogeneous, which leads to some computational difficulties. Figure 3-18 shows that nearly all the vectors can be obtained from the mesh when the final interrogation window is large, such as for the condition illustrated in Figure 3-17a, whilst with a decrease in size of the final interrogation window, the number of errors increases.

In Figure 3-19, the maximum velocity values based on pixels for one hundred successive vector fields, corresponding to the same series of images used to derive the data presented in Figure 3-18 are shown. With a decrease in the size of the final interrogation window, more detail of the flow information can be seen. However, it should be noted that the final interrogation window at 12×12 pixels is not directly half of mesh 32×32 pixels, which results in reduced stability compared with the 16×16 pixels. Therefore, the condition shown in Figure 3-17b with a 16×16 pixels interrogation window was chosen for analysis of the remaining experimental results.

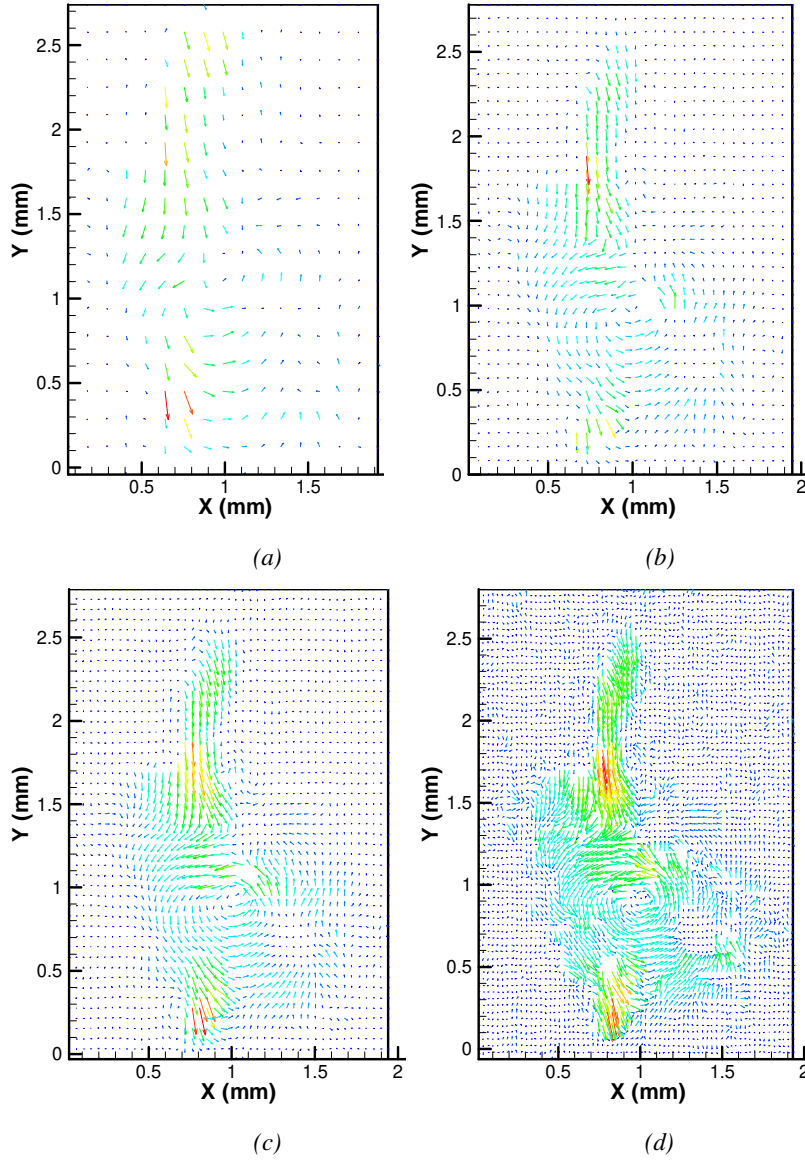


Figure 3-17 Flow fields derived from an initial interrogation window (64×64 pixels) and different final interrogation window of (a) 32×32 pixels (b) 16×16 pixels (c) 12×12 pixels.

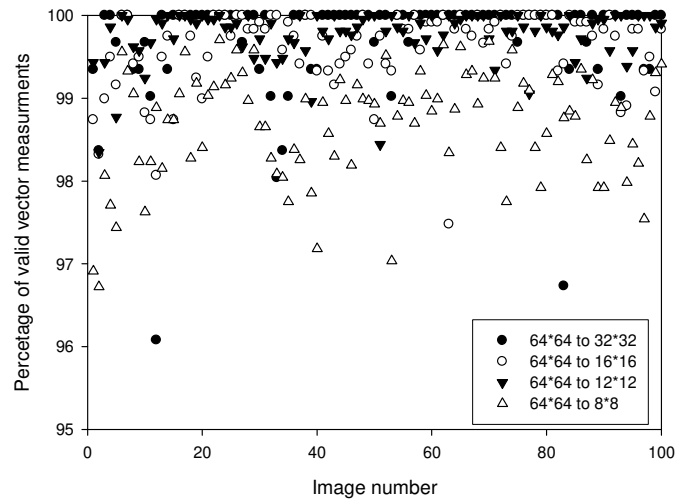


Figure 3-18 Percentage of valid velocity vectors from one hundred successive vector fields for different final interrogation window sizes.

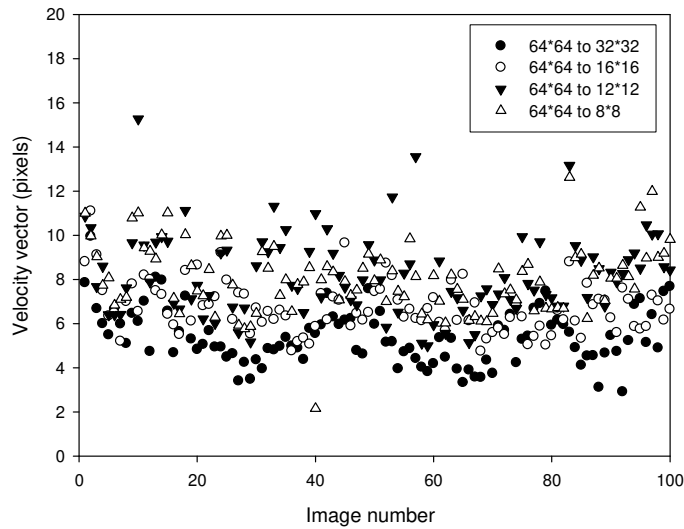


Figure 3-19 Maximum velocity values from one hundred successive vector fields based on different interrogation window size. Results correspond to the same data presented in Figure 3-18.

3.4.3 Flow instability

As shown in Figure 3-16, the surface tension drives the flow from the boundary toward the centre of the weld pool, this flow motion generates collisions of liquid streams from the left and right hand sides close to the centre line, resulting in the formation of an interfacial zone. The flow pattern at this interfacial zone is complex since the weld pool is not circularly symmetrical, as shown in Figure 3-20a, where the weld pool is divided into two parts labelled I and II. In zone I, the weld pool boundary describes more or less a half circle on the sample surface, whilst in zone II the shape is more elliptical.

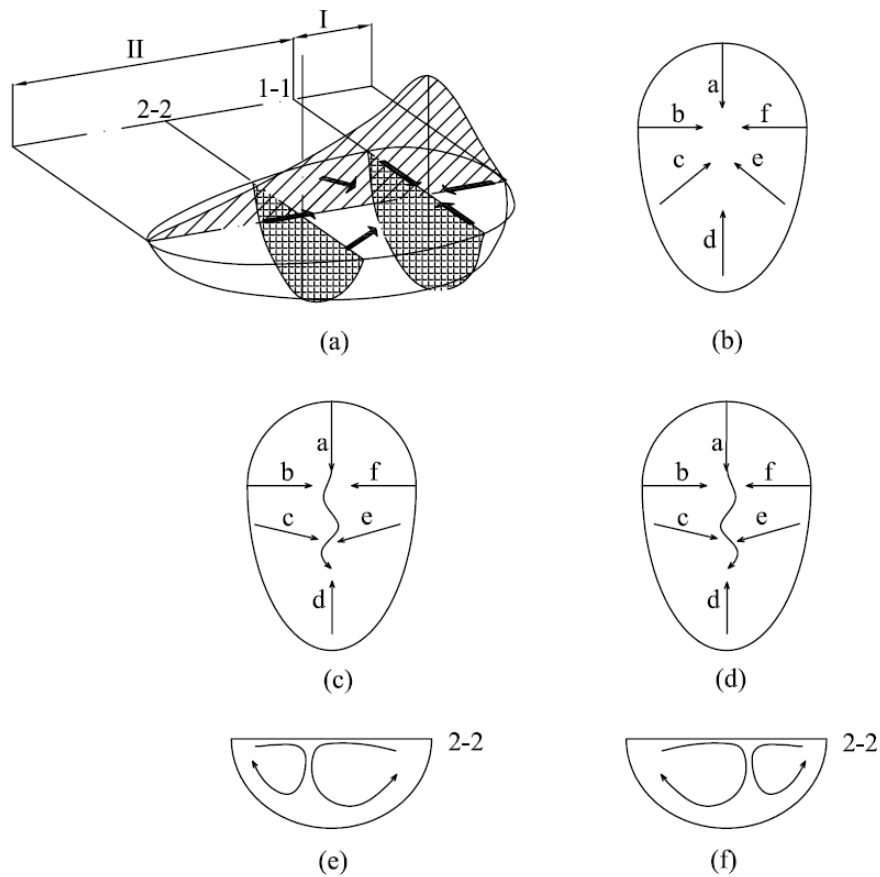


Figure 3-20 Weld pool surface shape (a) 3D shape of the weld pool (b) symmetrical flow motion on the weld pool surface, (c) and (d) illustration of observed flow motion captured from high speed camera images, (e) and (f) asymmetry inward flow inside the weld pool from cross section view.

For an ideal flow motion with negative surface tension gradient and a moving welding arc, the fluid flows from the boundary to the centre of the pool, as shown in Figure 3-20b. However, for a real condition, the weld pool shape and interface line follow the pattern shown in Figure 3-20c and d. Visual observations indicate that the interface is not a straight line, but a curve. This wavy interface is associated with periodic asymmetry in the weld pool flow as illustrated in Figure 3-20e and f, which schematically show the flow motion in a cross section through zone II (see Figure 3-20a).

The interface shows a strong unsteady wave like flow motion, and strong vortex flow motions were observed during welding at currents of 70 A, 80 A and 90 A at a welding speed of 4 mms⁻¹. The vortex flows became stronger with increasing current. Fluid from the front of the weld pool flows toward the rear following the wavy interface and collides with fluid flow from the rear of the pool resulting in vortex formation. The flow motion of these vortices varies frequently as illustrated schematically in Figure 3-20c and d. Thus the flow patterns are quite complex.

3.4.4 Flow motion and velocity field

Clockwise vortex

According to the flow patterns observed, three types of flow motion can be identified; the first is a clockwise vortex, the evolution of which is shown in Figure 3-21a-c for successive time steps of 1 ms. The colour of each vector represents the speed, with reference to the colour scale on the right hand side of each image, whilst the flow direction of the liquid and oxide particles is represented by the vector arrows. Since sufficient particles were only available near the interfacial zone, only these areas could be calculated with any confidence. The velocity field far from the interface shows a low value; however, due to the limited number of particles in these regions, the result is considered less reliable.

Counter clockwise vortex

The second flow pattern is a counter clockwise vortex and the evolution of the flow is shown in Figure 3-22. The flow motion was observed to change frequently from clockwise to counter clockwise flow, correspond to the asymmetry shown in Figure 3-20.

Symmetrical flow

Between the clockwise and counter clockwise flow motion, there is a short time period, during which a more or less symmetrical flow is observed, as shown in Figure 3-23. During this period, the fluid flowing from the front of the weld pool moves directly toward the rear and induces two nearly symmetrical vortices either side of the interfacial line.

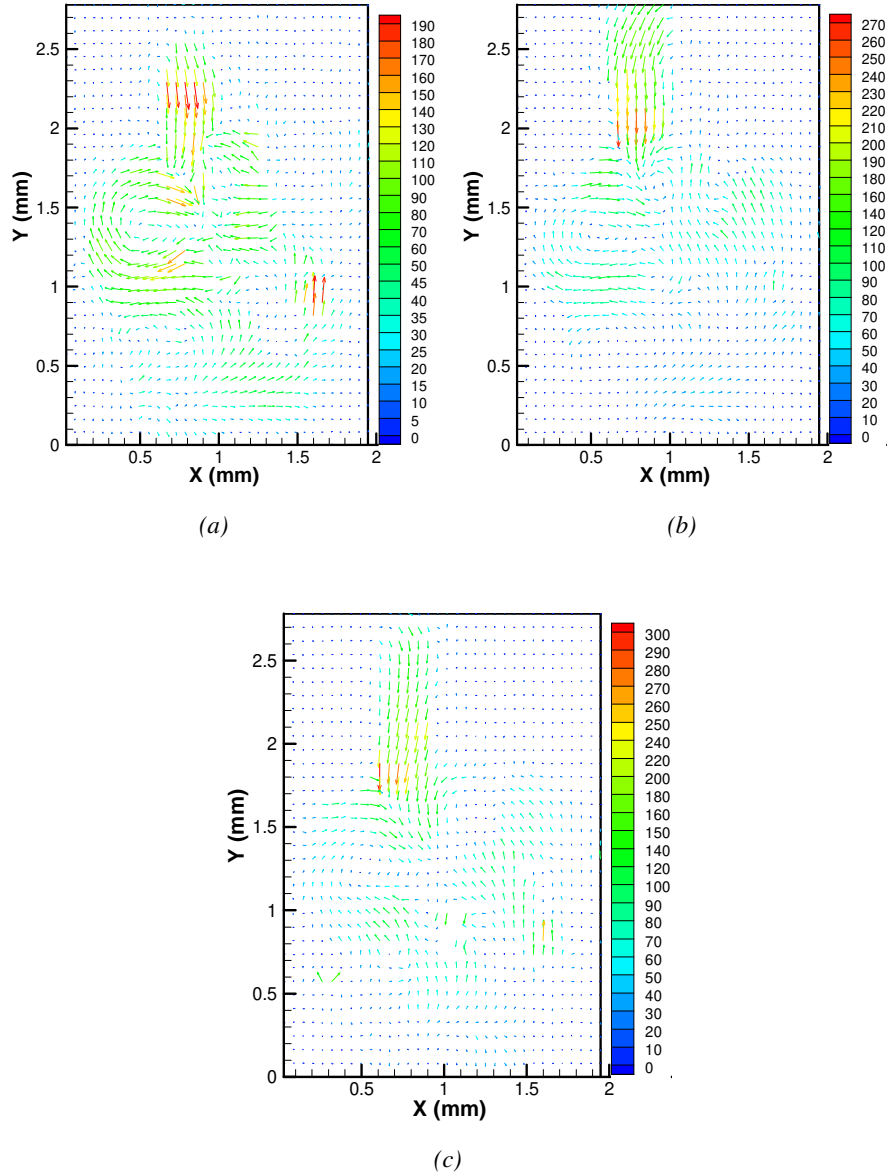


Figure 3-21 Clockwise flow motion, velocity field and vortex field (a) at time t . (b) at time $t+1ms$. (c) at time $t+2ms$.

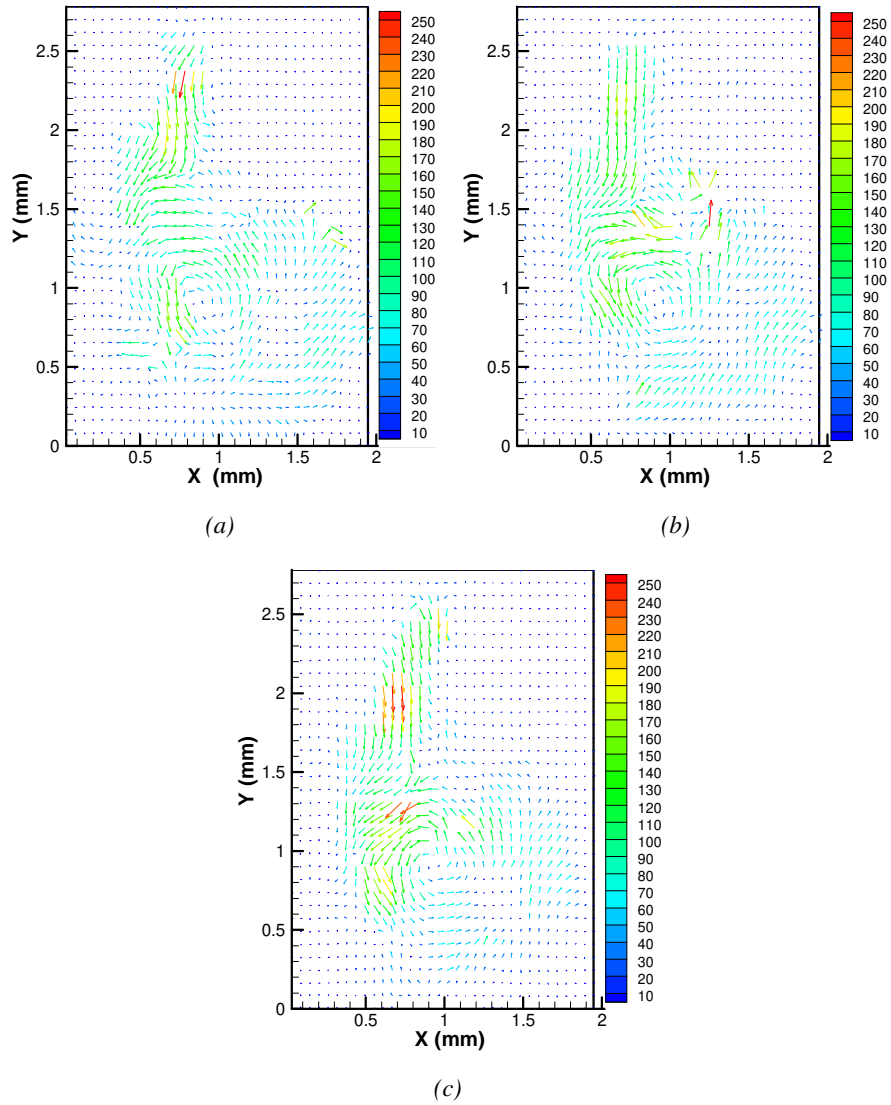


Figure 3-22 Counter clockwise flow motion, velocity field and vortex field. (a) at time t . (b) at time $t+1$ ms. (c) at time $t+2$ ms.

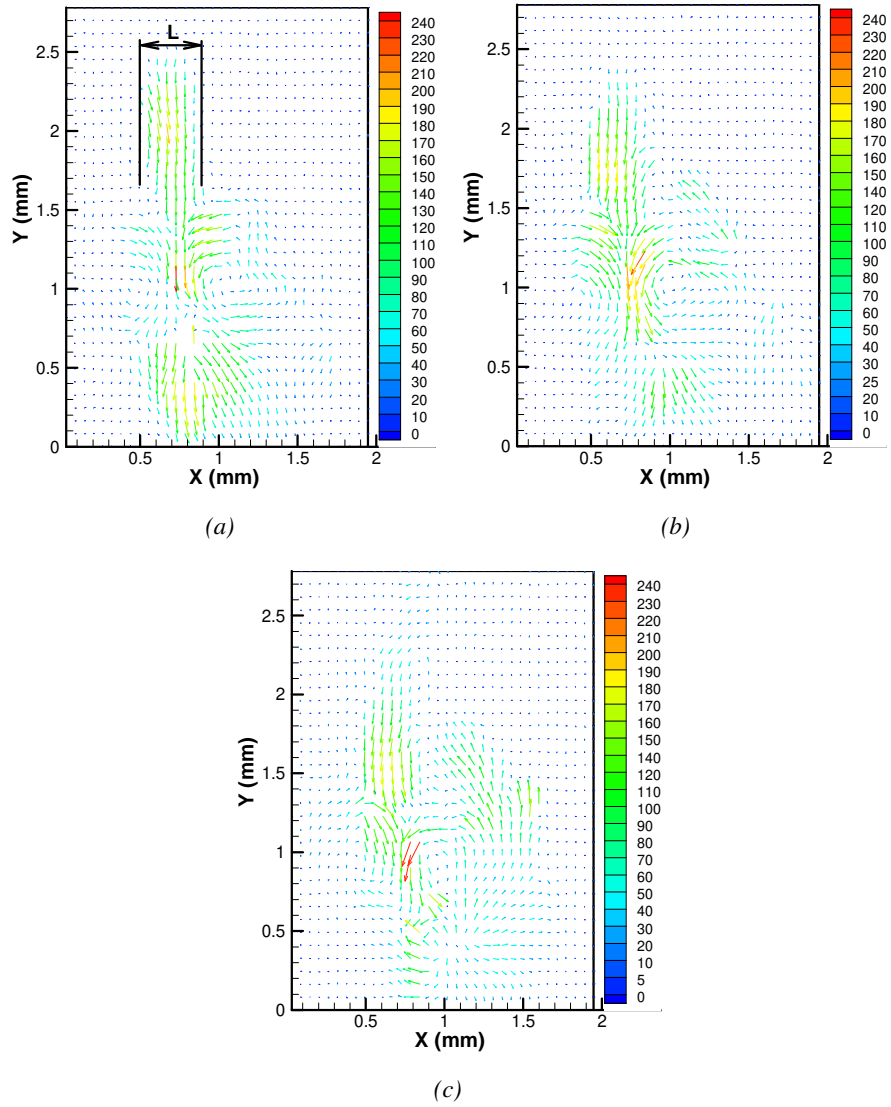


Figure 3-23 Transaction flow motion, velocity field and vortex field. (a) at time t . (b) at time $t+1$ ms. (c) at time $t+2$ ms.

3.4.5 Maximum velocity in the computational zone

The maximum velocity for one hundred successive velocity field images is shown in Figure 3-24. The highest velocity is nearly 400 mm s^{-1} , and the Reynolds number is about 1600 based on equation 3.1. Comparing with the result of 100 mm s^{-1} reported earlier⁹⁹ for nominally identical welding parameters, this value is nearly four times as high. One possible reason is that the surface tension is increased because of the presence of surface active oxides which act together with the electromagnetic force to drive flow inward.

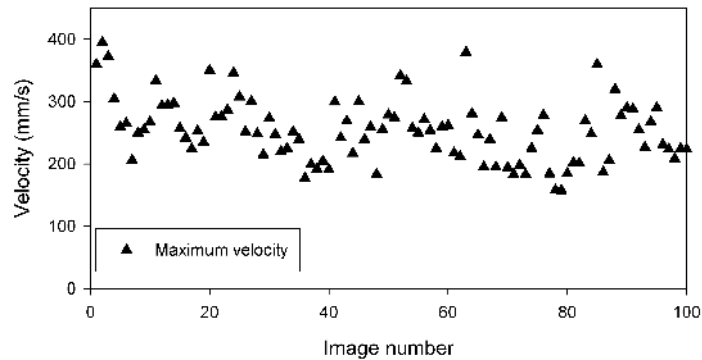


Figure 3-24 Maximum velocity values for successive hundred images in computational zone

3.4.6 Discussion

Surfactant effect

Surface active elements such as oxygen, sulphur and selenium can significantly change the weld penetration.¹⁰⁰ These elements change the temperature dependence of surface tension; often form a negative gradient for pure solvents to a positive gradient for binary systems.⁸⁰ In order to understand the relationship between surface active elements and surface tension, Heiple and Roper¹¹ used high speed filming of gas tungsten arc (GTA) welds to observe aluminium oxide powder motion on the weld pool surface and studied the effect of minor elements on fusion zone geometry. Sahoo *et al.*⁸⁰ studied surface tension as a function of temperature in Fe-O and Fe-S systems theoretically. Both works demonstrate the significant influence of surface tension.

Two main methods are used to change the surface tension, the first is adding active elements to the substrate, such as (SiO_2 ,¹⁰¹⁻¹⁰² TiO ,¹⁰³ TiO_2 ,¹⁰²⁻¹⁰⁴ Ti_2O_3 ,¹⁰³ Al_2O_3 ,¹¹ Fe_2O_3 ,¹⁰² sulphur,^{105,106} aluminium,¹¹ selenium,^{1,107} bismuth¹⁰⁸ or other materials such as AlF_3 , CaF_2 , Na_2WO_4 .¹⁰² The second method involves adding active materials in the shielding gas. For example Bad'yanov¹⁰⁹ added gaseous fluorides (BF_3 , WF_3 and SF_6) to argon to increase the penetration. Heiple and Burgardt¹¹⁰ studied the effect of adding SO_2 to the shielding gas, whilst mixtures of oxygen and argon and argon mixed with CO_2 were studied by Lu *et al.*¹¹¹⁻¹¹⁴

With such additions it is well known that the weld pool shape can be changed significantly, whilst heat input and other welding parameters remain constant. The induced change in surface tension modifies the fluid flow pattern resulting in changes in energy distribution compared to the flow pattern observed in the weld pool without surface additives.

Currently, numerical modelling is the primary method employed to study the effect of surface-active elements on fluid flow in the weld pool. Notable works on numerical modelling include the publications of Pitscheneder and co-workers,¹¹⁵ Wang and Tsai,¹¹⁶ Wang *et al.*,¹¹⁷ Zacharia *et al.*,¹¹⁸ Tanaka and Lowke,¹¹⁹ Zhang and Fan¹²⁰ and Kou and Wang.¹²¹ These authors employ symmetrical models to understand mass and energy transfer during welding. Sufficient attention has not yet been paid to the asymmetrical flow motion and its influences on welding.

Flow motions

One possible reason for the change from clockwise to counter clockwise flow is minor instabilities in the position of the arc or unsteady fluid motion. Once triggered, the wavy interface motion appears to be self-perpetuating, which may be related to an asymmetric surface tension as illustrated by vectors *c* and *e* in Figure 3-25a, where a clockwise vortex is formed, and in Figure 3-25c where a counter clockwise vortex occurs. A combination of surface tension and fluid momentum drives the flow from one state to the other and back again, passing through the symmetrical state Figure 3-25b in the intervening period.

Another possible reason is that these flow instabilities are characteristics of the fluid itself. The main mechanisms are not yet clear. The development of a numerical simulation to explain the detailed physics of this flow would be helpful both for our understanding and also for control of fluid flow in the pool.

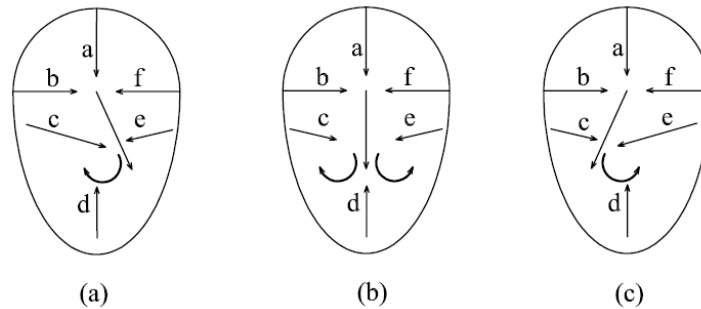


Figure 3-25 Flow motions corresponding to clockwise vortex, symmetry vortex and counter clockwise vortex.

Interfacial phenomena

Although reports on interfacial phenomena have been included in many references,^{11,88,100,103,107,110,117,119} there are few studies which provide quantitative experimental evidence of the surface velocity field. Zacharia and co-workers¹²² noted the interfacial behaviour and studied this by numerical simulation, showing that it has a significant influence on the development of the weld pool. The effect of surface active elements on interfacial phenomena is a strong function of surface temperature and hence the welding parameters.

In the present work, not only does the interface show an unsteady wavy structure, but also some of the liquid metal from the front of the weld pool follows this interface and arrives at the rear of the weld pool. This aspect of the flow motion has not yet been reported, as simulations did not consider the wavy interface. In welding practice, this unsteady interface could affect both heat and mass transfer.

In order to evaluate the quantitative mass transfer along the interface, reference is made to the simple sketch shown in Figure 3-26. The symbol m indicates the flow rate from the front to the back of the weld pool transported along the interface. The depth of the boundary layer is denoted by δ , and Equation 3.4 is used to compute δ for laminar flow conditions.¹²³ The flow condition could be turbulent according to the critical surface Reynolds number of 100 mentioned by Aboutalebi *et al.*¹²⁴ and Bejan,¹²⁵ but this is not taken into account for the present work. The mass flow rate along the interface can be obtained from the following equation:

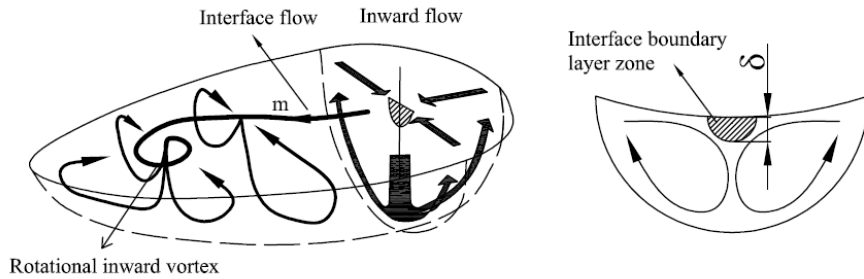


Figure 3-26 Mass flow in the interfacial area

$$\begin{aligned} \delta &= 5 \sqrt{\frac{\nu L}{u_m}} \\ &= 0.22 \times 10^{-3} m \end{aligned} \tag{3.4}$$

where ν is kinematic viscosity $\nu = \mu / \rho$, $\mu = 0.006 \text{ kg} \cdot \text{m}^{-1} \text{ s}^{-1}$, $\rho = 7660 \text{ kgm}^{-3}$, L is a characteristic length; here identified as the width of the interface flow, $L = 5 \times 10^{-4} \text{ m}$ as measured from Figure 3-23. Using $u_m = 0.200 \text{ ms}^{-1}$ as the mean flow velocity

$$\begin{aligned}
 m &= \rho \cdot S \cdot \bar{u} \\
 &= \rho \cdot \frac{1}{2} \pi \delta L \cdot \bar{u} \\
 &\approx 0.27 \times 10^{-3} \text{ kg s}^{-1}
 \end{aligned} \tag{3.5}$$

where S is cross sectional area of the interfacial zone, and $\bar{u} = 0.5 \times U_m$ is the average velocity inside the boundary layer.

The total liquid mass in the weld pool zone I (see Figure 3-20a) can be calculated from equation 3.6. Zone I is assumed to be half of a segment of a sphere for partial penetration welding.

$$\begin{aligned}
 m_{total} &= \rho \cdot V \\
 &= \rho \cdot \frac{1}{2} \cdot h \cdot \pi \frac{(3D^2 + 3d^2 + h^2)}{6} \\
 &\approx 0.44 \times 10^{-3} \text{ kg}
 \end{aligned} \tag{3.6}$$

where $h=2 \text{ mm}$ is the thickness of sample, $D=4.9 \text{ mm}$ and $d=3.4 \text{ mm}$ are the weld pool top and bottom width respectively measured from sectioned weld samples.

Comparing the mass flow rate from equation 3.5 and total mass in weld pool zone I, it is clear that this flow rate is significant. In reality the mass flow rate along the interface is larger than the value computed above because it also receives contributions from the side flows, as indicated by vectors c and e in Figure 3-20 (c) and (d).

From the above calculations, it can be seen that although the interface flow area is narrow, the flow rate is high enough to affect the mass transfer during welding. Because the temperature of this region is quite high, the interface flow is responsible for transporting both mass and heat from the centre of the weld pool, and should be considered when studying the fluid hydrodynamics in the weld pool.

The interface behaviour described is responsible for asymmetry in the weld pool fluid dynamics. As a result solidification is also likely to experience some asymmetry in local conditions which is not considered by current numerical models.

3.5 Conclusion

A high speed camera system was used to visualize the weld pool surface flow during GTA welding of 316L stainless steel. The velocity field has been calculated based on a PIV technique using oxide particles as tracers.

For test case I, three major classifications of surface flow were observed; an outward flow field, an inward flow field and a multi-cellular field, all of which showed rotational flow for the majority of welding conditions examined. The multi-cellular field was observed at the start of the weld, whilst unsteady rotational flow dominated for the majority of the weld time. This unsteady flow field shows alternating vortex formation, development and dissipation at frequencies of a few tens of Hertz. The maximum surface velocity calculated from the flow field, assuming a two-dimensional flow, is of the order 0.1ms^{-1} , with corresponding maximum Reynolds number of about 400, which is consistent with the unsteady flow classification.

For the test case II, this quantitative method was used to study weld pool fluid flow interface phenomena during welding with surface active components. The interface flow shows strong wavy properties and oscillates around the centreline of the weld pool. The interface flow is associated with strong vortex flow, which changes between a clockwise and a counter clockwise motion. The heat and mass transportation together with the solidification processes will be influenced by the unsteady nature of the interface flow. This study highlights weld pool fluid flow complexity and results are expected to prove useful for validation of numerical flow models.

The PIV method has been found to be an efficient method to quantitatively study the fluid flow. It can provide both flow patterns and velocity fields, which are useful for validation of future numerical results.

4 Three dimensional velocity measurements

Measurement and sensing of the weld pool features is the key to controlling the welding process.⁴⁴ As a non-contact method, vision technology is still the main approach employed to obtain quantitative results during welding, since contact measurements for capturing the thermal or fluid parameters in the weld pool are nearly impossible.

Experimental methods have been developed to study flow motion in welding, and most works are based on surface flow measurements. Examples include Delapp^{26,27} and Henrikson,²⁴ who studied the surface flow velocity by tracing seed particle flow using high speed video. For bulk flow observations, high energy X-rays have been used to image tungsten particle flow and porosity formation inside a weld pool by Matsunawa and co-workers,³¹⁻³³ these results are based on two dimensional measurements.

In chapter 3, two dimensional particle image velocimetry (PIV) was employed to compute the whole weld pool surface velocity field by tracing oxide particle flow. However, the real weld pool surface is not flat but a three dimensional curved surface, induced by surface tension, and changing due to surface oscillations. Therefore, 2D PIV is limited to conditions when the top surface of the weld pool is nearly flat or can be assumed to be flat. Information from the third dimension is missed in two-dimensional measurements, which can result in significant errors under some conditions.

Mnich *et al.*¹²⁶ reconstructed three dimensional weld pool surfaces using stereovision. Choong and Jihye¹²⁷ employed a stereo system based on a single CCD camera with a single lens fitted with biprism to acquire three-dimensional information.^{128,129} Zhao and co-worker⁴¹ studied three-dimensional reconstructions for a weld pool based on two-dimensional images. However, three dimensional reconstructions using two or more cameras can be limited for the following reasons: (a) Cost: high-speed cameras will increase the system cost if two or three cameras are required. (b) Complexity: to remove strong radiation from the weld pool or arc illumination, two or more filters are necessary, and synchronization is required to control these cameras. (c) Target size: the width of a normal weld pool is about 3-10 mm, which provides limited space to arrange the observation equipment. (d) Working condition: the welding process usually produces fume and sometimes spatter. As a result, most of the reported data for three dimensional measurement methods are based on a single camera system. However, there are no reported works that evaluate the three dimensional velocity on the weld pool surface.

In this chapter, a single high speed video camera with a stereo adapter is employed to make a 3D surface measurement. The adapter comprises two groups of parallel mirrors that can capture two images in the same frame from two different viewpoints. Three-dimensional velocity was reconstructed using one frame, based on mathematical models of machine vision.

4.1 Measurement description

4.1.1 Experimental arrangement

The system arrangement is shown in Figure 4-1 where the optical device consists of a CMOS high speed camera (Phantom V5), a Pentax stereo adapter (49 mm), a Nikon 70-300 mm optical lens, some 62 mm close up lenses and adapter rings.

A camera speed of 4,000 frames per second was employed to capture sufficiently clear detail of the weld pool surface. Each frame size was 1204 pixels \times 256 pixels and the exposure time was 14 μ s. A pair of weld pool images was captured on the left and right side of each frame.

Welding was carried out using an Nd-YAG laser in the heat conduction mode; the maximum output power is 3000 W. The measured case considered here involves a stationary spot weld made with a beam power of 3000 W for a duration of 2 s. The weld pool is open to the environment without any shielding gas, which induces inward flow motion to produce a concave weld pool surface, since oxygen influences the surface tension gradient. Oxide particle velocity is assumed to represent the liquid metal flow velocity on the weld pool surface. Welding was carried out on a type 304L stainless steel sample of size 50 mm \times 50 mm \times 2 mm.

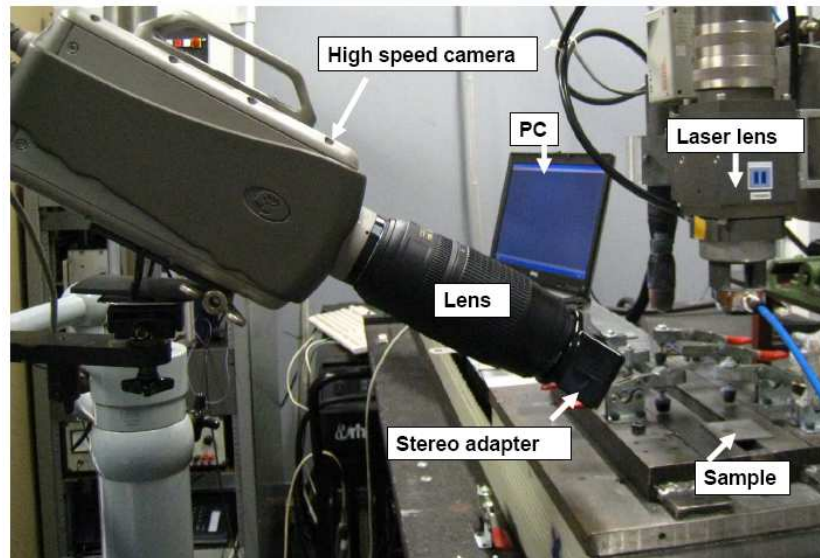


Figure 4-1 Observation system.

4.1.2 Structure of the stereo adapter

The geometric structure of the stereo adapter as shown in Figure 4-2 consists of two groups of parallel mirrors arranged symmetrically with respect to the observation centre line. Light from an object placed in front of the adapter is reflected firstly by the longer mirror, and then reflected again by the shorter mirror into the camera lens. Since the arranged angle of these mirrors affects the reflection direction, there are three observation zones, designated I, II, III as shown in Figure 4-2. Only one image can be captured by the camera if an object is placed in zone II, two images are available in zone I, whilst no image is available in zone III. The focus length should be beyond the cross point P to capture clear dual images. Both views can then be seen by a single camera to view the object from different angles. Thus, three-dimensional information can be reconstructed from these two images according to machine vision theory.

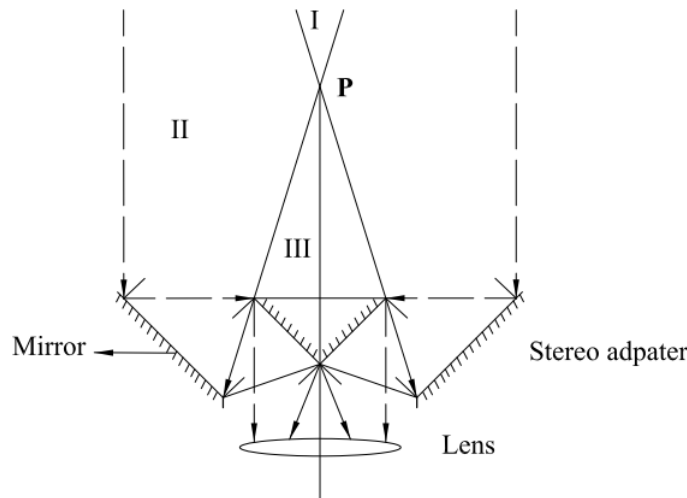


Figure 4-2 Structure of the stereo adapter.

4.1.3 Geometric relationship between the image and spacial coordinate systems

In order to understand this stereo system mathematically, firstly, four coordinate systems are introduced, which are shown in Figure 4-3. They are the world Euclidean coordinate system with subscript w , the camera Euclidean coordinate system with subscript c , the image Euclidean coordinate system in 2D, uOv , and the image affine coordinate system $xO'y$.

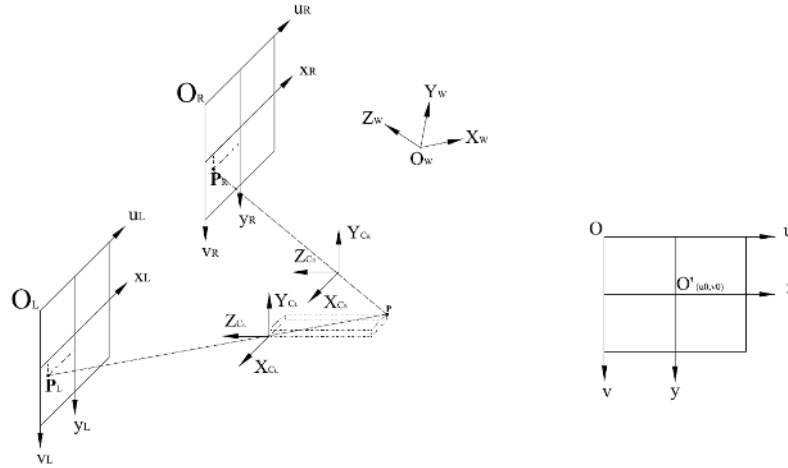


Figure 4-3 Geometric relationships between the world coordinate system (W), camera coordinate system (C) and image coordinate system.

The image Euclidean and image affine coordinate systems, are in the same plane but have different origins. If point $O'(u_0, v_0)$ in the image Euclidean coordinate system is the origin of the image affine coordinate system, then the coordinate of any point $P_i(u_i, v_i)$ in the image Euclidean coordinate system uOv can be expressed as

$$\begin{cases} u_i = \frac{x_a}{dx} + u_0 \\ v_i = \frac{y_a}{dy} + v_0 \end{cases}, \quad (4.1)$$

where dx and dy are the physical scales of each pixel. Equation 4-1 can be rewritten in matrix form as

$$\begin{bmatrix} u_i \\ v_i \\ 1 \end{bmatrix} = \begin{bmatrix} \frac{1}{dx} & 0 & u_0 \\ 0 & \frac{1}{dy} & v_0 \\ 0 & 0 & 1 \end{bmatrix} \begin{bmatrix} x_a \\ y_a \\ 1 \end{bmatrix}. \quad (4.2)$$

A pinhole model is used to express the relationship between the image Euclidean

coordinate system and the camera Euclidean coordinate system. As shown in Figure 4-3, point $P_c(X_c, Y_c, Z_c)$ in the camera Euclidean coordinate system is projected onto the left image as point P_L and right image as point P_R . Assuming that f is the focal length, then equation 4.3 can be used to express the projection relationship for point $P_c(X_c, Y_c, Z_c)$ in each camera Euclidean coordinate system and the image affine coordinate system, based on similar-triangles, where (x_a, y_a) is the coordinate in the image affine coordinate system,

$$\frac{f}{Z_c} = \frac{x_a}{X_c} = \frac{y_a}{Y_c}, \quad (4.3)$$

which can be rewritten as

$$Z_c \begin{bmatrix} x_a \\ y_a \\ 1 \end{bmatrix} = \begin{bmatrix} f & 0 & 0 & 0 \\ 0 & f & 0 & 0 \\ 0 & 0 & 1 & 0 \end{bmatrix} \begin{bmatrix} X_c \\ Y_c \\ Z_c \\ 1 \end{bmatrix}. \quad (4.4)$$

There is a unique relationship between the world and each camera coordinate system, given by the Euclidean transformation consisting of a translation $T(1 \times 3)$ and rotation $R(3 \times 3)$ matrix expressed by

$$\begin{bmatrix} X_c \\ Y_c \\ Z_c \end{bmatrix} = \begin{bmatrix} R & T \\ 0 & 1 \end{bmatrix} \begin{bmatrix} X_w \\ Y_w \\ Z_w \\ 1 \end{bmatrix}. \quad (4.5)$$

Equations 4.2, 4.4 and 4.5 represent all the relationships between the four coordinate systems, the relationship between the image coordinate system and the world Euclidean coordinate system can therefore be expressed as

$$Z_c \begin{bmatrix} u_i \\ v_i \\ 1 \end{bmatrix} = \begin{bmatrix} \alpha_x & 0 & u_0 & 0 \\ 0 & \alpha_y & v_0 & 0 \\ 0 & 0 & 1 & 0 \end{bmatrix} \begin{bmatrix} R & t \\ 0 & 1 \end{bmatrix} \begin{bmatrix} X_w \\ Y_w \\ Z_w \\ 1 \end{bmatrix} = M_1 M_2 P_w = M P_w, \quad (4.6)$$

where M is a 3×4 matrix, M_1 is a 3×4 intrinsic matrix, M_2 is a 4×4 extrinsic matrix. A calibration process will be introduced in the following steps to obtain the unknown parameters in matrix M .

4.1.4 Stereo point reconstruction

Both left and right side views can be processed using equation 4-6 viz:

$$Zc_1 \begin{bmatrix} u_1 \\ v_1 \\ 1 \end{bmatrix} = \begin{bmatrix} m_{11}^1 & m_{12}^1 & m_{13}^1 & m_{14}^1 \\ m_{21}^1 & m_{22}^1 & m_{23}^1 & m_{24}^1 \\ m_{31}^1 & m_{32}^1 & m_{33}^1 & m_{34}^1 \end{bmatrix} \begin{bmatrix} X_w \\ Y_w \\ Z_w \\ 1 \end{bmatrix}, \quad (4.7)$$

$$Zc_2 \begin{bmatrix} u_2 \\ v_2 \\ 1 \end{bmatrix} = \begin{bmatrix} m_{11}^2 & m_{12}^2 & m_{13}^2 & m_{14}^2 \\ m_{21}^2 & m_{22}^2 & m_{23}^2 & m_{24}^2 \\ m_{31}^2 & m_{32}^2 & m_{33}^2 & m_{34}^2 \end{bmatrix} \begin{bmatrix} X_w \\ Y_w \\ Z_w \\ 1 \end{bmatrix}. \quad (4.8)$$

Eliminating Zc_1 and Zc_2 yields

$$\begin{cases} (u_1 m_{31}^1 - m_{11}^1)X + (u_1 m_{32}^1 - m_{12}^1)Y + (u_1 m_{33}^1 - m_{13}^1)Z = m_{14}^1 - u_1 m_{34}^1 \\ (v_1 m_{31}^1 - m_{21}^1)X + (v_1 m_{32}^1 - m_{22}^1)Y + (v_1 m_{33}^1 - m_{23}^1)Z = m_{24}^1 - v_1 m_{34}^1 \\ (u_2 m_{31}^2 - m_{11}^2)X + (u_2 m_{32}^2 - m_{12}^2)Y + (u_2 m_{33}^2 - m_{13}^2)Z = m_{14}^2 - u_2 m_{34}^2 \\ (v_2 m_{31}^2 - m_{21}^2)X + (v_2 m_{32}^2 - m_{22}^2)Y + (v_2 m_{33}^2 - m_{23}^2)Z = m_{24}^2 - v_2 m_{34}^2 \end{cases}, \quad (4.9)$$

where u_1, v_1 and u_2, v_2 can be obtained from the images, and X, Y and Z represent the real 3D coordinates in the world coordinate system. Calibration is required to determine $m_{i,j}^k$ ($i=1,2,3; j=1,2,3,4; k=1,2$). When these are known, a 3D coordinate in the world coordinate system can be computed for any pair of coordinate points $(u_1, v_1), (u_2, v_2)$ from the image Euclidean coordinate system.

4.2 3D reconstruction

4.2.1 Calibration

A self-calibration model was used to calibrate the left and right view using checker-board meshes of known dimensions. Images were captured from different angles to obtain the corresponding relationship between the image Euclidean coordinate system and world Euclidean coordinate system, these images are placed at different inclinations to the

camera, to calibrate a larger space covering the weld pool size. Three calibration cases are shown in Figure 4-4a, for which the corners of diagonally adjacent black squares were selected as calibration points. A total of 117 points were employed for each calibration plate (Figure 4-4b). A Matlab toolbox¹²⁹ was used to calibrate the intrinsic and extrinsic matrix of this system for both left and right views. The left top corner is considered as the origin point of the calibration plate. The origin point and three coordinate axis of the world coordinate system are chosen as shown in Figure 4-4b. In this work, to simplify the reconstruction process, the distortion is not considered during the three-dimensional reconstruction, since no obvious skew is found in the current calibration.

4.2.2 Match and Correspondence

The correspondence between left and right images is evaluated by using the correlation coefficient¹³⁰ shown in equation 4.10.

$$\text{Coeff} = \frac{\sigma_{LR}^2}{\sqrt{\sigma_L^2 + \sigma_R^2}}, \quad (4.10)$$

where the gray variances of the left and right views are given by,

$$\sigma_K^2 = \sum_{i=1}^n \sum_{j=1}^m [I_K(i, j) - \mu_K]^2 / (N_m \times N_m), \quad (4.11)$$

where K is either L or R and

$$\sigma_{LR}^2 = \sum_{i=1}^m \sum_{j=1}^n \{ [I_L(i, j) - \mu_L][I_R(i, j) - \mu_R] \} / (N_m \times N_m), \quad (4.12)$$

is the covariance between $I_L(i, j)$ and $I_R(i, j)$. $I_K(i, j)$ is the intensity value at point (i, j) and μ_K is the average intensity value in the correlation window.

For any point P_L in the left image, a match window around this point was chosen of size $(2N_m + 1) \times (2N_m + 1)$ pixels, and then a larger area of size $(2N_s + 1) \times (2N_s + 1)$ pixels was selected as the search window as shown in Figure 4-5. Point P_R was chosen as the corresponding point when it had the highest correlation coefficient in the search window correlating with P_L . The size of the search window should be large enough to cover the potential matching point.

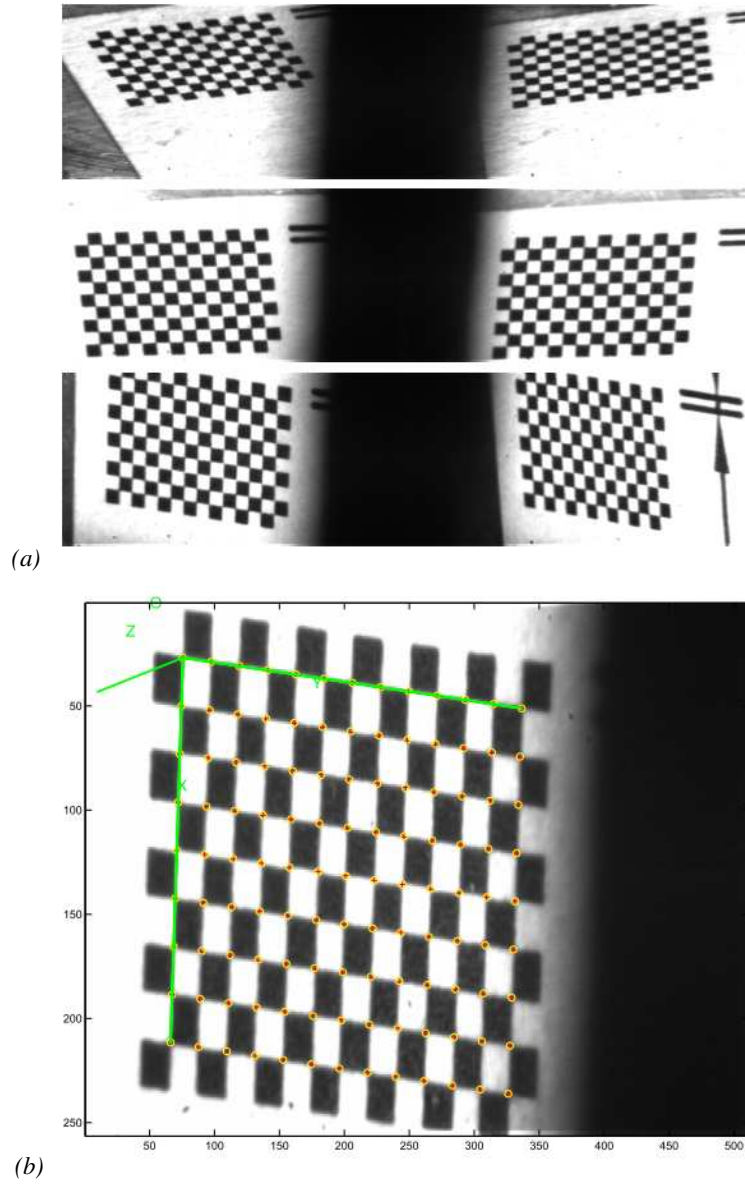


Figure 4-4 Calibration. (a) three of the calibration images. (b) the world Euclidean coordinate system.

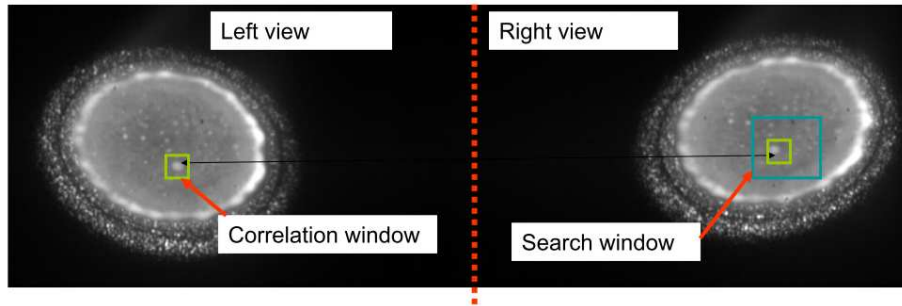


Figure 4-5 Point matching in left and right stereo images.

4.3 Results and Discussion

4.3.1 Error analysis

In order to evaluate the precision of the current system, additional images were captured from another five random different angles (named groups 1 to 5), to compare the real dimensions with reconstructed 3D lengths using the above method. The measured width of each mesh square is 0.656 ± 0.014 mm.

Figure 4-6a shows the pixel coordinates in the image coordinate system and Figure 4-6b the reconstructed 3D-coordinates in the world coordinate system. The reconstructed 3D width of each mesh is shown in Figure 4-6c. The average measured widths for the five groups are 0.581 mm, 0.815 mm, 0.776 mm, 0.683 mm and 0.560 mm. For each group, 8 values in the X direction along 13 square boundaries in the Y direction are reconstructed to compare with the measured width. Totally, 104 values are reconstructed as shown in Figure 4-6c. The precision is different for each test case; group 4 has highest precision and group 2 the lowest. From the 2D image in Figure 4-6b, group 4 shows a small inclination compared with the other images, indicating that precision is reduced when the inclination of the studied object is too great. For the current weld pool flow velocity reconstruction, an inclination similar to that represented by group 1 is employed; group 1 was placed horizontally and inclined to the camera at an angle of 45° ; the absolute error is 0.075 mm, representing a reconstruction error of 11.4%.

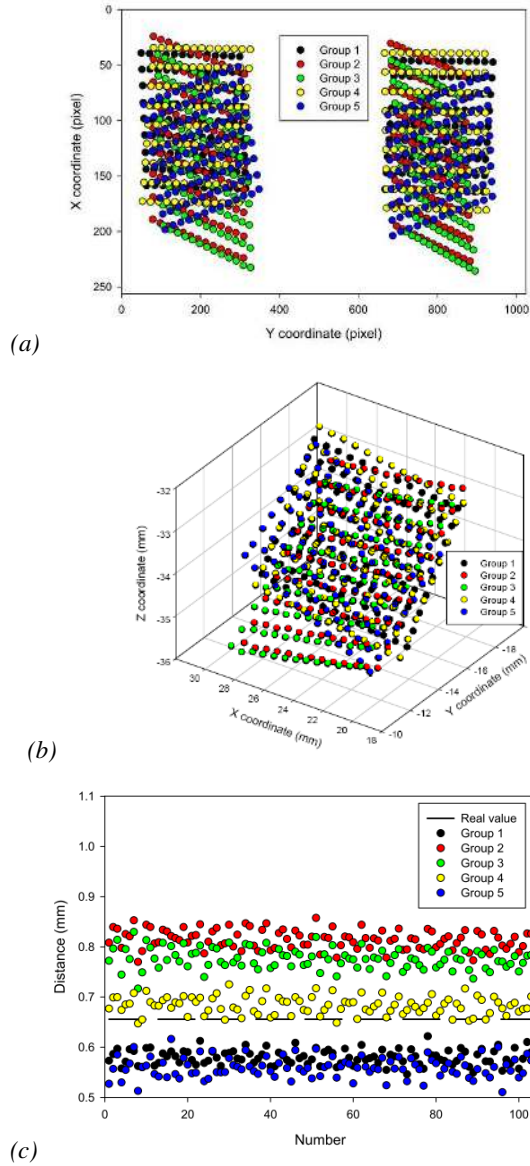


Figure 4-6 Error analysis for five different inclination angles (a) extracted 2D coordinates in the left and right image coordinate systems, (b) computed 3D coordinate in the world coordinate system, (c) measured distances as a function of real distance for each mesh point.

4.3.2 Two and three dimensional velocity (measured case)

Based on the above calibration results, a laser spot weld was measured by tracking surface oxide particle flow. The particle displacements dependent on time are shown in Figure 4-7, where the time step between successive image pairs is 1 millisecond. Five images show particle movement following an inward liquid flow pattern because of a positive surface tension gradient. The inward flow motion makes the weld pool surface concave.

Both 2D and 3D velocities are calculated as shown in Figure 4-8. The 2D velocity is based on the distance of particle displacement projected on the sample surface. Based on the structure of the stereo adapter shown in Figure 4-2, the coordinate values in the image Euclidean coordinate system for the left and right side views should be identical if and only if the object appears on the centre line of the stereo adapter. However, particle movement does not follow such a line but moves on a 3D curved surface, which means the viewing angle for left and right views are not only different but also asymmetric. The relationship between image pixel and real distance in a 2D system are shown in Table 4-1. The 2D velocity is computed from the 2D image Euclidean coordinate system for left and right side views, however there is a difference between the 2D velocity values from left and right views, and both of them ignore the third component which is normal to the sample surface.

A schematic figure is shown in Figure 4-9 in order to explain the relationship between 2D and 3D velocity. When a particle is moving on the weld pool surface, the 2D velocity is projected onto the surface as horizontal components from the 3D velocity; since the viewing angle is asymmetric these two components are not identical. Based on the 2D and 3D velocities shown in Figure 4-8, the angle between the velocity components can be evaluated by dividing the 2D velocity by the 3D velocity. These are presented in Figure 4-9 as angles α and β . It should be noted that the two 2D components are not perpendicular to each other. Figure 4-10 shows that when an object A is placed on the central line at a distance d in front of stereo adapter (zone I in Figure 4-2), it is firstly reflected as A' by the outside longer mirror, and then as A'' by the shorter mirror. So A in front of stereo adapter is the same as A'' without the stereo adapter. Since there is a short distance D between the two mirrors, then the geometric relationship between particle and its right side image can be expressed as shown in Figure 4-10, where the two mirrors are parallel to each other and the included angle between the mirror and lens is 45° . It is obvious that ω is less than 45° , and the viewing angle from the lens to A'' is $45^\circ + \omega$, the angle ω is dependent on d and D as

$$\arctg(\omega) = 1 + \frac{2\sqrt{2}D}{d}, \quad (4.13)$$

and this condition is the same for both the left and right views. Thus, both of the viewing angles lie between 45° and 90° . As a result, the 2D velocity components are not exactly perpendicular to each other.

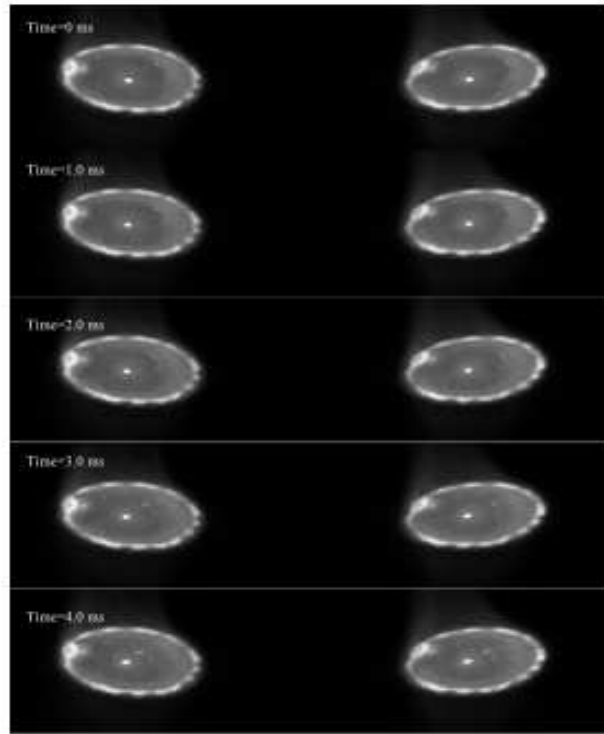


Figure 4-7 Particle flow motion

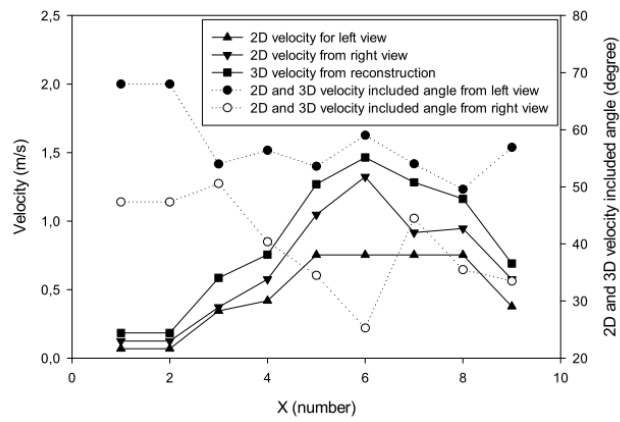


Figure 4-8 2D and 3D velocity based on the images shown in Figure 4-7.

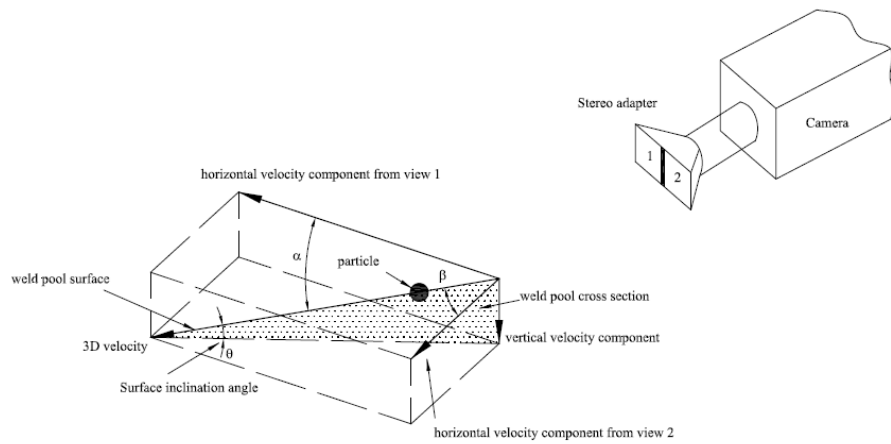


Figure 4-9 Relationship between 2D velocity and 3D velocity.

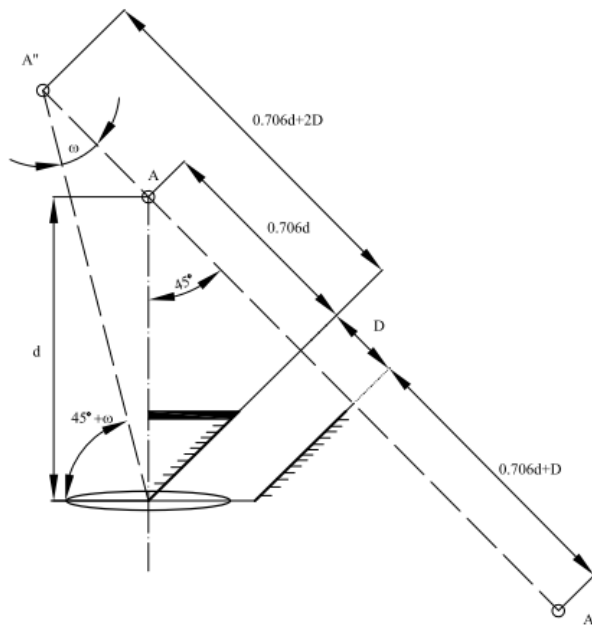


Figure 4-10 The 2D viewing angle.

Table 4-1 2D relationship between pixels and real distances

Left view		Right view	
X (mm/pixel)	Y(mm/pixel)	X (mm/pixel)	Y (mm/pixel)
0.063133	0.013705	0.058532	0.024785

In Figure 4-11, a cross section of the weld pool shows the shape and the surface inclination after solidification. Measured angles are also shown in Figure 4-11. The inward flow center is not stationary during welding, but oscillates around the geometric centre of the weld pool, and the inclination angle of the weld pool surface during welding is variable and larger than the values measured after solidification. Although the solidified weld pool cannot be used to represent the weld pool shape during welding, it still gives a qualitative understanding of the inclination of the weld pool surface.

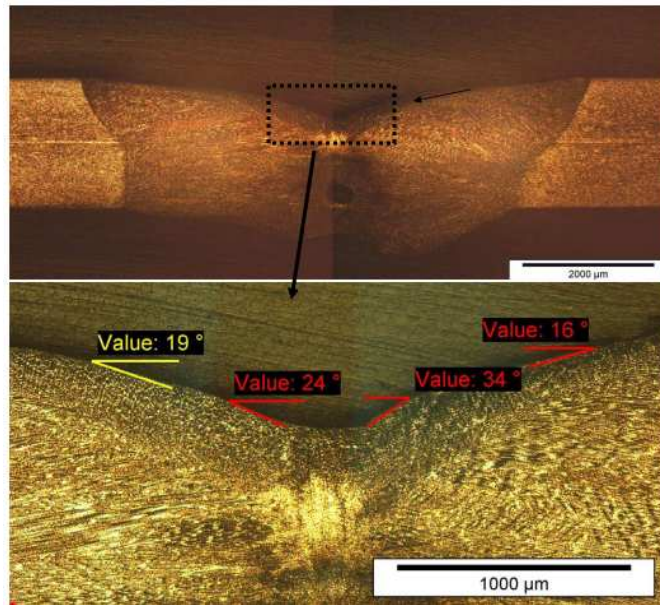


Figure 4-11 Cross section of the weld pool for a laser power of 2000W and a welding duration of 2s. (Top)The small black arrow shows the flow direction. (Bottom) Surface inclination angles in the centre of the weld pool (bottom).

It is important to note that when the weld pool surface is not flat, not only is the flow motion complex, but it can also influence the heat and mass transfer. The inward flow can induce an interfacial phenomenon,^{122,131} which has been shown to be unstable. When the

inclination angle of the weld pool surface increases sufficiently, surface collapse can result in the entrapment of a gas bubble; the result of such a collapse is visible in Figure 4-11. The subsequent pool behavior should therefore be described as a two phase flow, since the flow velocity can be as high as 1 ms^{-1} in such a small channel. Here 3D measurement should provide more reliable information than simple 2D measurement.

4.3.3 Weld pool surface inclination and accuracy analysis

As discussed above, different inclination can lead to differences in accuracy since inclination moves some of the studied points out of the focal plane. For the 3D curved weld pool surface, the induced angle between the camera and particle flow direction is dependent on the camera inclination angle, the surface curvature, and the particle position. As shown in Figure 4-12, θ ($0^\circ < \theta < 90^\circ$) is the weld pool surface inclination angle to horizontal plane, for a flat surface $\theta = 0^\circ$. Theoretically, at the center of weld pool $\theta = 90^\circ$ since the inward flow direction is vertically downward, but in real welding, this might be less than 90° . The camera inclination angle to horizontal plane is γ . To observe the particles on the weld pool surface we must have $\gamma > \theta$ and due to experimental limitations $\gamma < 90^\circ$.

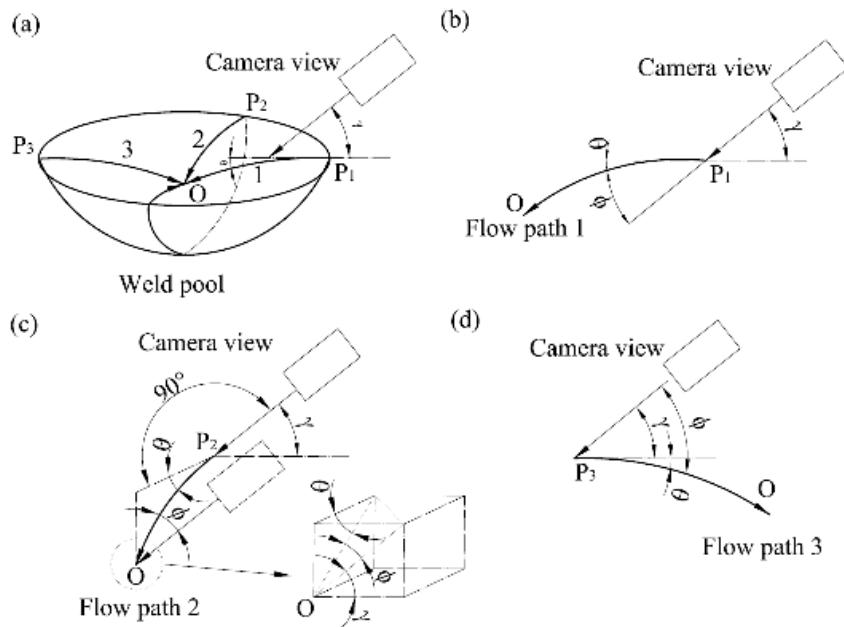


Figure 4-12 Induced angle between camera and inclination of weld pool surface

Figure 4-12b-d shows three different representative positions on the weld pool surface labeled flow path 1, flow path 2 and flow path 3 in Figure 4-12a, which meet at point o , the geometric center of weld pool surface. For the particle following flow path 1 (Figure 4-12b), the induced angle between camera and weld pool is $\phi = \gamma - \theta$; a similar condition applies to flow path 3, where $\phi = \gamma + \theta$; Flow path 2 (Figure 4-12c) lies perpendicular to the camera axis; the angle ϕ between the camera axis and the pool surface is $\phi = \arccos[\sin(\gamma) \cdot \sin(\theta)]$. For the measurements made in this study, $0^\circ < \theta < 35^\circ$ and the camera inclination angle to the work piece surface $\gamma \approx 45^\circ$. Thus the induced angles for flow path 1, 2 and 3 range between $15^\circ < \phi < 45^\circ$, $66^\circ < \phi < 90^\circ$ and $45^\circ < \phi < 75^\circ$ respectively.

The current 3D reconstruction results are based on particles lying on the weld pool surface between the positions of flow paths 2 and 3 (Figure 4-12). This may be illustrated with reference to Figure 4-7, where the movement of the white point on the top-right of the weld pool is followed. Only a very small region of the pool surface has an inclination angle $\theta > 30^\circ$, as measured from the weld pool cross section in Figure 4-11. For the velocity assessment, the particle located between the boundary and approximately 80% of the weld pool radius was chosen, since close to the center of the weld pool, the flow motion is less stable and measurement errors increase. The induced angle θ between the camera and weld pool surface is therefore larger than 45° . As already noted in the calibration error analysis section, calibration group 1 has a camera to surface inclination of 45° giving rise to a reconstruction error of 11.4%. In the current measured case, the induced angle between particle flow direction and camera lens is larger than 45° . As a result, our current 3D reconstruction has a maximum error somewhat below this limit because of the higher average induce angle. Theoretically, the 3D reconstruction of the weld pool surface is also possible based on the same optical setup; however, this has not been investigated in the present work due to the complexities of the algorithm.

4.4 Summary and conclusion

A 3D reconstruction method was used to study the fluid flow on the weld pool surface by adding a simple stereo adapter to obtain two images on the same frame of a high speed camera. The qualitative flow motion and quantitative flow velocity are observed. The method provides a way to study the liquid metal flow in the weld pool during welding.

This method can provide 3D point coordinates for a weld pool in a world coordinate system, if there are enough recognized points on the weld pool surface. It is then possible to obtain 3D surface profile measurements and flow velocity measurements for a weld pool under favorable circumstances. In well shielded welding conditions, the surface remains quite clean, without any oxide particles, adding an additional structured illumination laser, as used by Song and Zhang^{35,36} could offer an efficient way to reconstruct the weld pool surface and to track surface oscillations on both arc and laser generated weld pools. It is also possible to use this method when the object shape is a

complex 3D component; however, the equipment arrangement is inherently more complex.

Calibration is the main factor influencing the measurement precision during 3D reconstruction. There are a number of potential sources of error including the roughness of the calibration board, spatial resolution of a printed calibration checkerboard or limited image resolution from the camera. The first is not thought to be significant in the present case as the board is flat to within a few microns. The spatial resolution of the checkerboard relates to the accuracy of printing and hence the accuracy to which the intersection points can be identified. Graininess in the image is illustrated in an enlarged section of the checker board shown in Figure 4-13. For our purposes, a printing precision of 50 micron was employed. Thus, the main error source is the spatial resolution of printed calibration checkerboard since the square boundary is not sharp enough to distinguish the exact corner positions that were used for calibration. As to the image resolution, it is limited by the camera speed, improving the camera speed can provide a better temporal resolution, however this is generally accompanied by a lower image resolution.

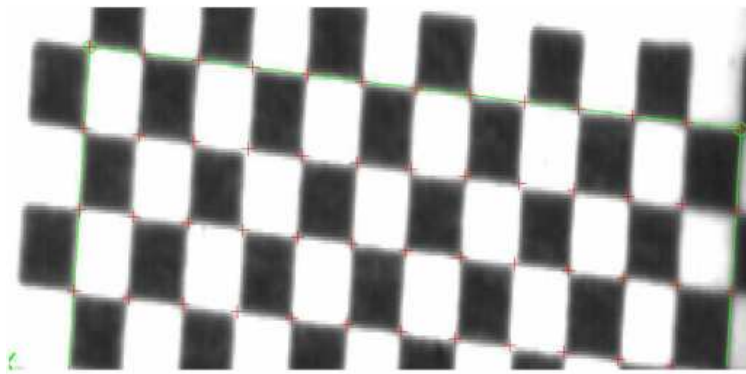


Figure 4-13. Enlarged calibration checkerboards.

5 Oxygen active and transitional flow

5.1 Introduction

Fluid flow plays an important role in energy transfer during welding, and surface tension is reported to be the main driving force.^{1,20} Surface tension can be significantly influenced by the addition of surface active elements^{11,107} and the degree of surface cleanliness.¹³² Results from both experimental investigations^{11,107,110,133-137} and numerical simulations^{103,116-118,138-140} have shown that surface active elements have a strong influence on Marangoni driven fluid flow, particularly during arc welding. Surface tension driven flow is influenced both by the presence of surface active elements and by local temperature variations, and has been quantified by Sahoo *et al.*⁸⁰ for the oxygen-iron system.

Due to its unavoidable presence in the atmosphere, the oxygen influence^{111,112} on welding is considerable. In this chapter, a novel transition in flow direction during laser spot welding is reported related to the environmental oxygen concentration and laser exposure time. The temporal development of both the oxygen concentration and the surface temperature and their influence on fluid flow have therefore been studied.

5.2 Experimental arrangement

5.2.1 Experimental system

The laser spot heating system employed to make spot welds is shown schematically in Figure 5-1. Spot welds were made with a defocused Nd:YAG laser (wavelength 1.064 micron) in the conduction mode to avoid significant vaporization, which could otherwise lead to surface displacement or keyhole formation. The development of the weld pool was observed with a high speed camera (Phantom V.5) operating at a speed of 10,000 fps. The sample was placed in an environmentally controlled chamber, with argon, argon+oxygen or air flushed slowly through the system to control the oxygen level in the range 30 ppm to 20.9%. Twelve different oxygen concentrations were examined as listed in Table 5-1.

5.2.2 EPMA oxygen concentration measurement

The composition of the main alloying elements (Cr, Fe and Ni) and the distribution of oxygen and sulphur were determined using Electron Probe Microanalysis (EPMA). Oxide measurements were performed with a JEOL JXA 8900R microprobe employing wavelength dispersive spectrometry (WDS). The instrument was calibrated with elemental standards of Cr, Fe and Ni (Astimex Metal Mount 44) and quartz (SiO₂ – Astimex Mineral

Mount 53) with a purity of 99.95 wt.% or better. Mineral marcasite (FeS_2 – Astimex Mineral Mount 53) with purity of 99.95% was used as a calibrant for sulphur.

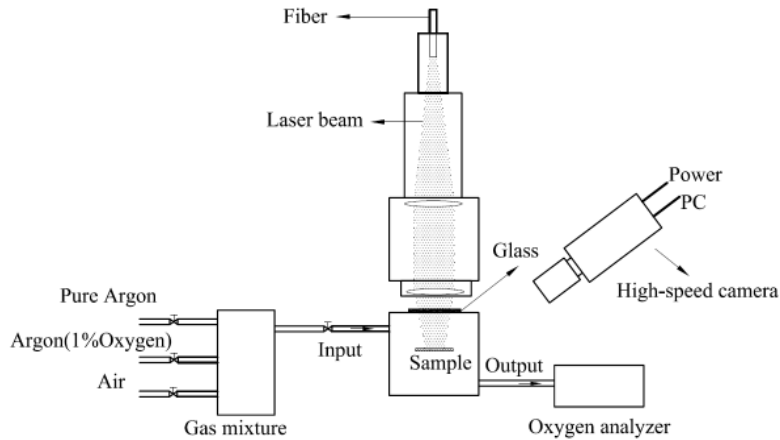


Figure 5-1 Experimental arrangement.

Table 5-1. Experimental cases examined using a constant laser power (2808 W), defocused laser spot size (12.6 mm diameter) and illumination time of 1 s.

Case number	1	2	3	4	5	6
Oxygen concentration (ppm)	59	188	403	805	1025	2396
Time to start melting (s)	0.1441	0.1446	0.1519	0.1387	0.1384	0.1351
Time to start inward flow (s)	-	-	-	-	-	-
Case number	7	8	9	10	11	12
Oxygen concentration (%)	0.4768	1.0	3.1	8.7	14.5	20.9
Time to start melting (s)	0.1171	0.1095	0.0668	0.0619	0.0306	0.0266
Time to start inward flow (s)	-	-	0.2980	0.2640	0.2452	0.2528

Surface oxide scale measurements were made using an electron beam with an energy of 15 keV and beam current of 50 nA. The electron beam was defocused to a circular area of 100 μm diameter. The composition of the main alloying elements and measurement of oxygen level was performed on weld cross-sections using the same beam parameters and a 10 μm spot diameter. In addition, a trace element measurement scheme was employed for oxygen and sulphur, using a beam energy of 15 keV, a beam current of 500 nA and a 10 μm spot diameter; in this case only oxygen and sulphur X-ray intensities were recorded.

The composition at each analysis location of the sample was determined using the X-ray intensities of the constituent elements after background correction relative to the corresponding intensities of reference materials. The intensity ratios were processed with a matrix correction program CITZAF.¹⁴¹ The contents of the trace elements O and S were determined from the X-ray intensities keeping the composition of the matrix fixed at 72.7 wt.% Fe, 18.8 wt.% Cr and 8.5 wt.% Ni, derived from bulk measurements and normalized to 100 wt.%. The points of analysis were located along lines on the weld pool surface and the cross sections depicted in Figure 5-2. The energy of the spectral lines, detection limits and counting errors are given in Table 5-2.

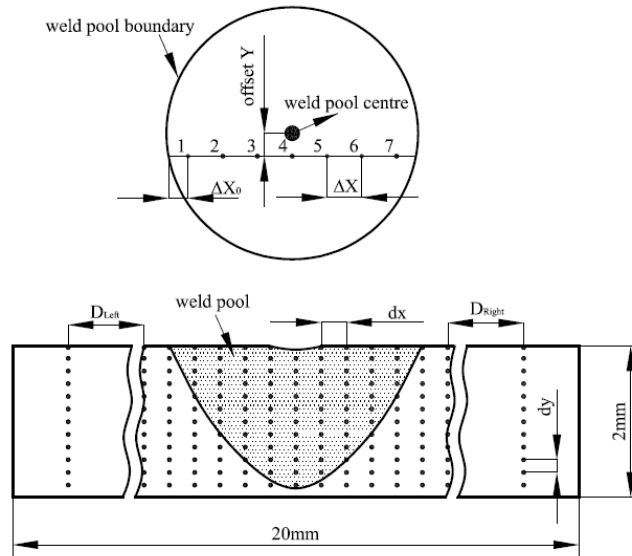


Figure 5-2 Oxygen measurement locations: (a) surface oxygen measurements in steps ΔX of 1000 to 1200 μm ; an offset Y of 500 to 1000 μm from the pool centre was used to avoid errors due to measurement in the region of significant weld pool curvature, (b) cross-sectional measurements perpendicular to the original material surface made in increments dy of 50 μm , along lines 500 μm apart (dx) and extending 1000 μm to 1500 μm into the base material. Two additional lines were measured far from the solidified pool locations for comparison ($D_{\text{Left}} \approx D_{\text{Right}} \approx 2\text{mm}$).

Table 5-2. The energy (keV), detection limit (ppm) and counting error (wt.%) is given for each of the elements analysed using WDS.

Element, X-ray line	Energy (keV)	Detection Limit (ppm)	Counting error(wt.%)
Oxygen, O K α	0.529	20	26 ppm
Sulphur, S K α	2.307	8	6 ppm

5.3 Results

5.3.1 Observed flow behaviour

Marangoni driven flow generally leads to one of two distinct flow patterns when welding; an outward flow, from the centre to the edge of the molten pool, or an inward flow from the edge to the centre,^{1,130,136} dependent on whether the surface tension gradient is negative or positive respectively. In the current laser spot welding configuration, the development of the weld pool was observed and the flow motion was measured by visualizing the displacement of surface oxide particles. During the evolution of the weld pool, the surface tension is affected both by the transport of oxygen from the environment to the pool as well as the surface temperature distribution. As time progresses, more and more oxygen is absorbed by the liquid pool, and the dissolved oxygen concentration in the liquid pool increases, changing the surface tension gradient. The surface temperature and temperature gradients change as energy is absorbed by the work-piece. The detailed behaviour is dependent on the evolution of the local absorption coefficient, as well as the heat and mass transfer in the weld pool. These coupled factors result in observed flow behaviour that can be quite complex and unsteady. Snapshots of weld pool evolution for a spot weld made in a high oxygen environment (case 12 with 20.9% oxygen) are shown in Figure 5-3, illustrating changes in flow behaviour. During initial weld pool formation, the surface flow of the liquid metal is outward (see Figure 5-3a). As time progresses, oxygen is absorbed by the liquid pool, the outward flow becomes steadily weaker as the surface tension gradient approaches zero. Above some critical combination of oxygen concentration and surface temperature distribution, the surface tension gradient becomes positive and the flow direction changes (see Figure 5-3b). The resultant inward flow gives rise to the accumulation of surface oxide particles in the region of flow convergence, which need not be in the centre of the pool. High speed video images indicate that the converging flow can rotate around the geometric centre of the weld pool.

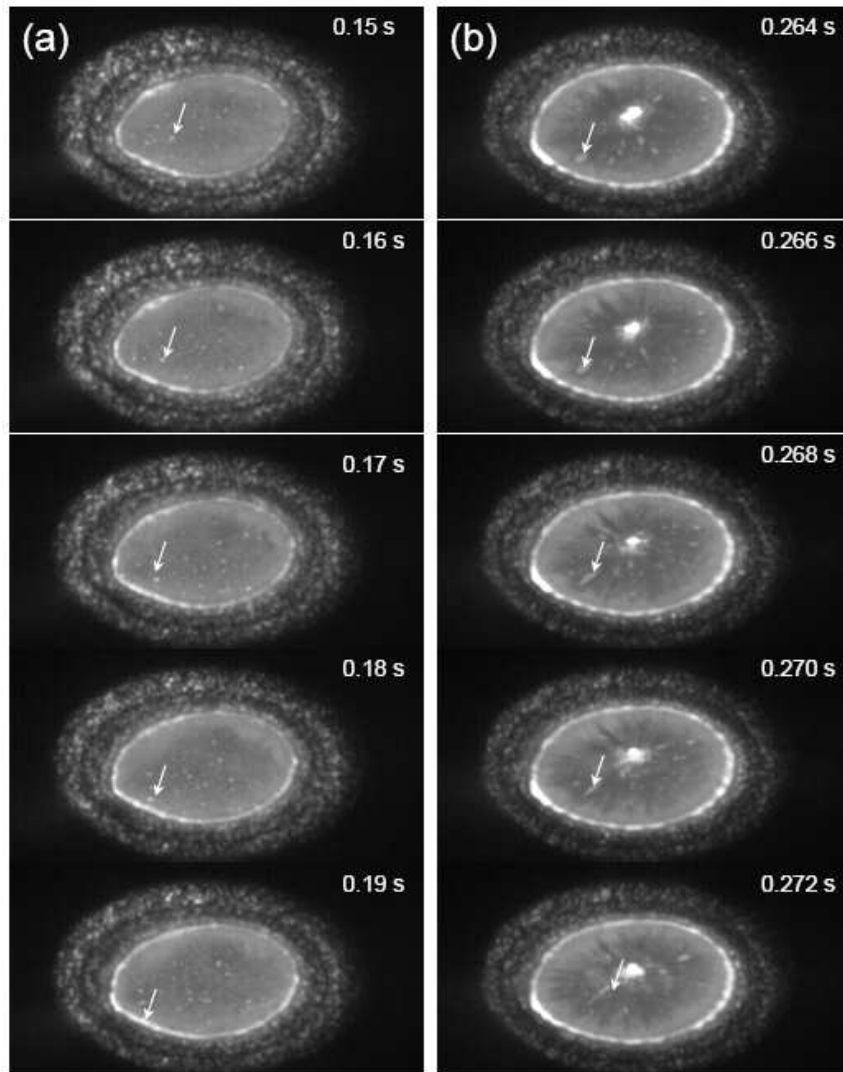


Figure 5-3. Flow motion and oxide particle movement for a laser spot weld made in air shielding, (a) outward flow (b) inward flow to a point.

5.3.2 Interface instability

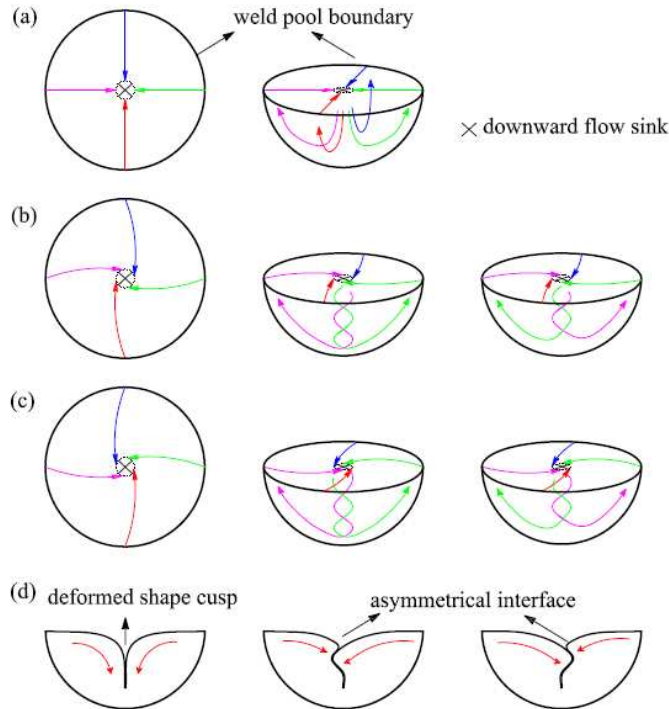


Figure 5-4. Illustration of inward flow patterns, the centre and right hand sketches show possible flow patterns for small volume elements of the fluid, (a) ideal inward flow (b) clockwise inward flow (c) counter clockwise flow.

The interfacial phenomena was addressed by Zacharia and co-workers,¹²² who studied inward flow by numerical simulation and found that interfacial phenomena have a significant influence on the development of the weld pool. Asymmetrical melting patterns were studied by Mishra and co-workers,¹⁴² who reported that asymmetric flow can result in asymmetry in weld pool shapes when welding materials with different sulphur concentrations. In chapter 3, the instability of the flow convergence interface in non-stationary arc welding is studied,^{130,136} where the inward flow forms an unstable interfacial line and induces vortices at the rear of the weld pool. In the current stationary laser spot welding configuration, the interface flow can generally be described as a rotational flow.

Three kinds of flow regimes are illustrated in Figure 5-4. In an ideal condition, often employed to model weld pool fluid flow Figure 5-4a, the liquid metal flows from the boundary to the centre of the weld pool and downward to the bottom of the pool (inward toroidal flow). In practice, strong rotational flow is observed, as illustrated schematically in Figure 5-4b and Figure 5-4c. These can be clockwise or counter clockwise, dependent upon the surface temperature and surface active element distribution. For both conditions, two possibilities exist; the first is a cellular flow, in which a liquid volume element can return to the same side of the weld pool (middle images, Figure 5-4b and Figure 5-4c); the second is cross-cellular flow, where a liquid volume element crosses the central line and moves to the opposite side of the weld pool (right hand images, Figure 5-4b and Figure 5-4c). Which dominates is still not known with certainty; however, the latter is likely based on the random flow behaviour observed by Weidlich *et al.*,¹⁴³ who used an X-ray source to track tungsten carbide and platinum particle displacements inside a weld pool.

The rotational flows observed in the present work show strongly asymmetric patterns. As illustrated in Figure 5-4d, the inward core can oscillate around the geometrical center of the weld pool. This might be the result of surface tension perturbations, due for example to chemical inhomogeneity, or an uneven temperature distribution due to lack of uniformity in the laser power density distribution (see Figure 5-5) on the workpiece surface. Temperature variations may also arise as a result of oxide particle formation, which affects energy absorption from the laser beam. All these factors will lead to local variations of the surface tension, which can result in asymmetrical flow.

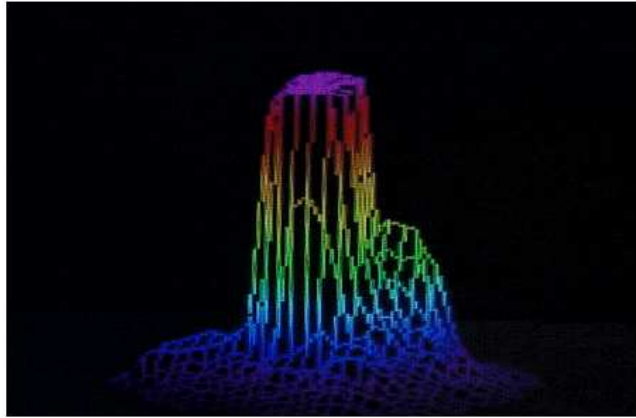


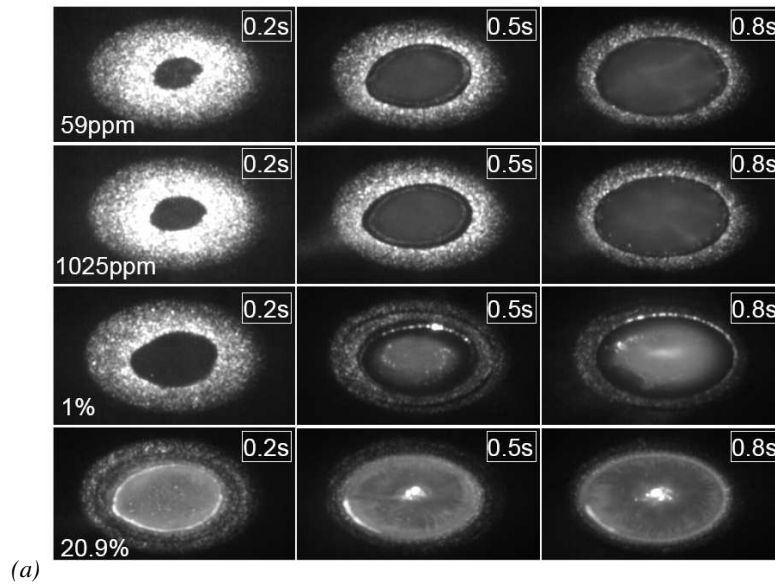
Figure 5-5. Laser power distribution.¹⁴⁴

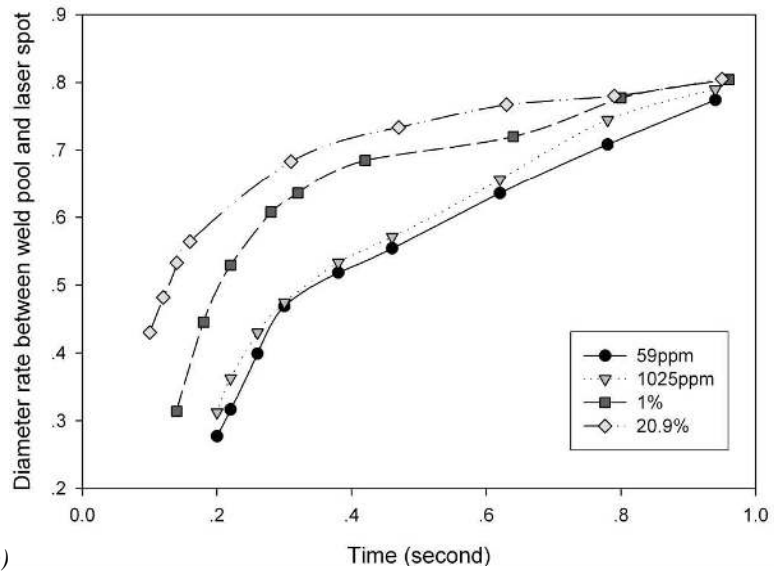
Despite observing asymmetrical flows in laser spot welds, the weld pools are substantially symmetrical, unlike the cases reported when welding dissimilar materials.¹⁴² This may be due to the random and short lived nature of the asymmetries with respect to the lifetime of the weld pool, resulting in an averaging of the flow and energy transport.

5.3.3 Oxygen influences

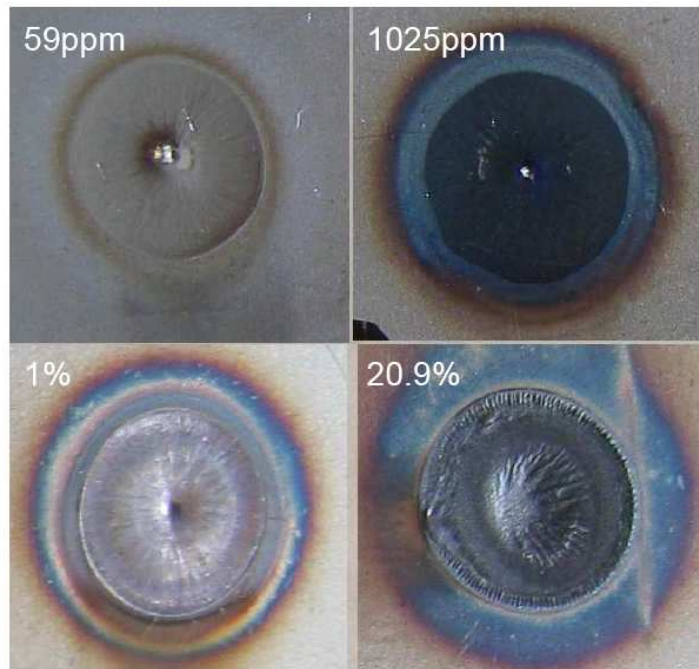
High speed video observations show that the time between initial beam impingement on the sample surface and the onset of weld pool formation decreases with increasing oxygen content (Table 5-1.). This may be attributed to a variation of the surface absorptivity coefficient with increasing oxygen concentration in the environment, resulting in a greater total power absorption. As a result, the weld pool size increases with increasing oxygen concentration for a constant illumination time (Figure 5-6a). After the onset of melting, the liquid pool diameter increases with time. In the initial stages of development, the weld pool size varies for a given elapsed time, although the final sizes are similar (Figure 5-6b).

As expected, the degree of oxidation on the weld pool surface is highly dependent on the oxygen concentration in the shielding gas. For the lowest oxygen concentration (case 1, 59 ppm), the surface is relatively clean, whilst for the highest (case 12, 20.9%), oxide and slag particles float on the weld pool surface (Figure 5-6c). Cross-sections of these welds are shown in Figure 5-6d, indicating that variation of oxygen concentration has little influence on the top bead width but significantly affects the root width and total fusion area. When full penetration is achieved, a second free surface is formed giving rise to more complex flows than those observed with a single free surface.^{144,146}





(b)



(c)

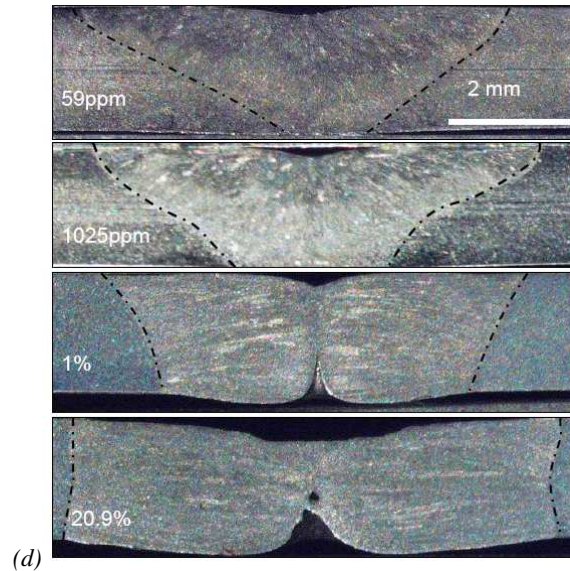


Figure 5-6. Weld pool development and oxygen influence for laser spot welds made at 2808W (a) evolution of the weld pool (b) normalised weld pool diameter as a function of time for different oxygen concentrations (c) final weld pool surface appearances after 1 second (d) cross sections of samples shown in (c).

An important difference observed between outward and inward flow is the surface curvature. For inward flow, the final weld pool surface is strongly curved at the sink point, whereas for outward flow, the surface is only slightly curved. No observable inward flow motion was seen for the lower oxygen environment until the concentration reached 3.1% (case 9), after which, inward flow begins earlier with increasing oxygen concentration (Table 5-1). However, for the weld made in air rather than an oxygen-argon mixture (case 12, 20.9%), strong weld pool surface oscillations were observed, and the time to the onset of inward flow lies between the times measured for 8.7% and 14.5% oxygen concentrations (cases 10 and 11 respectively).

5.3.4 Oxidation and oxygen distribution

Oxygen concentrations on the weld pool surface after solidification have been measured for twelve cases (Table 5-1) and results are shown in Figure 5-7. For oxygen concentrations up to about 1,000 ppm in the shielding gas (cases 1 to 5), the measured surface oxygen concentration is almost constant for different positions on the surface, but increases with increasing oxygen concentration in the shielding environment. From 0.24% O_2 in the shielding gas (case 6), the surface oxygen concentration becomes increasingly position sensitive. In general, the oxygen concentration is higher close to the edges and centre of the weld pool and lower at intermediate locations. Oxygen interacts with a surface both before and after melting occurs, and oxygen is present in the form of oxides

and a solute. Oxygen that remains bound up in oxides has little influence on the surface tension, whilst soluble oxygen is known to have a significant influence.^{134,147} The soluble oxygen levels only change significantly after melting occurs. Both oxides and soluble oxygen contribute to the oxygen concentration measured on the weld pool surface.

In addition to the surface oxygen concentration, the oxygen distribution within the solidified weld pool was measured on planar cross-sections cut through the centre of the weld. Measurements were made on lines normal to the specimen surface, following the scheme shown in Figure 5-2 (bottom). Oxygen distributions were measured for three representative cases; the base metal, 1% O₂ in the shielding gas (case 8) and 20.9% O₂ in the shielding gas (case 12), and results are shown in Figure 5-8.

The oxygen concentration in the base metal is far lower than that measured in the welded samples. Cases 8 is more homogeneous than case 12 (Figure 5-8), where the oxygen concentration along the centre line and at the weld pool boundary is slightly higher than in the intermediate regions, which might be the effect of an inward toroidal flow.

Sulphur is another important surfactant affecting surface tension driven fluid flow in steel weld pools. The sulphur concentration in the base metal sample was therefore measured, yielding an average value is 0.004 wt.%, which is very close to the critical value of 0.003 wt.% for flow reversal reported by Mishra *et al.*¹⁴² In this chapter, the influence of sulphur is limited because (i) initial inward flow at the beginning of weld pool formation was not observed, although there should be a short time of inward flow on the pool surface if the initial sulphur concentration is higher than the critical value and (ii) the initial sulphur concentration will remain constant or decrease slightly with increasing temperature due to vaporization.

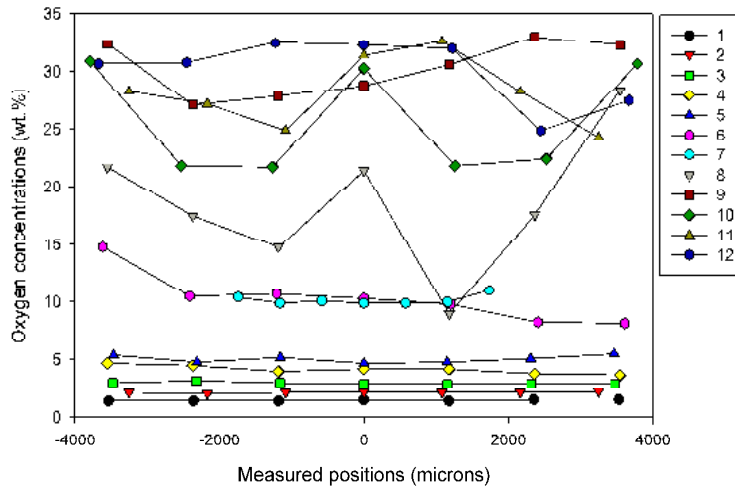
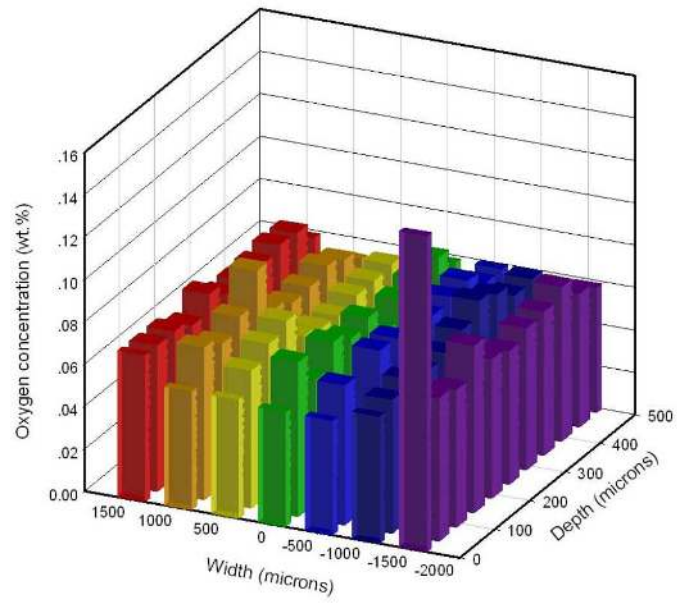
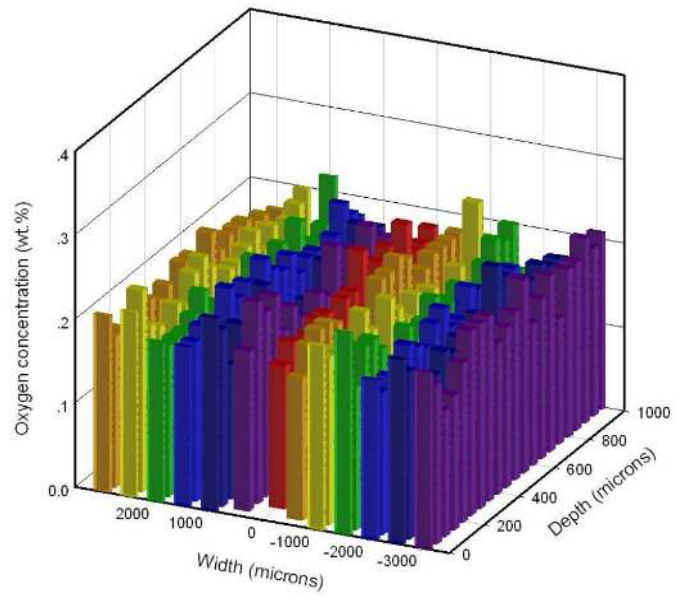


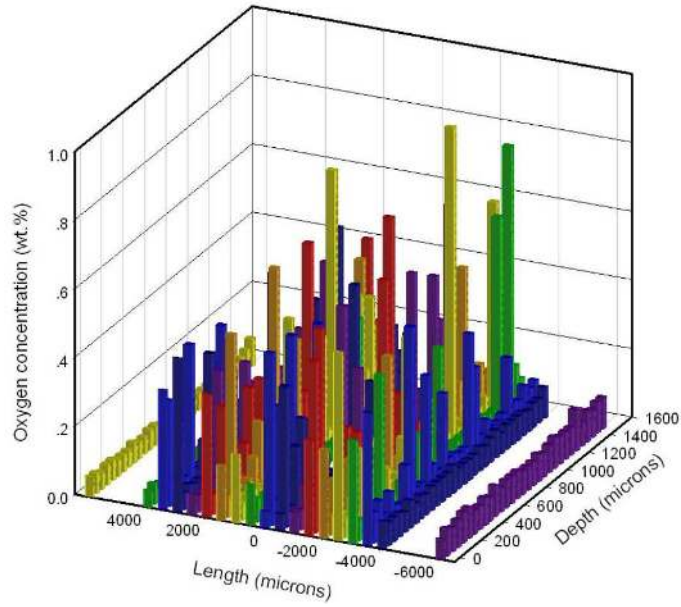
Figure 5-7 Measured oxygen concentrations on the weld pool surface for environmental oxygen levels between 59 ppm and 20.9% (cases 1 to 12 described in Table 5-1).



(a)



(b)



(c)

Figure 5-8. Measured oxygen distribution in sample cross sections: (a) base metal, (b) 1% O_2 in the shielding gas (case 8). (c) 20.9% in the shielding gas (case 12).

The Peclet number expresses the ratio of advection to diffusion and is given by

$$Pe = \frac{Lu}{D}, \quad (5.1)$$

where $L = 0.002$ m is the characteristic length taken as the final penetration depth, and u is the characteristic velocity ranging from 0.1 m s^{-1} to 1 m s^{-1} according to the previous experimental measurements.^{99,130,136} The mass diffusion coefficient D ranges from 4×10^{-11} to $1 \times 10^{-10} \text{ m}^2 \text{ s}^{-1}$ for oxygen in liquid iron at 1873 K.¹⁴⁸ The Peclet number is of the order $10^6 \sim 10^8$, indicating that the flow is mainly influenced by advection rather than diffusion.

5.4 Analysis and discussion

5.4.1 Surface tension and gradient

Both surface active element concentration and temperature can affect the surface tension. This relationship has been described by Belton¹⁵⁰ and was studied by Sahoo *et al.*⁸⁰ for a number of materials. They express the surface tension γ as

$$\gamma = \gamma_m^0 - A(T - T_m) - RT\Gamma_s \ln[1 + Ka_i] \quad (5.2)$$

where $K = k_1 e^{-\left(\frac{\Delta H^0}{RT}\right)}$, $\gamma_m^0 = 1.943 \text{ N m}^{-1}$ is the surface tension of pure metal at the melting temperature T_m , $A = 4.3 \times 10^{-4} \text{ N m}^{-1} \text{ K}^{-1}$ is the negative temperature coefficient of surface tension ($d\gamma/dT$) for pure iron, T is temperature, R is the gas constant, $k_1 = 1.38 \times 10^{-2}$ is a constant which is related to the entropy of segregation, a_i is the activity of species i in solution, $\Delta H^0 = -1.463 \times 10^8 \text{ J Mole}^{-1}$ is the standard heat of adsorption for the iron-oxygen system, and $\Gamma_s = 2.03 \times 10^{-8} \text{ Mole m}^{-2}$ is the surface excess at saturation.

Differentiating with respect to temperature yields the temperature coefficient of surface tension, which is a function of both temperature and oxygen concentration:

$$\frac{\partial \gamma}{\partial T} = -A - R\Gamma_s \ln(1 + Ka_i) - \left(\frac{Ka_i}{1 + Ka_i} \right) \left(\frac{\Gamma_s \Delta H^0}{T} \right) \quad (5.3)$$

The surface tension and its temperature coefficient for the iron-oxygen system over the temperature range 1800 K to 3000 K are shown in Figure 5-9. For pure liquid iron, the surface tension decreases monotonically with increasing temperature. However, for the iron-oxygen system, the surface tension first increases and then decrease with increasing temperature. The maxima occur when the surface tension gradient is zero (the flow transition line in Figure 5-9). On the left lower side of this line in Figure 5-9a, the surface tension gradient is always positive, which corresponds to inward flow motion. On the right upper side of this line, the surface tension gradient is negative, which corresponds to outward flow motion. Changes in temperature or oxygen concentration on the weld pool surface can result in flow reversal if the change results in an excursion across the flow transition line.

5.4.2 Flow motion transition

Here only the flow motion transition during heating is discussed, *i.e.*, the condition $dT/dt > 0$. As shown in Figure 5-9b, there are a number of routes leading to flow reversal, for example, starting from an inward flow and decreasing the oxygen concentration whilst keeping the same temperature (path P_1-P_2), increasing the temperature at a constant oxygen concentration (P_1-P_3) or increasing the oxygen concentration together with the temperature (P_1-P_4). Conversely, a transition from outward flow to inward flow under the condition $dT/dt > 0$ requires an increase in oxygen concentration (for example Q_1-Q_2).

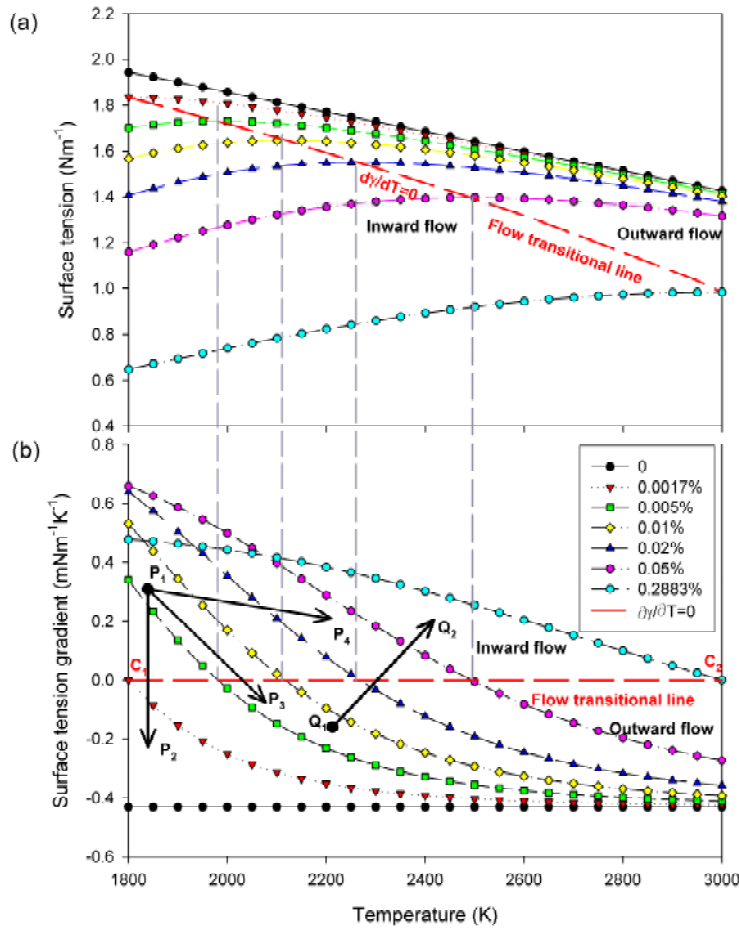


Figure 5-9. (a) Surface tension γ and (b) temperature coefficient of surface tension $\partial\gamma/\partial T$ as a function of temperature and oxygen in the Fe-O system.

There are two critical conditions associated with the temperature range of interest (1800 K to 3000 K). For oxygen concentrations lower than 0.0017%, the surface tension gradient is always negative within the whole temperature range. Conversely, for the oxygen concentration higher than 0.2883%, the surface tension gradient is always positive within the temperature range (see Figure 5-9b). Thus, flow transition is possible only if the oxygen concentration lies between 0.0017% and 0.2883%. This is similar to the condition reported for the iron-sulphur system, where the two critical concentrations are 0.003% and 0.3% respectively.¹⁵⁰

Numerical simulation of the transition from the outward to inward flow observed in practice requires knowledge of the time dependent variation of both $T(t)$ and $a(t)$. Oxygen concentration $a(t)$ is affected by temperature $T(t)$, and temperature $T(t)$ is dependent on the time dependent energy absorption from the laser beam. Both $a(t)$ and $T(t)$ together change the surface tension and affect the fluid flow, resulting in changes in heat and mass transfer.

5.4.3 Influence of temperature and oxygen concentration

Since both the development of temperature $T(t)$ and oxygen concentration $a(t)$ can affect the surface tension gradient, it is necessary to describe these effects independently. The surface tension gradient $f(T, a) = \partial\gamma/\partial T$ is a function of temperature and oxygen concentration. If the variations of temperature and oxygen concentration are denoted dT and da respectively within a very short time step dt , the induced variation of the temperature coefficient of surface tension is $f(T + dT, a + da) - f(T, a)$, then

$$f(T + dT, a + da) - f(T, a) = f'_T(T, a)dT + f'_a(T, a)da, \quad (5.4)$$

which can also be expressed as

$$d\left(\frac{\partial\gamma}{\partial T}\right)_{T,a} = \frac{\partial^2\gamma}{\partial T^2}dT + \frac{\partial^2\gamma}{\partial T\partial a}da. \quad (5.5)$$

The first term on the right hand side represents the contribution from variations of temperature on the temperature coefficient of surface tension, the second term represents the contribution from variation of oxygen concentration. In order to compare the two terms, two dimensionless numbers ψ and χ are defined, the former represents instantaneous contributions within an infinitesimal time dt , the latter the total contribution (integrated from the initial condition). Thus, the instantaneous contribution is given by

$$\psi = \left(\frac{\partial^2 \gamma}{\partial T^2} dT \right) / \left(\frac{\partial^2 \gamma}{\partial T \partial a} da \right), \quad (5.6)$$

and the total contribution

$$\chi = \left(\int \frac{\partial^2 \gamma}{\partial T^2} dT \right) / \left(\int \frac{\partial^2 \gamma}{\partial T \partial a} da \right), \quad (5.7)$$

where from equation 5.3

$$\frac{\partial^2 \gamma}{\partial T \partial a} = -\Gamma_s R \left(\frac{K}{1 + Ka_i} \right) - \left(\frac{\Gamma_s \Delta H^0}{T} \right) \frac{Ka_i}{(1 + Ka_i)^2} \quad (5.8)$$

and

$$\frac{\partial^2 \gamma}{\partial T^2} = -\frac{\Delta H^0}{RT^2} \left(\frac{\Gamma_s \Delta H^0}{T} \right) \frac{Ka_i}{(1 + Ka_i)^2}. \quad (5.9)$$

The latter two terms are shown in Figure 5-10, the contribution from increasing temperature $\partial^2 \gamma / \partial T^2$ is negative, whilst the contribution from increasing oxygen concentration $\partial^2 \gamma / \partial T \partial a$ can be positive or negative.

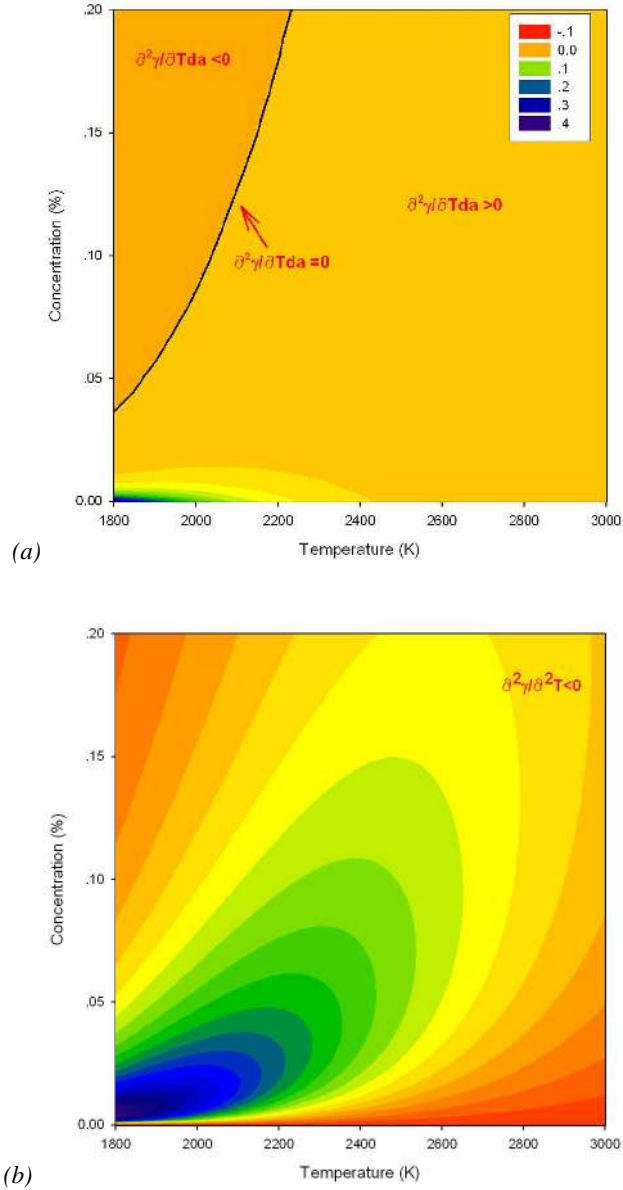


Figure 5-10. Dissolved oxygen concentrations as a function of temperature with (a) $\partial^2\gamma/\partial T\partial a(N m^{-1}K^{-1})$ contours and (b) $\partial^2\gamma/\partial T^2(10^{-6} N m^{-1}K^{-2})$ contours.

5.4.4 Development of temperature and oxygen concentration

Although experimental measurements can provide the oxygen concentration in the initial and final conditions, knowledge of the time dependent intermediate behaviour is lacking. For example, the starting point Q_1 with parameters $t_1, T_1, a_1, \gamma_1, (\partial\gamma/\partial T)_1$, and ending point Q_2 with parameters $t_2, T_2, a_2, \gamma_2, (\partial\gamma/\partial T)_2$, can be connected via any number of paths, leading to different weld pool flow patterns.

To illustrate these effects, consider the example of a starting point Q_1 at a temperature of 1800 K and zero oxygen and an ending point Q_2 at a temperature of 2400 K and an oxygen concentration 0.2% (close to our experimental result shown in Figure 5-8b), under the assumption that $dT/dt > 0$ and $da/dt > 0$. These points are connected by the three paths shown in Figure 5-11. For the purposes of this example, the concentration along each path follows the curves:

$$\begin{aligned} \frac{a - a_1}{a_2 - a_1} &= \left(\frac{T - T_1}{T_2 - T_1} \right) & (\text{path 1}) \\ \frac{a - a_1}{a_2 - a_1} &= \left(\frac{T - T_1}{T_2 - T_1} \right)^n & (\text{path 2}) \\ \frac{a - a_1}{a_2 - a_1} &= \left(\frac{T - T_1}{T_2 - T_1} \right)^{1/n} & (\text{path 3}) \end{aligned} \tag{5.10}$$

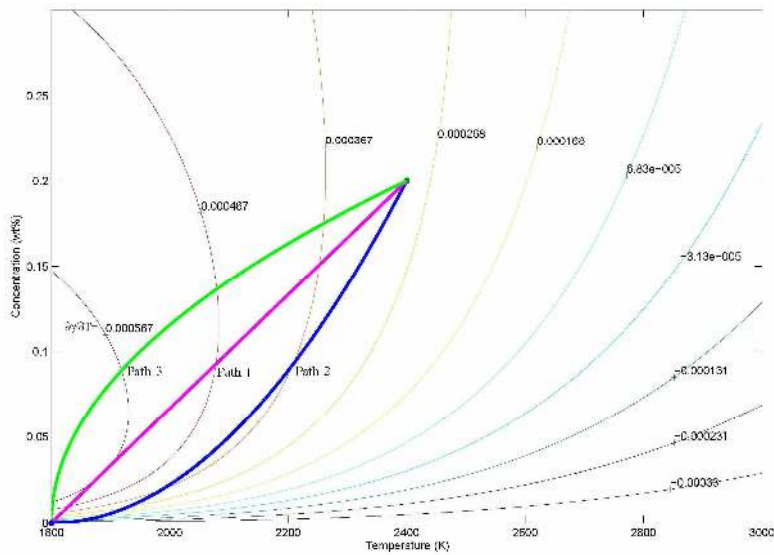


Figure 5-11 Temperature coefficient of surface tension for three example paths.

The surface tension temperature gradient $\partial\gamma/\partial T(T,a)$ is shown in Figure 5-11, for an arbitrarily chosen value of the exponent n of 2. Paths 1 to 3 represent different ways to increase both temperature and oxygen concentration. For path 1, the temperature and oxygen concentration increase linearly. For path 2, the temperature initially increases faster than the oxygen concentration, and subsequently, oxygen concentration increase faster than the temperature. For path 3, the reverse is the case. Although all reach the same final point, the temperature coefficient of surface tension follows a significantly different development (see Figure 5-11), influencing the flow motion as well as the heat and mass transfer.

Using the three paths described in equation 5.10, the total contributions from temperature and oxygen concentration are calculated and shown in Figure 5-12. The solid lines represent the total contribution from temperature variations

$$d(\partial\gamma/\partial T)_T = \int_{T_1}^T \frac{\partial^2\gamma}{\partial T^2} dT, \quad (5.11)$$

whilst the dotted lines represent the contribution from the oxygen contribution variations

$$d(\partial\gamma/\partial T)_a = \int_{T_1}^T \frac{\partial^2\gamma}{\partial T\partial a} da, \quad (5.12)$$

where T ranges from 1800 to 2400 K, and the oxygen concentration depends on the temperature as described in equation 5.10.

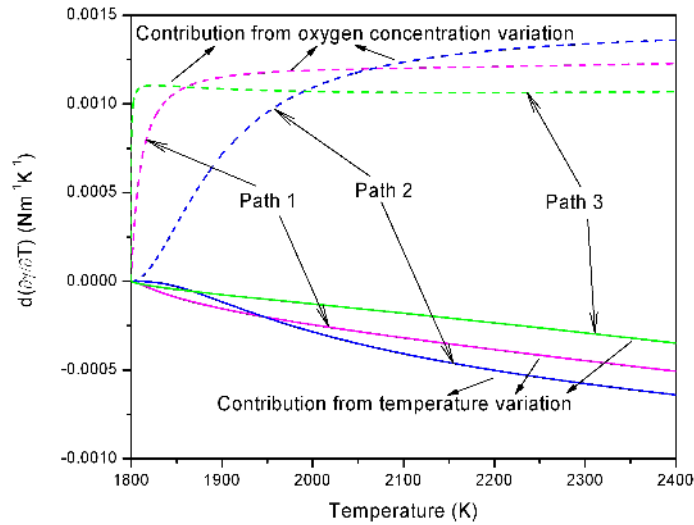


Figure 5-12 Total contributions of temperature and oxygen concentration to $\partial\gamma/\partial T$ for three example paths.

For these three paths, the total contributions from oxygen are positive and larger than the negative contributions from temperature. The total contribution of oxygen on path 3 is initially larger than the other two paths. With increasing temperature, $\partial\gamma/\partial T$ for path 1 exceeds that of path 3, whilst at high temperatures a higher surface tension gradient is observed for path 2.

The dimensionless number χ for these three paths is shown in Figure 5-13a, the main contribution is from increasing oxygen concentration, which has to overcome the negative contribution from increasing temperature.

In order to express the contribution at each small time step, the dimensionless number $1/\psi$ (defined in equation 5.6) is shown in Figure 5-13b. All curves initially start from large and negative numbers because $\partial^2\gamma/\partial T^2$ is almost zero when the temperature is close to 1800 K (Figure 5-10). The dimensionless $1/\psi$ for paths 1 and 2 increases monotonically with temperature. Since $\partial^2\gamma/\partial T\partial a$ can be positive or negative, $1/\psi$ for path 3 first increases then decreases, passing through zero at around 1824 K and 2177 K (Figure 5-13b).

The quantitative contributions for any starting and ending point can be evaluated once the temperature and oxygen component development paths are known. Normally, temperature measurements are difficult to obtain from experiments and recourse is made to numerical simulations. In situ measurement of oxygen concentration is even more difficult and in general, only the final oxygen distribution on the weld pool surface or inside the weld pool can be determined. Further work is required to understand the time dependent oxygen transfer to the weld pool surface. Once the oxygen transfer rate can be evaluated and combined with computation fluid dynamics,¹⁵¹⁻¹⁵³ the flow behaviour and associated heat and mass transfer can be simulated with greater accuracy.

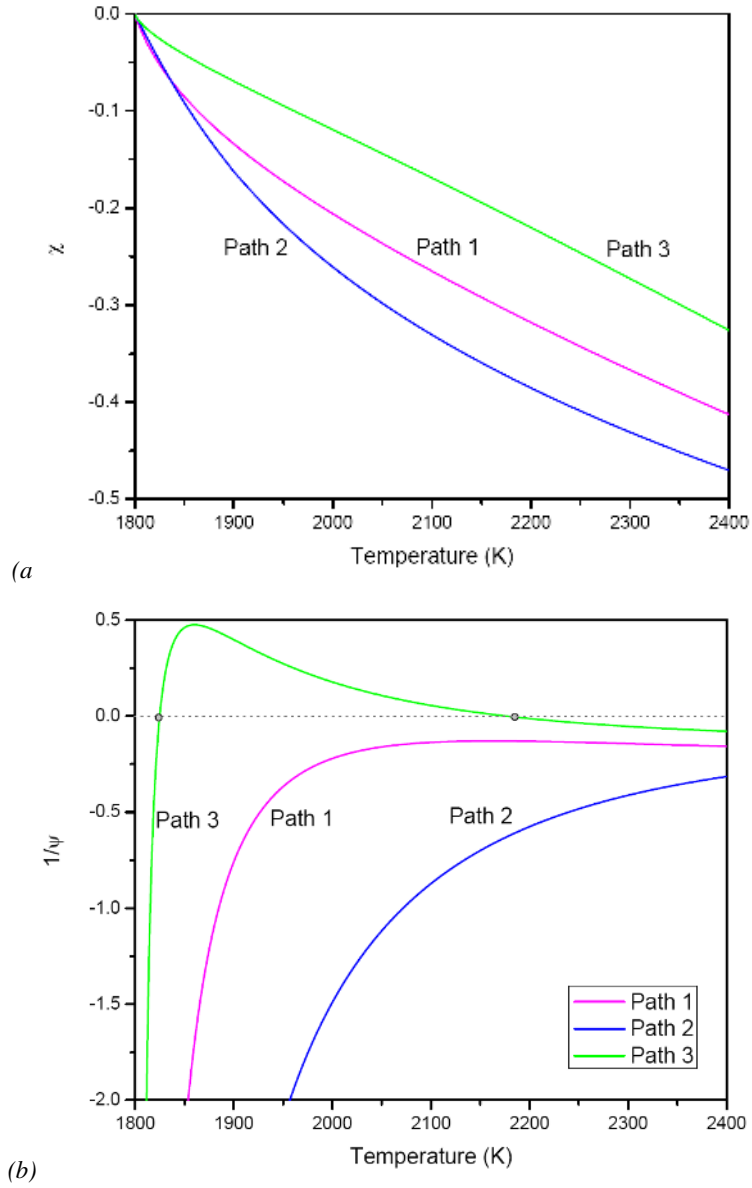


Figure 5-13 Dimensionless numbers for three example paths. (a) z and (b) $1/\psi$.

5.5 Conclusions

In this chapter, a novel transition in fluid flow direction has been reported, which was observed during laser spot welding, where an initially outward flow changes to an inward flow in the presence of an oxidising atmosphere. The behaviour can be explained in terms of changes in surface tension gradients driven by oxygen dissolution in the liquid metal, where oxygen works as a surfactant to induce transitional flow, which in turn results in an unstable rotational interface moving randomly around the pool centre position.

The real time experimental observations indicate that oxidation can change the surface absorption coefficient of solid steel and results in shorter time for the onset of melting. Flow reversal only occurs in the presence of sufficient environmental oxygen; greater than about 0.24% for the material and welding conditions employed here, with an associated weld metal oxygen content of the order 0.18%, which lies within the calculated limits (0.0017% to 0.2883%) within which flow reversal can occur.

The distribution of dissolved oxygen in the weld pool is found to be uniform at low levels of environmental oxygen concentration, but becomes none uniform at environmental concentration levels associated with flow reversal, with greater weld metal oxygen concentrations found at the edges and in the centre of the solidified pools. The upper surface diameters of spot welds show a temporal dependence on environmental oxygen concentration during formation, but the final diameters are independent of environmental composition, being governed by the diameter of the incident laser beam. Conversely, spot root diameters show a strong oxygen dependency and increase with increasing environmental oxygen concentration.

Oxygen is transported into the inside of the weld pool mainly by fluid flow rather than diffusion, and the its distribution is almost homogenous before full penetration occurs. After full penetration, the two free surface flows are unsteady, generating an inhomogeneous distribution of oxygen.

The occurrence of a transition from an outward to an inward flow depends on the relationship between temperature and dissolved oxygen concentration in the weld pool. Although both influence the surface tension gradient, increasing temperature always acts to reduce the surface tension gradient, whilst oxygen acts to increase the surface tension gradient for an outward to inward flow transition.

6 Contact line instability

The weld pool boundary is the contact line between the liquid metal, the solid metal and the vapor (here, the vapor refers to the air, gas, and vaporized metals above the solid or liquid surfaces). The dynamic balance between these states influences the shape of the weld pool. As discussed in chapter 5, temperature and surface-active agents are the two main factors affecting the surface tension of a liquid metal. Together they influence the heat and mass transfer, and thus the dynamic development of the weld pool boundary. Understanding of the spreading of the triple line is helpful for controlling the weld pool shape.

Wetting and spreading in a high temperature environment can be divided into unreactive and reactive conditions, and welding generally falls into the latter category since it involves complex chemical reactions. In this chapter, the dynamic spreading of the weld pool boundary is examined by both optical visualization and chemical analysis. Experiments have been conducted at relatively low power densities compared with those studied in chapter 4 and 5, and boundary spreading and its instability are described quantitatively.

6.1 Spreading and wetting theory

Dynamic wetting^{154,155} or spreading¹⁵⁶⁻¹⁵⁸ appears when a liquid moves over a solid surface and replaces the gas or liquid which was initially in contact with the solid surface. Two general situations are possible; one is partial wetting, where the liquid spreads on the solid surface until the moving liquid front reaches a finite equilibrium contact angle; the other is complete wetting where the liquid displaces the original fluid or gas completely.

Wetting phenomena in low temperature systems have been well documented both by experiments¹⁵⁸⁻¹⁶⁸ and by theoretical models,^{162,165-167,169,170} covering the spatial scale from nanometers to millimetres. Recently, high temperature wetting and spreading have also been studied.¹⁷¹⁻²⁰⁰ Low temperature wetting occurs at $T \ll T_m$ and high temperature wetting at $T > 0.5T_m$, where T_m is the melting point of the substrate.

During welding, the temperature difference appearing on the weld pool surface is significantly larger than gradients observed in other systems; the high temperature leads to chemical reactions, melting and vaporization. All of these conditions make boundary wetting and spreading behavior complex, and limits the execution and interpretation of experimental measurements. For the published studies of high temperature wetting and spreading, most of the reported results are based on constant temperatures. To represent conditions in welding, a laser spot has been defocused on a metal surface to generate a

liquid pool. The spreading and wetting behavior have been studied for a range of oxygen concentrations in the environment. Results from these studies are reported and discussed in this chapter.

Two relationships often employed when describing wetting and spreading phenomena are Young's equation²⁰¹ and Smith's theory.²⁰²

Young's equation

Young first gave a mathematical expression for the equilibrium contact angle, as shown in Figure 6-1a, which represents a macroscopic quantity defined as the angle between the substrate/liquid interface and the tangent to the droplet at the solid/liquid/vapor junction. Equilibrium is described by Young's equation (equation 6.1), which is the result of balancing the horizontal components at the triple line:

$$\cos \theta = \frac{\gamma_{SV} - \gamma_{SL}}{\gamma_{LV}} \tag{6.1}$$

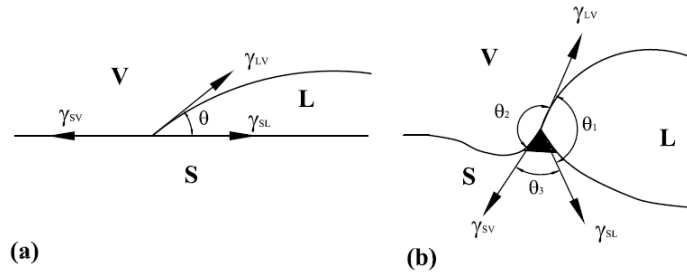


Figure 6-1. Equilibrium between three forces, (a) γ_{LV} , γ_{SV} and γ_{SL} are the equilibrium solid/vapour, solid/liquid interfacial energies, θ is Young's equilibrium angle (b) the force balance at the triple line, θ_1 , θ_2 and θ_3 are equilibrium dihedral angles in the solid liquid and vapour respectively.

Smith's theory

For most high temperature systems, local deformation changes the contact angle at the triple line.^{2,194-198} The forces acting at the triple line resolved both horizontally and vertically (Figure 6-1b), can be expressed as

$$\frac{\gamma_{SV}}{\sin \phi_1} = \frac{\gamma_{SL}}{\sin \phi_2} = \frac{\gamma_{LV}}{\sin \phi_3} \tag{6.2}$$

6.2 Experimental description

The observation system used in this work is the same as that described in chapter 5. A laser was used to continuously heat up a type 304 stainless steel surface and to melt the sample to form a liquid pool. A high-speed camera working at a speed of 10,000 frames per second was employed to record the evolution of the flow pattern as well as the surface morphology development.

After solidification, the sample surface was measured with a confocal microscope (Optical 3D Profiling System, Veeco Wyko NT330) to obtain the surface profile. The microstructure and chemical composition of the surface were examined with a scanning electron microscope (SEM JSM 6500, JEOL) equipped with an energy dispersive spectrometer (EDS). To investigate the microstructure of the oxidized film along the direction perpendicular to the sample surface, a cross section was prepared through the centre of the weld pool, the cross-section was measured using SEM/EDS after polishing to 1 micron.

6.3 Test cases and results

6.3.1 Surface flow motion

In the current test case, the laser power was 2000 W with a spot size of 8 mm. A high-speed camera recorded the dynamic process of melting and spreading. As shown in Figure 6-2, when the sample surface is heated beyond a certain time (around 1 second in this case), the solid surface begins to melt. During the initial pool evolution, a non-circular shape appears as shown in Figure 6-2a-f. Then many small finger-like flows are generated in the radial direction transverse to the molten pool boundary as shown in Figure 6-2g-i. Following this, more and more finger-like flows generate around the rest of the boundary as shown in Figure 6-2m-r.

6.3.2 Marangoni film

From the high-speed video (see Figure 6-2), a circular boundary can be seen ahead of the molten pool. To understand what this is, the sample was examined after solidification for two cases corresponding to laser illumination times of 1.5 and 2 seconds respectively (Figure 6-3 and 6-4 respectively). Dark rings correspond to the expanding circles on the sample surfaces (Figure 6-5), and are identified as thin precursor films spreading ahead of main liquid pool. Three-dimensional surface profiles of these rings are shown in Figure 6-3b and Figure 6-4b. In this work, these precursor films are referred to as Marangoni films. The justification for this terminology is given in section 6.4.1.

Inside this Marangoni film area, there are some finger like profiles lying radially, these correspond to the fingers shown in Figure 6-2. The thickness of the Marangoni film is also measured along four lines as shown in Figure 6-3c and 6-4c using a line scan technique. The measurements show that the thickness of the film is about 3 microns. It should be noted that these thickness and surface profiles are based on post-solidification

measurement; there may be differences between surface profiles during spreading and the results shown in Figures 6-3 and 6-4.

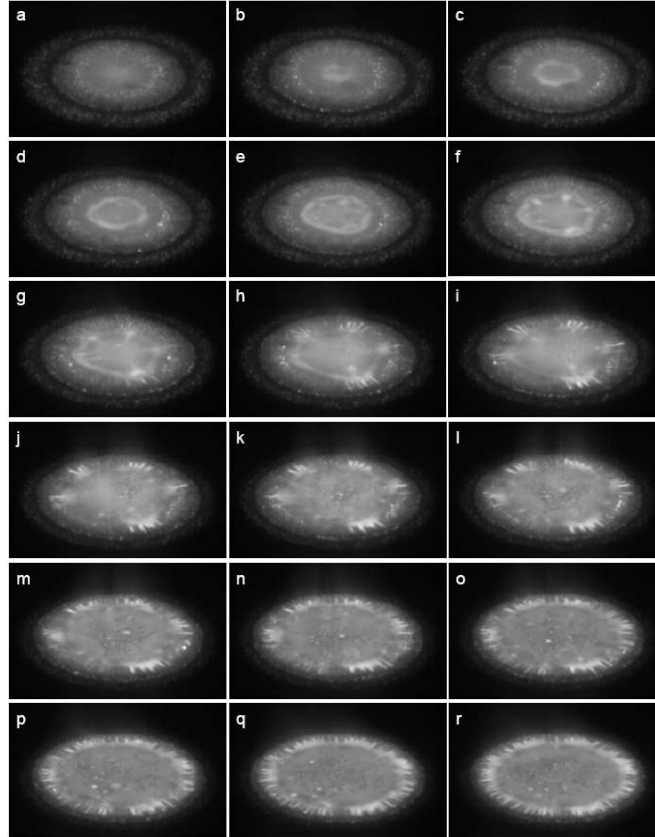


Figure 6-2. Fingering instability development, the time step is 0.05 second (every 500 frames) between successive figures from (a) to (r).

To gain a quantitative understanding of the spreading speed, an image processing method is used to calculate the displacement of the spreading front; the calculated spreading speed is shown as the blue line in Figure 6-6. The spreading speed of the Marangoni film decreases with time; in other words, the spreading speed is lower when the spreading radius is larger. This is most likely due to a decrease of the surface temperature difference with increasing spreading radius close to the boundary of the laser spot. The relationship between spreading radius R and time t can be expressed as

$$R \propto (t - t_0)^n \quad (6.3)$$

where $t_0 \approx 1$ s is the time of melting onset and $n \approx 0.3$.²⁰³

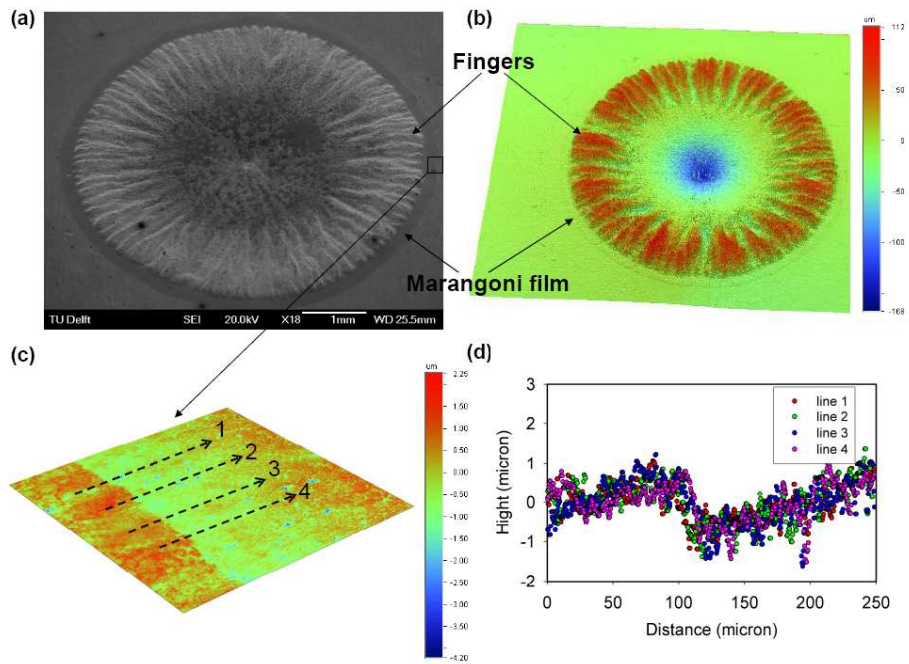


Figure 6-3. Surface profile after solidification for a 2000 W, laser spot weld of 1.5 seconds duration (a) SEM photo (b) 3D surface profile (c) Surface profile of the Marangoni film marked in (a). (d) Surface profiles measured along four lines shown in (c), the step height from Marangoni film to the base metal is less than 3 microns.

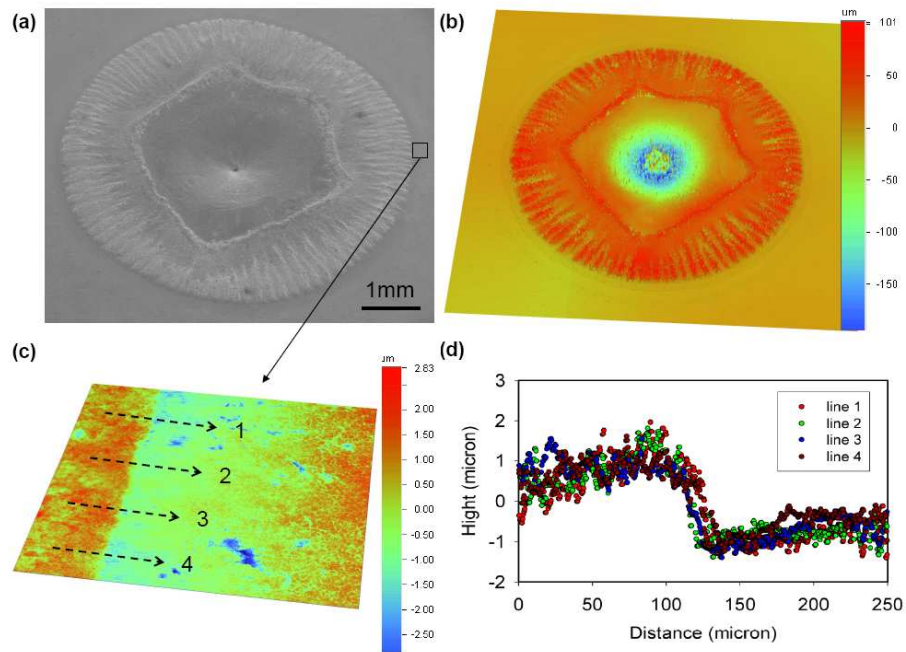


Figure 6-4. Surface profile after solidification for a 2000 W, laser worked 2 seconds duration (a) SEM photo (b) 3D surface profile (c) Surface profile of the Marangoni film marked in (a). (d) Surface profiles measured along four lines shown in (c), the step height from the Marangoni film to base metal is less than 3 microns.

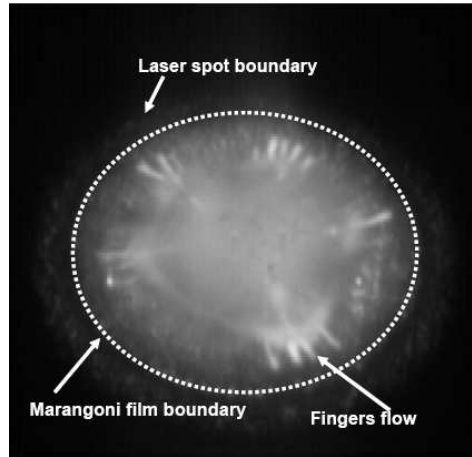


Figure 6-5. Laser spot, Marangoni film, melt pool and spreading fingers.

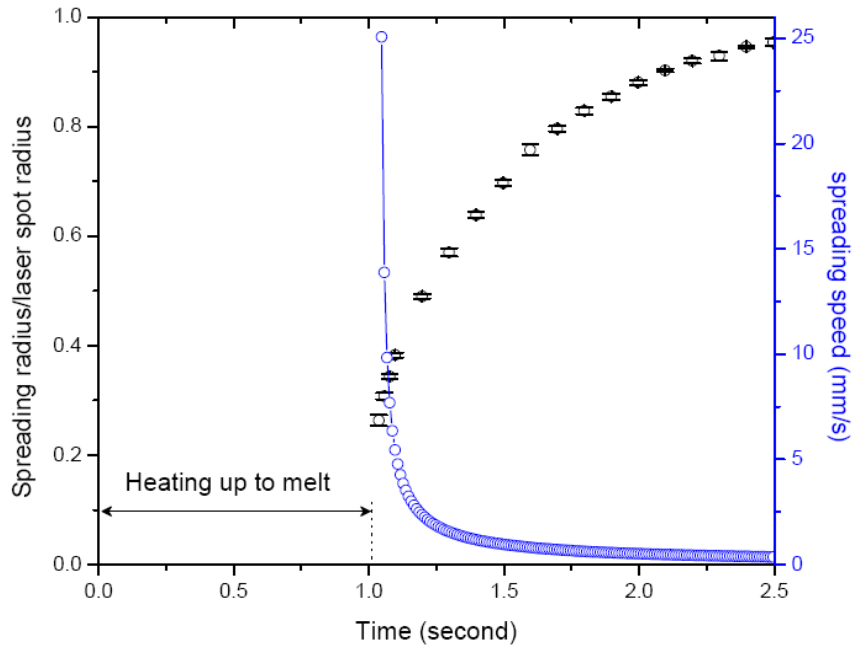


Figure 6-6. Spreading radius and speed of the Marangoni film as a function of time at a laser power of 2000 W.

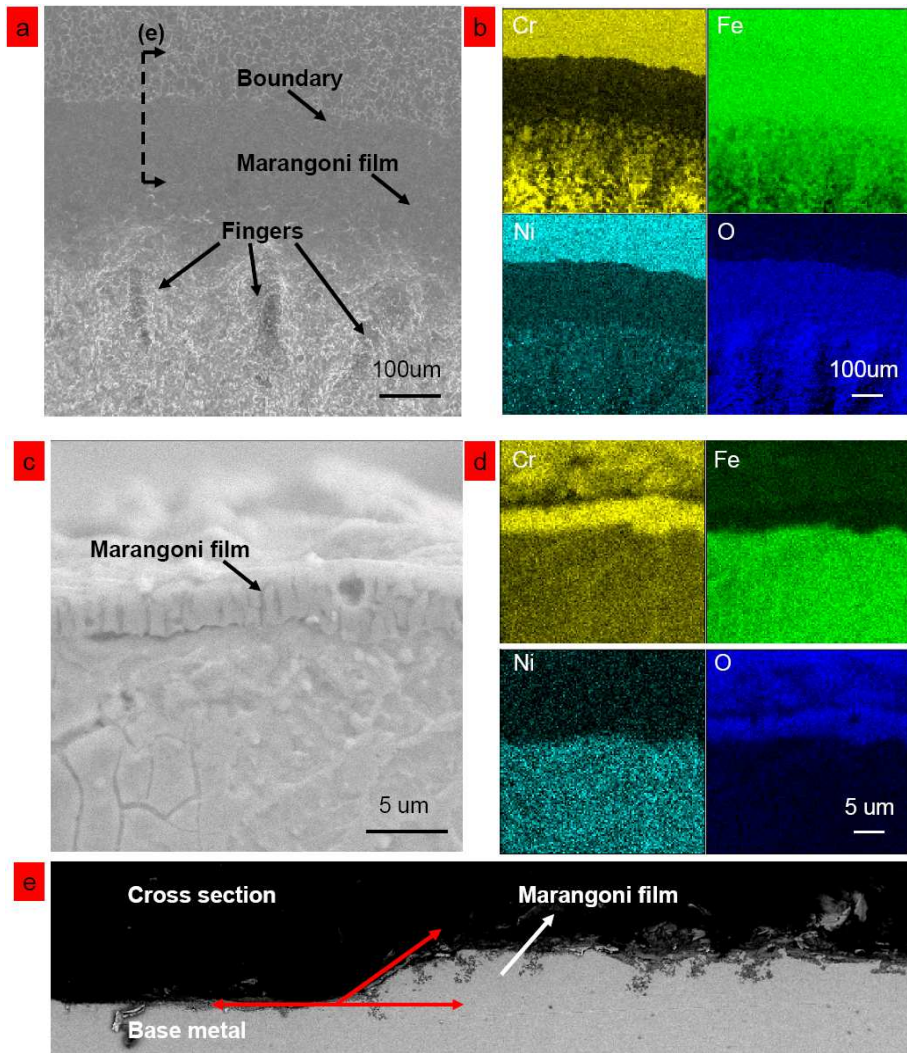


Figure 6-7. (a) Mapping area and (b) elemental maps on the melt pool surface. (c) Mapping area and (d) elemental mapping on a cross-section. (e) Cross section profile of the Marangoni film edge and the base material.

6.3.3 Chemistry mapping

To determine the chemical distribution on the melt pool surface, element maps for Cr , Fe , Ni and O were measured using an SEM-EDS as shown in Figure 6-7. Figure 6-7a covers the base metal, Marangoni film and spreading finger, and Figure 6-7b shows the element maps from the image shown in Figure 6-7a. The cross section was also measured as shown in Figure 6-7c and d, where the scanning area covers both the base metal and the Marangoni film. The contact angle at the spreading front is around 30° as measured in Figure 6-7e. Both Figure 6-7b and d indicate that the oxygen content within the Marangoni film area is much higher than that in the base metal. Thus, the Marangoni film is an oxygen rich film, which spreads on the metal surface. Following this oxide film, the liquid from the molten pool spreads to form the finger flow. Two line scans to measure selected elemental distributions are shown in Figure 6-8. In Figure 6-8a the scanning line passes through the Marangoni film and finger front. In Figure 6-8b the scanning line passes through the Marangoni film and between finger fronts. Two step changes are observed at the spreading interfaces of the Marangoni film and finger flows.

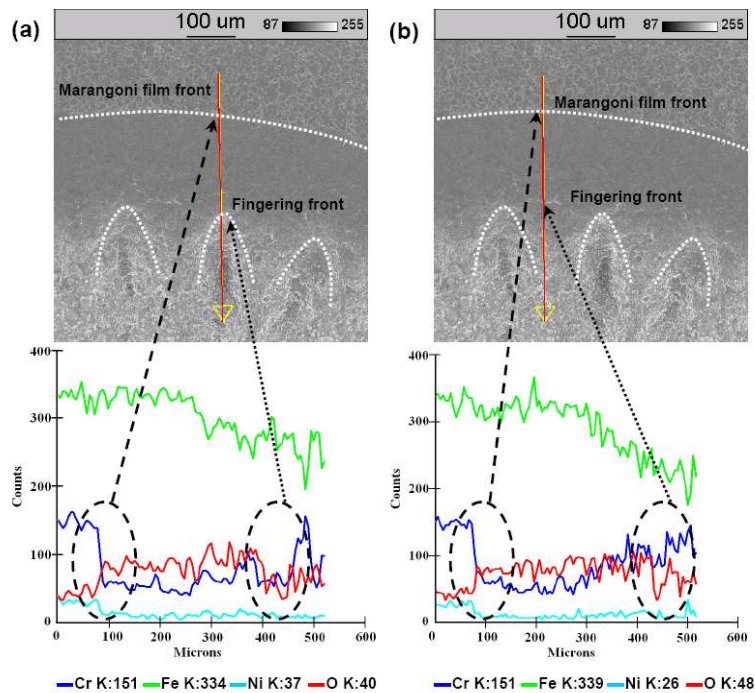


Figure 6-8. Line scanning through (a) fingering front and (b) between fingering fronts.

6.4 Discussion

6.4.1 Thermal grooving and formation of a liquid net

Deformation at grain boundaries (see Figure 6-9) occurs when the sample surface is heated, the theoretical explanation of which was first described by Mullins,²⁰⁴⁻²⁰⁶ who studied the dynamic motion of grain boundaries. It is proposed that the grooves formed as a result of grain boundary deformation influence the wetting of the metal, because they change the contact angles according to Smith's theory (equation 6.2).

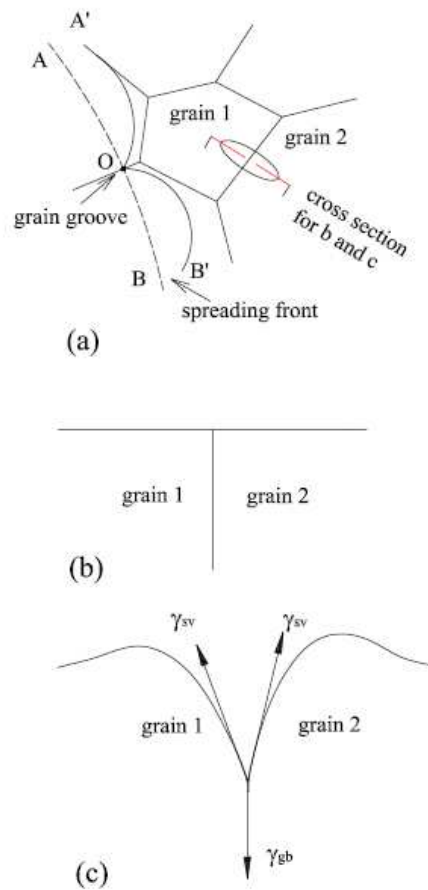


Figure 6-9. The formation of a grain boundary groove (a) surface (b) cross section of grain boundary (c) cross section of boundary groove.

Mullins²⁰⁵ considers only identical surface energies and diffusivities at both sides of the grooves; these conditions are no longer valid if ridge^{1982,194} formation occurs (see shaded area in Figure 6.1b for the formation of a ridge). Asymmetrical surface energies and diffusion along the solid-vapor and solid-liquid interfaces have to be taken into account.²⁰⁰ This was investigated by Saiz *et al.*¹⁹⁴ when they studied the broad effects of wetting ridge formation. They suggest that ridges formed at the triple line in response to the vertical component of surface tension, and drag from these ridges can limit the spreading velocity of the liquid.

In the case shown in Figure 6-10, due to strong deformation of grain boundaries, small islands are formed on the base metal surface before melting, which lead to increase of the surface roughness which has an effect on the liquid wetting and spreading. It can be seen from Figure 6-10 that the spreading flow does not occur as capillary flow in grooves at grain boundaries. However, small flows spread on the grain surface and connect with each other as a liquid net; some deep grooves at the grain boundaries are left as shown in Figure 6-10. The formation of a liquid net may limit the spreading flow since it reduces the contact area between liquid and base metal.

As is known, spreading of a liquid on a solid surface depends upon the relative magnitudes of the surface energies of the vapour-solid surface, vapour-liquid surface and solid-liquid surface. If the the total energy of the system decreases, the liquid will spread resulting in a decrease of the vapour-solid surface area and increase of the other two surface areas. The condition for spreading is thus:²

$$dG = \gamma_{sl}dA_{sl} + \gamma_{sv}dA_{sv} + \gamma_{lv}dA_{lv} < 0 \quad (6.4)$$

This may also be written as:

$$S = -\frac{dG}{dA} = \gamma_{SG} - \gamma_{SL} - \gamma_{LG} \quad (6.5)$$

where S is defined as the spreading parameter or spreading coefficient. When dealing with non-equilibrium situations, such as liquid spreading on a solid surface, S represents the difference between the free energy of the uncovered and the liquid covered regions of the substrate. When S is positive, the solid-gas interface has a higher free energy than the liquid covered region and so the liquid will spontaneously wet the substrate to a final contact angle of zero, a situation known as spreading. Conversely, when S is negative, a non-zero contact angle results and the liquid partially wets the surface.

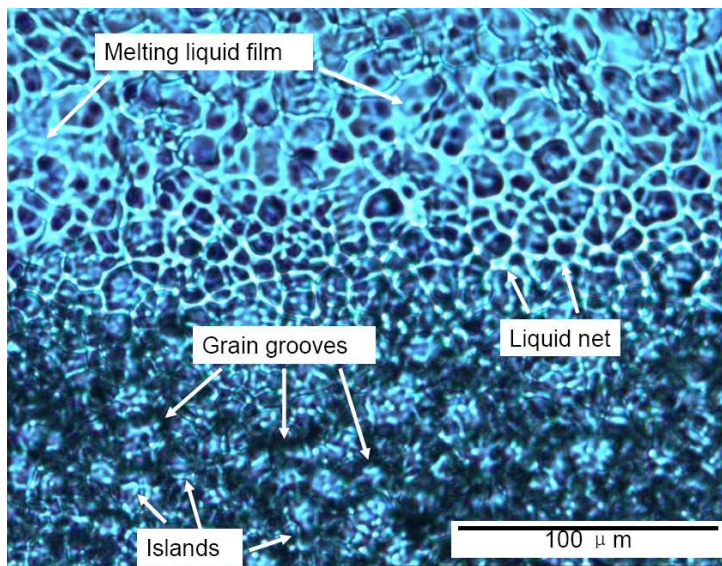


Figure 6-10. The formation of a grain boundary groove and formation of a liquid net.

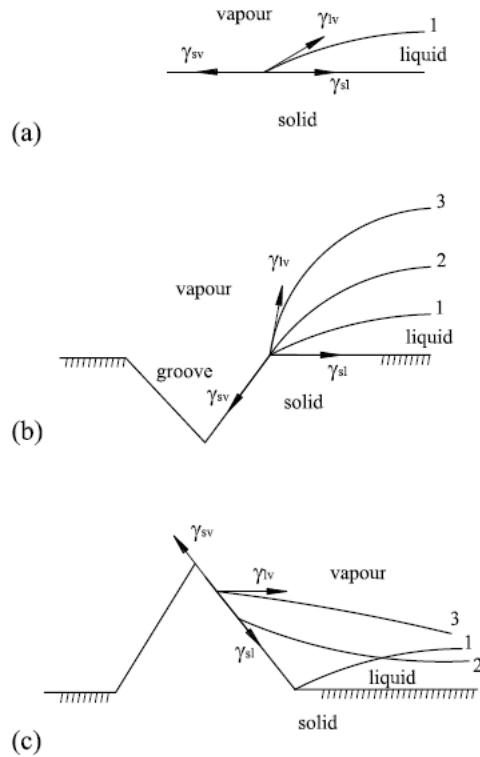


Figure 6-11. Effect of sharp edges on wetting. (a) equilibrium at flat surface (b) liquid front deformation at a sharp edge (c) liquid spreading

According to equation 6.4, to minimize the surface energy of the liquid metal system, spreading may occur to increase the wetted area or pinning to increase the contact angle. To understand how the liquid net shown in Figure 6-10 formed; the surface roughness must be considered. Two cases are considered as shown in Figure 6-11b and c. The first occurs when the spreading front meets a grain groove, the second when the spreading front meets a protrusion. For the purposes of comparison, the variation of interfacial free energy dG is assumed to be the same. The initial equilibrium configuration of the liquid surface is identified in Figure 6-11a. If the liquid volume and the surface energy are increased, the successive configurations of liquid surfaces can be denoted as 2 and 3. For the condition in Figure 6-11b, increasing the contact angle at the edge can make a new equilibrium without spreading; however, spreading is the only way to make a new equilibrium for the condition in Figure 6-11c according to Young's equation, this changes both the contact area and contact angle. Thus, the spreading always occurs at a groove later than at a protrusion. For three-dimensional grooves, some void holes are formed when liquid fronts from all directions are deformed around the groove.

For multi-component crystalline solids, the main determinants of the interfacial energies are the presence of segregants,²⁰⁷ the temperature, and the crystalline orientation. The evaluation of the interfacial energy is difficult because of its sensitivity to the above parameters. Considering the distribution of the temperature field in laser spot welding, isotherms follow more or less concentric circles. Here, the spreading front is assumed to be isothermal. For a condition when a spreading front meets a grain boundary and a flat grain surface as shown in Figure 6-9a, spreading parameters for the grain surface and grain groove are different due to the segregate induced variation of interfacial energy.

The appearance of element enrichment at grain boundaries reduces the melting point and local surface energy at grain boundaries; the spreading parameter for the liquid/grain surface is higher than that of the liquid/groove. Thus, liquid spreads faster on the grain surfaces than in grain grooves and provides the formation of the liquid net shown in Figure 6-10. With increasing heat input, the whole surface is finally covered by liquid. This liquid film solidifies and forms new grain boundaries as shown in Figure 6-12 which is an SEM image on the sample shown in Figure 6-10.

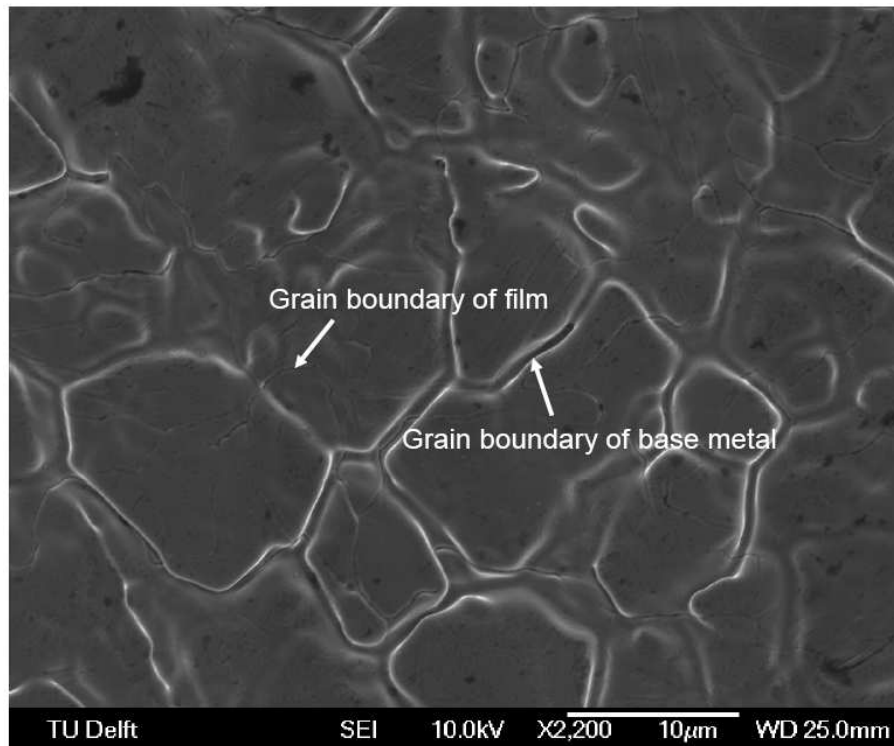


Figure 6-12. Microstructure of solidified surface covered by a film.

6.4.2 Oxygen influence and the formation of a Marangoni film

The surface tension influences the contact angle of the wetting front, and its temperature coefficient reflects the Marangoni flow patterns. Therefore, it is useful to study the oxygen influence on the wettability. By changing the oxygen concentration in the shielding gas (using the same method as that described in chapter 5), five cases were examined as shown in Figure 6-13. For the low oxygen concentration case (Figure 6-13a), the liquid metal forms a net structure during spreading. With increasing oxygen concentration, these flows start to merge with their neighbors (Figure 6-13b-d), and finally form a thin Marangoni film (Figure 6-13e).

To study the oxygen influence on wetting, the temperature at the spreading front is assumed to be the same as the melting temperature. When the oxygen concentration is increased, the surface tension also varies according to equation 5.2. The surface tension gradient due to oxygen variation can be represented by the following equation.

$$\frac{\partial \gamma}{\partial a_i} = -RT\Gamma_s \frac{k_i e^{-\frac{\Delta H^0}{RT}}}{1 + k_i a_i e^{-\frac{\Delta H^0}{RT}}} \quad (6.6)$$

For the values of the various components given in chapter 5, $\partial \gamma / \partial a_i$ is always negative, indicating that surface tension decreases with increasing oxygen content at constant temperature.

According to Young's equation, given a temperature at the triple line, the contact angle of the liquid front will decrease when the surface tension of liquid/vapour decreases and its spreading parameter will be larger. Therefore, the liquid metal with high oxygen concentration has better wettability at the spreading front, and the liquid net becomes increasingly connected as the oxygen concentration is raised. This is supported by results shown in Figure 6-13, where increasing environmental oxygen leads to flow merging and finally forms a thin film.

The dynamic melting process observed from the high speed camera sequences also supports the supposition that oxygen induces the appearance of the Marangoni film. As shown in Figure 6-14, for the case at low oxygen level (the same condition as Figure 6-13a), the boundary of the bulk liquid is almost circular. The Marangoni film only occurs at high oxygen concentration, such as the case shown in Figure 6-13e; however, it is not clear what the critical oxygen concentration is for Marangoni film appearance. Further work is needed to address this question.

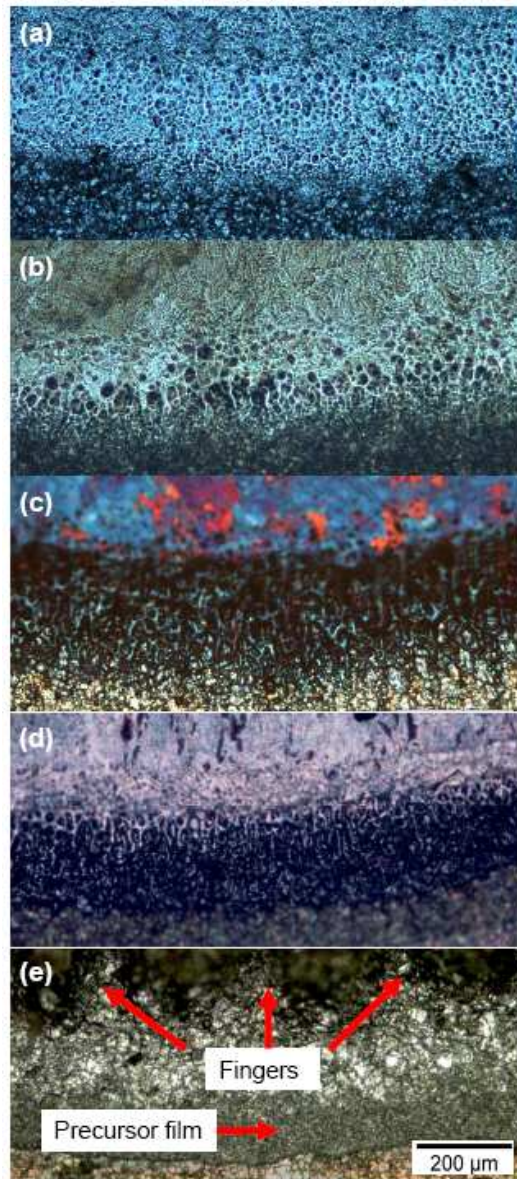


Figure 6-13. Liquid-solid interface profile for different oxygen concentrations in the environment. (a) 50 ppm oxygen. (b) 368.3 ppm oxygen. (c) 968.3 ppm oxygen. (d) 6541 ppm oxygen. (e) 20.9% oxygen.

6.4.3 Potential mechanisms for fingering flow

The fingering instability was first observed by Marmur and Lelah²⁰⁸ when they spread various aqueous surfactant solutions on what they assumed to be dry glass. Their results show that uniform and circular spreading occurs at concentrations below the critical micelle concentration (CMC). Spreading at concentrations above the CMC was accompanied by fingering instability. Troian *et al.*²⁰⁹ showed that instability does not occur on a completely dry substrate, but can be observed both above and below the CMC with a dependence of the pattern wavelength on the initial film thickness. Troian *et al.*²¹⁰ provided the first attempt at modeling the fingering instability of spreading surfactant solutions in order to uncover the underlying mechanism responsible. They suggested that gradients of surfactant concentrations which induce Marangoni stress are the essential driving mechanism for the instability.

Although the precise mechanism for the fingering instability remains unclear, several explanations proposed for low temperature systems are likely to be helpful for uncovering the potential mechanisms active on expanding weld pools. The occurrence of a fingering instability of a liquid front could be induced by an applied force,¹⁶⁵ a surface shear stress,²¹¹⁻²¹⁴ or surfactant solutions.^{163,167,168}

For high temperature weld pools, the most likely source of instability is the surfactant influence. As already commented above, fingering instability only occurs when oxygen concentration is high enough (see Figure 6-13e). Again, for oxygen concentration at a low level as shown in Figure 6-14, the triple line spreads as a circular shape and without formation of a precursor film. The oxygen transportation is a dynamic procedure, which depends on temperature and the partial pressure of oxygen. The fingering instability is only observed when the oxygen concentration in the liquid metal exceeds some critical value (somewhere between 8% and 14% oxygen in the environment for the experimental conditions adopted in this work).

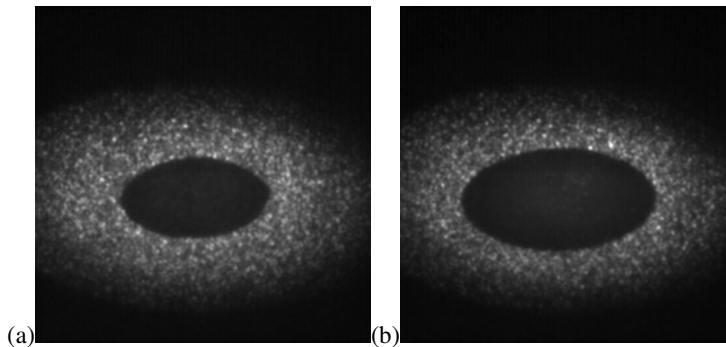


Figure 6-14. Liquid spreading motion at (a) 1.5s and (b) 2s respectively in an argon environment with around 50 ppm oxygen (see sample surface in Figure 6-13a).

In fact, two kinds of Marangoni film can occur; one is on the nano-scale,²¹⁵⁻²¹⁷ which appears when initial melting occurs at grain boundaries, the other one is at the micro-scale,²¹⁸ with thickness of around 3 microns (Figure 6-4). The nano-scale Marangoni film always occurs during heating, however, a micro-scale Marngoni film only occurs when the oxygen concentration is at a relatively high level as shown in Figure 6-13. Thus, it is suggested that it is the micro-scale rather than the nano-scale Marngoni film that induces the fingering instability shown in Figure 6-2. The Marangoni flow at nano-scale is not addressed further in this work.

To understand the formation of fingering instability, a schematic diagram of the weld pool cross section is shown in Figure 6-15. The appearance of fingering flow is due to the bulk liquid spreading on the precursor film. As shown in Figure 6-7, this micro-scale Marangoni film spreads ahead of bulk flow, thus the bulk flow spreads on a liquid film rather than on the solid. The spreading acts at the liquid/liquid/gas contact line and the spreading parameter, equation 6.5 is now:

$$S = \gamma_{LV_{film}} - \gamma_{LV_{bulk}} \quad (6.7)$$

where $\gamma_{LG_{film}}$ and $\gamma_{LG_{bulk}}$ refer to the surface tension of bulk liquid and precursor film. This makes the spreading parameter independent of the free energy of the solid surface. However, the spreading kinetics of the precursor film does depend on the free surface of solid since there is a contact interface between them.

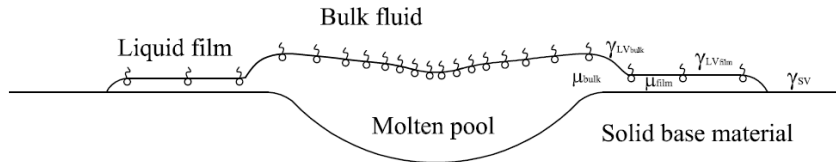


Figure 6-15. Schematic diagram of bulk liquid spreading on precursor film.

Both bulk flow and Marngoni film are driven by Marngoni force since the temperature decreases with increasing radial distance from the centre of the pool. In the region of the molten pool shown in Figure 6-15, Marangoni driven convection can distribute and mix oxygen from surface layer to the bulk pool. Due to its high flow velocity, which is in the order of one meter per second (see measurements in chapters 3 and 4), the oxygen distribution is almost homogenous in the bulk pool as shown in chapter 5. However, for the precursor film, convection is limited due to the low thickness and relatively low temperature gradient. Additionally, the total volume of the bulk molten pool is far larger than that of the precursor film; this leads to a lower oxygen concentration in the bulk liquid and a higher concentration in the precursor film. As a result, a difference of oxygen concentration occurs at the liquid/liquid interface, and results in a difference in surface tension at the contact line. The experimental measurements shown in Figure 6-8 support the above comment; the measured oxygen concentration in the fingering region is lower than that of the precursor film region, while both are much higher than that of the base metal.

The Peclet number is a measure of the relative strength of Marangoni driven convection to either surface diffusion or bulk diffusion. Here the surface Peclet number Pe_s and bulk Peclet number Pe_b are defined as²¹³

$$Pe_s = \frac{u_s L_s}{D_s} \quad (6.8)$$

and

$$Pe_b = \frac{u_b L_b}{D_b}, \quad (6.9)$$

where u_s and u_b are the characteristic Marangoni velocities, in the order of millimeters per second and meters per second respectively; L_s and L_b are characteristic lengths with scales of microns and millimeters; D_s and D_b are the diffusivities in precursor film and bulk flow respectively. It is seen that the diffusivities D_s and D_b are in the same order because the temperature and partial pressure of oxygen are in the same order; $u_s \ll u_b$ and $L_s \ll L_b$, thus for the two Peclet numbers, we have $Pe_s \ll Pe_b$, which suggest that convection plays a more important role in transporting oxygen in the bulk liquid than in the thin precursor film. Again, this suggests that the oxygen concentration in the precursor film is higher than that in the bulk pool.

Gravitational forces do not appear to be significant because the Bond number $Bo \ll 1$, where Bo is given by

$$Bo = \frac{\rho g L^2}{\gamma}, \quad (6.10)$$

and ρ , g , L and γ are the density of liquid metal, gravitational acceleration, a characteristic length and the surface tension of the liquid metal respectively. Thus, the Marangoni force is the main factor influencing the flow and spreading patterns.

As shown in Figure 6-4, the thickness of the precursor film is around 3 microns, which is much larger than that for which consideration should be given to the influence of van der Waals forces.^{161,162} Matar and Troian¹⁶¹ proposed that van der Waals forces become significant in regions of the film that have been thinned to less than 100 nm. In this thesis, the van der Waals force is not considered although it may play an important role for the initial melting at grain boundaries. According to the above discussions, the spreading flow is from bulk liquid to precursor film, and oxygen diffusion is from the precursor film into bulk liquid due to the oxygen concentration gradient. As suggested by Troian *et al.*²¹⁰ the basic mechanism of fingering is similar to a Saffman-Taylor instability due to an adverse mobility gradient at the spreading interface of the two liquids.²¹³ The fingering instability in the weld pool boundary is likely to be due to the adverse gradient of Marangoni force and surfactant concentration.

For the Staffman-Taylor instability,²¹⁹ there are other factors that may induce fingering instability such as viscosity and density differences between bulk flow and the precursor film. The bulk liquid is generated by melting the base metal, however, the chemical composition of the precursor film is mainly generated from oxidized grain boundaries, where elemental segregation occurs. This in turn might generate a gradient of viscosity and density at the bulk/film interface.

6.4.4 Correlation between high and low temperature systems

As shown in Figure 6-16, the so called ‘bump’¹⁶⁷ *i.e.*, a build up of liquid immediately preceding the contact line, has not been obviously found at the precursor film, it is not clear if a ‘bump’ occurs during spreading, since the surface profile is measured after solidification; however, it does occur at the fingering front. Compared with the finger spreading formed at low temperatures, there is no secondary finger¹³⁴ along the initial fingers; the main reason probably is that the Marngoni force gradient is in the radial direction, which is not beneficial to the formation of the secondary fingers along the tangential direction.

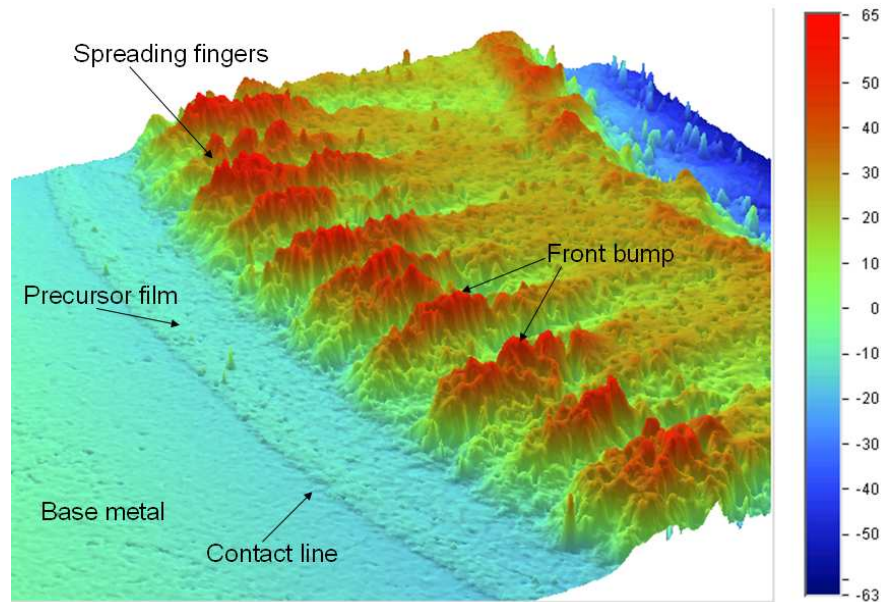


Figure 6-16. Surface profile of Marangoni film and spreading fingers after solidification

An important characteristic of the metal precursor film is that the spreading duration is short, compared with the phenomena observed in low temperature organic liquids, where the spreading duration can be several seconds or even a few minutes. As shown in Figure 6-6, the spreading speed decreases with time due to the decreasing temperature gradient. According to traditional experimental and theoretical results at low temperatures,

fingering instability phenomena can be induced when one liquid with a surfactant solution spreads on a thin wetting film, and surface coverage proceeds much more quickly than in ordinary spreading.²⁰⁹ This is similar to the current high temperature case when the oxygen level is increased, and higher oxygen concentration improves the wettability and spreading speed.

Although the fingering instability has not been reported before for liquid metal flow in high temperature systems, Saiz and Tomsia²¹⁵ studied the Marangoni film for a liquid metal spreading on a flat unreactive substrate. The present work shows that finger spreading flow also exists when liquid metal spreads on a thin Marangoni film. Based on the evidence presented here, the phenomenon is believed to be similar to that observed at low temperatures.

6.5 Conclusion

Although fingering spreading flow in organic liquids at low temperatures is well understood, it was not known whether this phenomenon existed for liquid metal flow at high temperatures. As shown in this chapter, finger spreading of a liquid metal can occur but only after the formation of a precursor Marangoni film.

The deformation of grain boundaries forms grain grooves upon heating, which affects liquid spreading and induces a liquid net structure when the oxygen level is low. These liquid nets merge with increasing oxygen concentration, and finally result in the formation of a Marangoni film and fingering instability.

The current experimental results indicate that the main mechanism for fingering instability of liquid metal is adverse force gradients; this is similar to the mechanism in low temperature systems. Here, the finger spreading in a high temperature system has been captured for the first time.

7 Conclusions and future work

7.1 Conclusions

In the current research, the main objective has been to investigate fluid flow behaviour in welding by experimental means. Both laser and arc welding were examined using a high-speed visualization system, which provided real-time measurements on both qualitative flow patterns and quantitative flow velocities. The influence of fluid flow on heat and mass transfer in welding has been addressed as an important issue for final weld pool shape and elemental distribution. It has been noted that flow motions are quite complex, oscillations and instabilities occur quite often. There are several factors influencing the flow of the weld pool, such as the physical properties of the base metal and the energy distribution of the heat source.

This thesis mainly focuses on the fluid dynamics of liquid stainless steel weld pools. The most significant contributions from this work are briefly highlighted below:

Measurement of the velocity field over the whole surface on the weld pool is reported here for the first time. The complete velocity field can capture complex flow motions, such as rotational flow, outward flow and inward flow, which can occur simultaneously. Measurements of surface flow fields made in this work can be used to validate numerical simulations and provide better understanding of physical mechanisms occurring during welding.

For both laser and arc welding, experimental results show that asymmetrical flow patterns dominate in all procedures, oscillations occur during both outward flow and inward flow. Numerical simulations have yet to incorporate the heat and mass transfer induced by asymmetrical flow. The asymmetrical flow patterns observed suggest that numerical models based on symmetrical assumptions do not adequately represent real weld pools.

Interfacial instability occurring in inward flow for a moving arc source can induce frequent vortex shedding. These vortices occur alternately on each side of the weld pool towards the weld pool rear. For laser spot welding, the interfacial instability induces rotational inward flow.

Measurements of the influence of oxygen from the environment suggest that dynamic oxygen absorption should be considered in computations of surface tension. Models that simply assume that the oxygen concentration in the shielding gas is the same as that in the liquid metal, cannot describe the dynamic development of a weld pool.

It is found that the absorbed oxygen can flip the liquid flow motion from outward to inward flow (provided the initial oxygen concentration in the liquid metal is quite low), indicating that the surface tension gradient was changed from a negative to a positive

value. Oxygen not only changes the surface tension gradient but also affects laser energy absorption, and resulting in differences in the size of the final weld pool.

The appearance of gas pores during inward flow occurs as a result of air entrainment at the interface, where fast metal flow leads to free surface deformation, causing gas to be drawn into the narrow channel of a cusp singularity.

A method has been developed for three dimensional observation based on a single high-speed camera by adding two groups of parallel mirrors in front of the lens; two individual images are obtained from two different angles, based on which a three dimensional surface velocity can be calculated. Calculation of the images is carried out using appropriate coordinate transforms and image calibrations.

The formation of grain grooves is due to the deformation of grain boundaries upon heating, and spreading liquid can move faster on the grain surface than in the grain grooves. Deformation of the liquid front delays spreading when the liquid meets a grain groove.

Fast flow driven by Marangoni forces can distribute the dissolved oxygen homogeneously in the weld pool. Convection plays a significant role in elemental distribution.

Two free surfaces are formed during penetration welding; inward flows occur on both the top and bottom surfaces. Oscillations occurring on two free surfaces can induce multi-cellular flow, which changes the heat and mass transfer, resulting in strong deformation of the free surface being frozen into the final weld profile. This has not been considered in numerical simulations to date.

Initial melting occurring at grain boundaries has an effect on the spreading liquid flow; a liquid net structure can be formed on the base metal surface when oxygen concentration in the shielding environment is less than about 1%.

Fingering instability phenomena is captured for the first time for a high temperature liquid metal system, a potential explanation is the formation of competing Marangoni forces. Inside the bulk area, the temperature gradient initially generates a negative surface tension gradient and drives the liquid flow outward; however, the flow is inward at the bulk/precursor film interface due to the gradient of surfactant concentration.

Fingering instability only occurs when a Marangoni film forms ahead of the main liquid pool. The formation of Marangoni film is influenced by oxygen concentration, which improves the wettability of liquid metal.

7.2 Future work

Although the previous issues provide experimental measurements, which could be helpful for understanding welding, there are still many challenges remaining. For further understanding of the weld pool fluid flow phenomena, the following aspects should not be missed:

Internal flow visualization should be considered in the future, because current surface observation cannot provide information about flow conditions inside the weld pool. Three dimensional high energy x-ray visualization could provide more information than surface visualization.

Keyhole dynamics is still not clearly understood, although many researchers tried to build numerical models to describe such behaviour. Real time experimental measurements on a supersonic plasma require equipment with a fast response to obtain sufficiently detailed information about the dynamic parameters during keyhole welding.

Mass transfer at the gas-liquid interface needs to be addressed based on consideration of fluid flow driven by surface tension. Absorbed oxygen can change flow motion and generate an oxide layer which increases the energy absorption. The dynamic process at the gas-liquid interface has not yet been described satisfactorily. There is still no adequate theoretical model to describe the details of oxygen transportation. Furthermore, other gases can have an influence on the final metallurgical properties of a weld, such as nitrogen and hydrogen. All these effects suggest that the dynamic transportation of gases should be studied further.

Energy absorption efficiency as a function of time and evolving weld pool chemistry needs to be considered. At present, it is assumed to be a constant in most publications; this is doubtful in view of the results of the current research, where different oxygen concentration in the shielding gas led to different weld pool shape and the onset time of liquid melting. The energy absorption efficiency should consider factors such as the influence of oxidation and deformation of the free surface, and can be divided into solid and liquid parts.

Interfacial instabilities inducing air entrainment during inward flow should be analyzed theoretically to provide suggestions for avoiding the generation of porosities at the flow interface.

Both liquid metals spreading on solid and liquid metal spreading on liquid need further investigations. These will require special experimental arrangements to monitor the spreading procedure as well as the variation of contact angle.

It is still not known whether the current observation on fingering instability occurs for other metals. Further studies should be undertaken to check the spreading of pure metal rather than alloys, since simulations on pure metals is easier than alloys.

Two-phase flow in liquid metal systems is not understood well, although it occurs quite often during welding. For example, gas entrainment phenomena can induce residual porosity in the weld pool, affecting the final mechanical properties.

Although the mixing of consumables with the base material has not been included in this thesis, the migration of liquid metal from a filler wire needs to be studied since the elemental distribution in the weld pool may have a significant influence in the final properties of a welded joint.

Due to the scale influence, the fluid dynamics of a liquid metal on a micro scale may exhibit different phenomena from flow on a macro scale. Both measurement and

Zhao CX: Measurements of fluid flow in weld pools

simulation for micro welding should be approached in the future. Current industrial applications also require understandings on this topic.

Reference

1. DebRoy T. (1995), "Physical processes in fusion welding", *Rev. Mod. Phys.* **67**, 85-112
2. Eustathopoulos N, Nicholas MG, Drevet B. (1998), "Wetting ability at high temperatures", Pergamon Materials Series 3, Elsevier science ltd.
3. Davis JR(Ed.) (1993), ASM Speciality Handbook: Aluminium and Aluminium Alloys, ASM International, Metals Park, OH
4. Kou S. (1986), "Welding metallurgy and weldability of high strength aluminium alloys", *Weld.Res.Coun.Bull.*, **320**, 1-20
5. Kou S. (2003), "Welding Metallurgy", 2nd edition, John Wiley & Sons, Hoboken, New Jersey.
6. Linton LM, Ripley MI. (2008), "Influence of time on residual stresses in friction stir welds in agehardenable 7xxx aluminium alloys", *Acta.Mater.*, **56(16)**, 4319-4327
7. Threadgill PL, Leonard AJ, Shercliff HR, Withers PJ. (2009), "Friction stir welding of aluminium alloys", *Int.Mater.Rev.*, **54 (2)**, 49-93
8. Norman AF, Hyde K, Costello F, Thompson S, Birley S, Prangnell PB. (2003), "Examination of the effect of Sc on 2000 and 7000 series aluminium alloy castings:For improvements in fusion welding", *Mater.Sci.Eng.A.*, 2003, **354 (1-2)**, 188-198
9. Norman AF, Birley SS, Prangnell PB. (2003), "Development of new high strength Al-Sc filler wires for fusion welding 7000 series aluminium aerospace alloys", *Sci.Technol.Weld.Joi.*, **8 (4)**, 235-245
10. Heiple CR, Roper JR. (1981), "Effect of selenium on GTAW fusion zone geometry", *Weld. J.* **60**, 143s-145s
11. Heiple CR, Roper JR. (1982), "Mechanism for minor element on GTA fusion zone geometry", *Weld. J.* **61**, 97s-102s
12. Woods RA, Milner DR. (1971), "Motion in the weld pool in arc welding", *Weld. J.* **50(4)**, 163s-173s
13. Erceer GM, Tzavaras A, Gokhale A, Brody HD. (1982), "Weld fluid motion and ripple formation in pulsed current GTAW", Trends in welding research ASM, pp 419-442
14. Hall AC, Knorovsky GA, Robino CV, Brooks J, Maccallum DO, Reece M, Poulter G. (1982), "Characterizing the microstructure of a GTA weld in process using high-speed camera, High magnification digital imaging", 11th Int.Conf.

- on Computer.Tech.in welding, Columbus OH, 117-124
15. Hall AC, Robino CV. (2004), "Association of microstructural features and rippling phenomenon in 304 stainless steel gas tungsten arc welds", *Sci. Technol. Weld. Joi.* **9(2)**, 103-108
 16. Kraus HG. (1989), "Experimental measurement of stationary SS 304, SS 316 and 8630 GTA weld pool surface temperatures", *Weld. J.*, **68**, 269-279
 17. Zacharia T, David SA, Vitek JM, Kraus HG. (1991), "Computational modeling of stationary Gas Tungsten Arc weld pools and comparison to stainless steel 304 experimental results", *Metall. Trans. B.* **22B**, 243-257
 18. Mundra K, DebRoy T, Kelkar K. (1996), "Numerical prediction of fluid flow and heat transfer in welding with a moving heat source", *Numer. Heat. Transfer A.* **29**, 115-127
 19. Jackson J.D: (1998), *Classical Electrodynamics*, 3rd edition, Wiley, New York
 20. Zhang W. (2005) (PhD thesis), "Fluid flow and microstructure evolution during fusion welding of alloys", The Pennsylvania state university, Department of materials science and engineering, USA
 21. Pitscheneder W, Ebner R, Hong T, DebRoy T, Mundra K, Benes R.(1998), "Experimental and Numerical Investigation of Transport Phenomena in Conduction Mode Weld Pools", in *Mathematical Modelling of Weld Phenomena 4*, edited by H. Cerjak
 22. Pitscheneder, W; Hong, T; Debroy, T; Ebner, R; Mundra, K. and Benes, R. (2000), "Experimental and numerical investigation of transport phenomena in conduction mode weld pools in laser welding", *Welding in the World.* **44(6)**, 25-36
 23. Verlarde MG, Normand C. (1980), "Convection", *Scientific American*:79-93
 24. Henrikson P. (2005) "Visualisation of Weld Pool Surface Flow During TIG Welding of Stainless Steel 316L Plates", *Mathematical Modelling of Weld Phenomena 7.* 125-147, edited by H.Cerjak, H.K.D.H.Bhadeshia. Publ: London SW1Y 5DB, UK; Institute of Materials;
 25. Henrikson P. (2003), Volvo Aero corporation, Swedish patent SE521787 and PCT international publication Wo03/086695
 26. Delapp D, Cook G, Strauss A, Hofmeister W. (2005), "Quantitative observations of surface flow and solidification on autogenous GTA weld pools", *ASM proceedings of the international conference, Trends in welding research*
 27. Delapp D. (2005), "Observations of solidification and surface flow on autogenous tungsten arc weld pools", PhD thesis, Vanderbilt University, Nashville, Tennessee, USA

Reference

28. Heiple CR, Burgardt P, Roper JR. (1986), "Control of GTA Weld Pool Shape, Advances in Welding Science and Technology, Trends in Welding Research"; ASM: Gatlinburg, TN, 1986 ASM international conference proceedings 387-392
29. Mizutani M, Katayama S, Matsunawa A. (2003), "Observation of molten metal behavior during laser irradiation-basic experiment to understand laser welding phenomena", first international symposium on high-power laser macro processing. Proceedings of SPIE Vol.4831
30. Naito Y, Mizutani M, Katayama S. (2006), "Effect of oxygen in ambient atmosphere on penetration characteristics in single yttrium-aluminum-garnet laser and hybrid welding", *J. Laser. Appl.* **18(1)**, 21-27
31. Matsunawa A, Mizutani M, Katayama S (2003), "Porosity formation mechanism and its prevention in laser welding", *Weld. Int.* **17**, 431-437
32. Matsunawa A, Seto N, Mizutani M, Katayama S. (1998), "Liquid motion in keyhole laser welding, Laser Materials Processing", Proceedings, Conference, ICALEO '98, Orlando, Florida, Section G; Orlando, FL; USA; 16-19 Nov. 1998. 151-160.
33. Katayama S, Seto N, Mizutani M, Matsunawa A. (2000), "X-ray transmission in-situ observation of fluid flow inside molten pool during TIG arc welding of stainless steel", Transactions of JWRI, vol.30. 2001. Special Issue: HTC-2000 (High Temperature Capillarity). Reviewed Proceedings, Third International Conference, Nov 19-22, Kurashiki, Japan
34. Zhang YM *et al.* (2006), "Observation of a dynamic specular weld pool surface", *Meas. Sci. Technol.* **17**, L9-L12
35. Song HS, Zhang YM. (2007), "Three-dimensional reconstruction of specular surface for a gas tungsten arc weld pool", *Meas. Sci. Technol.* **18(12)**, 3751-3767
36. Song HS, Zhang YM. (2007), "Image processing for measurement of three-dimensional GTA weld pool surface", *Weld. J.* **86(10)** 323-330
37. Smith JS, Balfour C. (2005), "Real-time top-face vision based control of weld pool size", *Industrial Robot: An international Journal.* **32:4**, 334-340
38. Beardsley H, Zhang Y, Kovacevic R. (1994), "Infrared sensing of full penetration state in gas tungsten arc welding", *Int. J. Mach. Tools. Manufact.* **34**, 1079-1090
39. Pietrzak KA, Packer SM. (1994), "Vision-Based Weld Pool Width Control", *ASME J. Eng. Ind.*, **116**, pp. 86-92.
40. Brzakovic D, Khani DT. (1991), "Weld Pool Edge Detection for Automated Control of Welding", *IEEE Trans. Rob. Autom.* **7**, 397-403.

41. Zhao DB *et al.* (2003), "Extraction of three-dimensional parameters for weld pool surface in pulsed GTAW with wire filler", *J. Manuf. Sci. E-TASME*, **125**, 483-503
42. Zhang YM, Wu L, Walcott BL, Cheng DH. (1993), "Determining joint penetration in GTAW with vision sensing of weld face geometry", *Weld. J.* **72**, 463-469
43. Kovacevic R, Zhang YM. (1995), "Vision sensing of 3D weld pool surface", 4th Int.Conf.on trends in welding research (Gatlinburg,TN,USA) 85-91
44. Saeed G, Lou M, Zhang YM. (2004), "Computation of 3D weld pool surface from the slope field and point tracking of laser beams", *Meas. Sci. Technol.* **15**, 389-403
45. Wang JJ *et al.* (2005), "Obtaining weld pool vision information during aluminum alloy TIG welding", *Int. J. Adv. Manuf. Tech.*, **26**, 219-227
46. Zhang GJ *et al.* (2006), "Reconstructing a three-dimensional P-GMAW weld pool shape from a two-dimensional visual image", *Meas. Sci. Technol.* **17**, 1877-1882
47. Tsai MC, Kou S. (1990), "Weld pool convection and expansion due to density variations", *Numer. Heat. Transfer A*, **17**, 73-89
48. Tsai MC, Kou S. (1989), "Marangoni convection in weld pools with a free surface", *Int. J. Numer. Meth. Fluids.*, **9**, 1503-1506
49. Goldak J, Chakravarti A, Bibby M. (1984), "A new finite element model for welding heat sources", *Metall. Trans. B.* **15B**, 299-305
50. Xiao YH, Ouden G den. (1990), "A study of GTA weld pool oscillation", *Weld. J.* **69**, 289-93s
51. Xiao YH, Ouden G den. (1993), "Weld pool oscillation during GTA welding of mild steel", *Weld. J.* **72**, 428-434
52. Yudodibroto BYB, Hermans MJM, Hirata YG, Quden G. den, Richardson IM. (2006), "Pendant droplet oscillation during GMAW", *Sci. Technol. Weld. Joi.* **11(3)**, 308-314
53. Ha EJ, Kim WS. (2005), "A study of low-power density laser welding process with. evolution of free surface", *Int. J. Heat. Fluid. Flow.* **26**, 613-621
54. Hong K, Weckamn DD, Weckamn AB, Strong AB. (1995), Trends in welding research, ASM international conference proceedings, 399-404
55. Tennekes H, Lumley JL. (1982), "A first course in turbulence", The MIT press
56. Hirt CW, Nichols BD. (1981), "Volume of fluid (VOF) method for the dynamics of free boundaries", *J.Comp.Phys.* **39**, 210
57. Haidar J. (1998), "A theoretical model for gas metal arc welding and gas

Reference

- tungsten arc welding”, *J.Appl.Phys.* 84(7), 3518-3529
58. Lee JY, Ko Sh, Farson DF. (2002), “Mechanism of keyhole formation and stability in stationary laser welding”, *J.Phys.D-Appl.Phys.*, **35(13)**, 1570-1576
 59. Kim JW, Na SJ. (1995), “Study on the effect of contact tube-to-workpiece distance on weld pool shape in gas metal arc welding”, *Weld. J.* 74,141s-1522
 60. Cao ZN, Dong P. (1998), “Modeling of GMA weld pools with consideration of droplet impact”, *J.Eng.Mater.Technol. Trans. ASME*, **120**,313
 61. Wu CS, Dorn L. (1994), “Computer simulation of fluid dynamics and heat transfer in full-penetrated TIG weld pools with surface depression”, *Comput.Mater.Sci.* **2**, 341
 62. Malinowski-Brodnicka M, Quden G. den, Vink WJP. (1990), “Effect of Electromagnetic Stirring on GTA Welds in Austenitic Stainless Steel”, *Weld. J.* **69(2)** 52s-59s
 63. Choo RTC, Szekely J. (1994), “Possible role of turbulence in GTA weld pool behaviour”, *Weld. J.* **73(2)** 25s-31s
 64. Touloukian YS. (1967), “Thermophysical properties of high temperature solid materials”, Vol3, Ferrous alloys, McMillan Co., New York.
 65. Yang Z, DebRoy T. (1999), “Modeling macro- and microstructures of gas-metal-arc welded HSLA-100 steel, *Mater. Trans. B.* **30B**, 483-493
 66. Chakraborty S, Sarkar S, Dutta P. (2002), “Scaling analysis of momentum and heat transport in gas tungsten arc weld pools”, *Sci. Technol. Weld. Joi.* **7(2)**, 88-92
 67. Oreper GM, Szekely J. (1987), “Comprehensive representation of transient weld pool development in spot welding operations”, *Mater. Trans. A.* 18A,1325-1332
 68. Limmaneevichitr C, Kou S. (2000), “Experiments to simulate effect of Marangoni convection on weld pool shape”, *Weld. J.* **79(8)**, 231s-237s
 69. Limmaneevichitr C, Kou S. (2000), “Visualization of Marangoni convection in simulated weld pools”, *Weld. J.* **79(5)**, 126s-135s
 70. Limmaneevichitr C, Kou S. (2000), “Simulated weld pools containing a surface active agent”, *Weld. J.* **79(11)**, 324S-330
 71. Limmaneevichitr C. (2000), PhD thesis, “Flow visualization of Marangoni convection in simulated weld pools”, University of Wisconsin-Madison, USA
 72. Raffel M, Willert C, Kompenhans J. (1998), “Particle image velocimetry: a practical guide”, Springer
 73. MPDB : MPDB v6.69 www.jahm.com

74. Brooks RF, Quested PN. (2005), "The surface tension of steels", *J. Mater. Sci.*, **40**, 2233-2238
75. Adrian R. (1991), "Particle-imaging techniques for experimental fluid mechanics", *Annu. Rev. Fluid. Mech.* **23**, 261-304
76. Westerweel J. (1993), PhD thesis, Digital particle image velocimetry: theory and application, NL
77. Westerweel J, Scarano F. (2005), "Universal outlier detection for PIV data", *Exp. Fluids.* **39**, 1096-1100
78. Chen WLT, Heberlein J, Pfender E. (1996), "Critical analysis of viscosity data of thermal argon plasmas at atmospheric pressure", *Plasma. Chem. Plasma P.*, **16(4)**, 635-650
79. Allum CJ. (1981), "Gas flow in the column of a TIG welding arc", *J. Phys. D: Appl. Phys.* **14**, 1041-1059
80. Sahoo P, DebRoy T, McNallan MJ. (1988), "Surface tension of binary metal-surface active solute systems under conditions relevant to welding metallurgy", *Mater. Trans. B.* **19B**, 483-491
81. Kou S, Wang Y.H. (1985), "Three-dimensional convection in laser melted pools", *Mater. Trans. A.* **17A**, 1986-2265
82. Lawson WHS, Kerr HW. (1976), "Fluid motion in GTA weld pools-1. Flow patterns and weld pool homogeneity", *Weld. Res. Int.* **6 (5)**, 63-77
83. Lawson WHS, Kerr HW. (1976), "Fluid motion in GTA weld pools-2. Weld pool shapes", *Weld. Res. Int.* **6(6)**, 1-17
84. Atthey DR. (1980), "A mathematical model for fluid flow in a weld pool at high currents", *J. Fluid Mech.* **98(4)**, 787-801
85. Oreper GM, Eagar TW, Szekely J. (1983), "Convection in arc weld pools", *Weld. J.* **62**, 307s-312s
86. Kou S, Wang Y.H. (1985), "Three-dimensional convection in laser melted pools", *Mater. Trans. A.* **17A**, 2265-2270
87. Kou S, Sun DK. (1985), "Fluid-flow and weld penetration in stationary arc welds", *Mater. Trans. A.* **16A (2)** 203-213
88. Chakraborty N, Chakraborty S. (2005), "Influences of sign of surface tension coefficient on turbulent weld pool convection in a gas tungsten arc welding (GTAW) process: A comparative study", *J. Heat. Transfer.* **127**, 848-862
89. Chakraborty N, Chakraborty, S, Dutta P. (2003), "Modelling of turbulent transport in arc welding pools", *Int. J. Heat. Mass. Tran.*, **13(1)**, 7-30
90. Hong K, Weckman DC, Strong AB, Zheng W. (2003), "Vorticity based turbulence model for thermofluids modelling of welds", *Sci. Technol. Weld. Joi.*

- 8(5)**, 313-324
91. Jaidi J, Dutta P. (2004), "Three-dimensional turbulent weld pool convection in gas metal arc welding process", *Sci. Technol. Weld. Joi.* **9(5)**, 407-414
 92. Hong K, Weckman DC, Stgong AB, Zheng W. (2002), "Modelling turbulent thermofluid flow in stationary gas tungsten weld pools", *Sci. Technol. Weld. Joi.* **7(3)**, 125-136
 93. Hong K, Weckman DC, Strong AB, Zheng W. (2003), "Vorticity based turbulence model for thermofluids modelling of welds", *Sci. Technol. Weld. Joi.* **8(5)**, 313-324
 94. Rott N. (1990), "Note on the history of the Reynolds number", *Annu. Rev. Fluid. Mech.* **22**, 1-11
 95. Winkler C, Amberg H, Inoue H, Koseki T. (1998), "A numerical and experimental investigation of qualitatively different weld pool shapes", *Mathematical modelling of weld phenomena* 4, 37-69
 96. Aboutalebi MR, Hassan M, Guthrie RIL. (1995), "Numerical study of coupled turbulent flow and solidification for steel slab clusters", *Numer. Heat. Transfer.* **28**, 279-299
 97. Joshi Y, Dutta P, Schupp PE, Espinosa D. (1997), "Nonaxisymmetric convection in stationary gas tungsten arc weld pools", *J. Heat. Transfer.* **119**, 164-172
 98. Chakraborty S, Sarkar S, Dutta P. (2002), "Scaling analysis of momentum and heat transport in gas tungsten arc weld pools", *Sci. Technol. Weld. Joi.* **7(2)**, 88-94
 99. Zhao CX, Steijn V, Richardson IM, Saldi S, Kleijn CR. (2008), "Experimental characterization of GTA weld pool surface flow using PIV", 8th international conference on trends in welding research, June1-6, pine mountain, Georgia USA
 100. Zhao YZ, Zhao YZ, Zhao HY, Lei YP, Shi Y.W. (2007), "Theoretical study of Marangoni Convection and weld penetration under influence of high oxygen content in base metal", *Sci. Technol. Weld. Joi.*, **12(5)**, 410-417
 101. Kaul R. et.al, (2007) "Effect of active flux addition on laser welding of austenitic stainless steel", *Sci. Technol. Weld. Joi.* **12(2)**, 127-137
 102. Modenesi, PJ, Apolinario ER, Pereira IM. (2000) "TIG welding with single-component fluxes", *J. Mater. Process. Tech.* **99**, 260-265
 103. Xu YL, Dong YH, Wei YH, Yang CL. (2007), "Marangoni convection and weld shape variation in A-Tig welding process", *Theor. Appl. Fract. Mec.* **48**, 178-186
 104. Tanaka M. et al. (2000), "Effect of activating flux on arc phenomena in gas

- tungsten arc welding”, *Sci. Technol. Weld. Joi.* **5(6)**, 397-402
105. Aidun DK, Martin SA. (1997), “Effect of sulfur and oxygen on weld penetration of high-purity austenitic stainless steels”, *J. Mater. Eng Perform.* **6(4)**, 496-502
106. McNallan MJ, DebRoy T. (1991), “Effect of temperature and composition on surface tension of Fe-Ni-Cr alloys containing sulphur”, *Metall. Trans. B.* **22**, 557-560
107. Heiple CR, Roper JR, Stagner RT, Aden RJ. (1983), “Surface active element effects on the shape of GTA, Laser and electron beam weld”, *Weld. J.* **62(3)**, 72s
108. Takeuchi Y, Takagi R, Shinoda T. (1992), “Effect of bismuth on weld joint penetration in austenitic stainless-steel”, *Weld. J.* **71(8)**, 283s
109. Bad'yanov B.N. (1975), *Avtom.Svarka.* **1**, 75
110. Heiple CR, Burgardt P. (1985), “Effects of SO₂ shielding gas additions on GTA weld shape”, *Weld. J.* **64**, 159s
111. Lu SP, Fujii H, Nogi K. (2004), “Sensitivity of Marangoni convection and weld shape variations to welding parameters in O-Ar shielded GTA welding”, *Scripta. Mater.* **51**, 271-277
112. Lu SP, Fujii H, Nogi K. (2006), “Effect of welding parameters on GTA weld shape for pure iron plate under Ar-O₂ mixed shielding”, *J. Mater. Sci. Technol.*, **22(3)**, 359-366
113. Lu SP, Fujii H, Nogi K. (2004), “Marangoni convection in weld pool in CO₂-Ar-shielded gas thermal arc welding”, *Metall. Mater. Trans. A.* **35**, 2861-2867
114. Lu SP, Fujii H, Nogi K. (2005), “Influence of welding parameters and shielding gas composition on GTA weld shape”, *ISIJ. Int.* **45(1)**, 66-70
115. Pitscheneder W, DebRoy T, Mundra K, Ebner R. (1996), “Role of sulfur and processing variables on the temporal evolution of weld pool geometry during multi-kilowatt laser beam welding of steel”, *Weld. J.*, **75(3)**, 71s-80s
116. Wang Y, Tsai HL. (2001), “Effects of surface active elements on weld pool fluid flow and weld penetration in gas metal arc welding”, *Metall. Mater. Trans. B* **32(3)**, 501-515
117. Wang Y, Shi Q, Tsai HL. (2001), “Modeling of the effects of surface-active elements on flow patterns and weld penetration”, *Metall. Mater. Trans. B.* **32(1)**, 145-161
118. Zacharia, T, David SA, Vitek JM *et al.* (1989), “Weld pool development during gas and laser-beam welding of type-304 stainless-steel. 1. Theoretical-analysis”, *Weld. J.* **68(12)**, 409s-509s

Reference

119. Tanaka M, Lowke JJ. (2007), "Predictions of weld pool profiles using plasma physics", *J. Phys. D. Apply. Phys.* **40**, R1-R23
120. Zhang RH, Fan D. (2007), "Numerical simulation of effects of activating flux on flow patterns and weld penetration in ATIG welding", *Sci. Technol. Weld. Joi.* **12(1)**, 15-23
121. Kou S, Wang YH. (1986), "Weld pool convection and its effect", *Weld. J.* **65(3)**, 63s-70s
122. Zacharia T, David SA, Vitek JM, Debroy T. (1990), "Modeling of Interfacial Phenomena in Welding", *Metall. Trans. B.* **21**, 600
123. Hermann S, Gersten K. (2003), "Boundary-layer theory", (8th Edition) Springer, p160
124. Aboutalebi MR, Hassan M, Guthrie RLL. (1995), "Numerical study of coupled turbulent flow and solidification for steel slab clusters", *Numer. Heat. Tr. A-Appl.* **28**, 279-299
125. Bejan A. (1995), "Convection heat transfer", John Wiley and Sons, p278
126. Mnich C, Al-Bayat F, Debrunner C, Steele J, Vincent T. (2004), ASME Proc. 2004, Japan-USA Symp. on Flexible Automation, Denver, CO, USA, 9-21 July
127. Choong DY, Lee J. "3D measurement of weld pool using biprism stereo vision sensor", <http://joining1.kaist.ac.kr/research/vision.htm>, Seoul National University
128. Sonka M, Hlavac V, Boyle R. (2008), "Image processing, analysis, and machine vision", (3rd edition) Thomson
129. http://www.vision.caltech.edu/bouguetj/calib_doc/
130. Zhang Z, Deriche R, Faugeras O, Luong QT. (1995), "A robust technique for matching two uncalibrated images through the recovery of the unknown epipolar geometry", *Artif. Intell.* **78**, 87-119
131. Zhao CX, Steijn V, Richardson IM, Kleijn CR, Kenjeres S, Saldi Z. (2009), "Unsteady interfacial phenomena for weld pool inward flow with an active surface oxide", *Sci. Technol. Weld. Joi.* **14(2)**, 132-140
132. Eustathopoulos N, Joud JC. (1980), Current topics in materials science volume 4, ed. Kaldis E. Amsterdam: North-Holland, 281
133. Zacharia T, David SA, Vitek JM, Debroy T. (1989), "Weld pool development during GTA and laser beam welding of type 304 stainless steel Part II. Experimental correlation", *Weld. J.* **68(12)**, 510-519
134. Mills KC, Keene BJ. (1990), "Factors affecting variable weld penetration", *Int. Mater. Review.* **35(4)**, 185-216
135. Pitscheneder W, DebRoy T, Mundra K, Ebner R. (1996), "Role of sulfur and

- processing variables on the temporal evolution of weld pool geometry during multikilowatt laser beam welding of steels”, *Weld. J.* **75(3)**, 71-80
136. Zhao CX, Richardson IM, Kenjeres S, Kleijn CR, Saldi Z. (2009), “A stereo vision method for tracking particle flow on the weld pool surface”, *J. Appl. Phys.* **105(12)**, 123104
137. Tanaka M, Tashiro S, Satoh T, Murphy AB, Lowke JJ. (2008), “Influence of shielding gas composition on arc properties in TIG welding”, *Sci. Technol. Weld. Joi.* **13(3)**, 225-231
138. Modenesi PJ, Apolinario ER, Pereira IM. (2000), “TIG welding with single component fluxes”, *J. Mater. Process. Tech.* **99**, 260-265
139. Aidun DK, Martin SA. (1997), “Effect of sulfur and oxygen on weld penetration of high-purity austenitic stainless steels”, *J. Mater. Eng. Perform.*, 1997, **6(4)**, 496-502
140. Lu SP, Dong WC, Li DZ, Li YY. (2009), “Numerical simulation for welding pool and welding arc with variable active element and welding parameters”, *Sci. Technol. Weld. Joi.* **14(6)**, 509-516
141. Armstrong JT. (1991), “Quantitative elemental analysis of individual microparticles with electron beam instruments”, In *Electron Probe Quantitation*, Heinrich, K.F.J., and Newbury, D.E. (eds.), pp 261-315, Plenum Press
142. Mishra S, Lienert TJ, Johnson MQ, DebRoy T. (2008), “An experimental and theoretical study of gas tungsten arc welding of stainless steel plates with different sulfur concentrations”, *Acta. Mater.* **56(9)**, 2133-2146
143. Weidlich N, Czerner S, Ostendorf A, Haferkamp H. (2007), “Analysis of the influence of alloying additions and process gases on the melt pool intrinsic dynamics of ferrous materials”, European congress and exhibition on advanced materials and processes, Nurnberg, Germany, 10-13, September, 2007
144. A Spiricon laser beam analyser and a silicon camera (model LBA-100A) was used. Because a focussed laser beam contains too much energy for the camera (i.e. it will burn through the camera) optical wedges or welding glasses have to be put between the laser beam and the camera. An optical wedge splits the laser beam, about 99% of the beam energy will reflect and only 1% reaches the camera in Kerstens, N.F.H. (2002), thesis, Nd:YAG laser welding of AA7075 high strength aluminium, Delft, The Netherlands.
145. Wu CS, Chen J, Zhang YM. (2007), “Numerical analysis of both front- and back-side deformation of fully-penetrated GTAW weld pool surfaces”, *Comp. Mater. Sci.* 2007, **39(3)**, 635-642
146. Chen Y, David SA, Zacharia T, Cremers CJ. (1998), “Marangoni convection with two free surfaces”, *Numer. Heat. Tr A-Appl.* **33(6)**, 599-620
147. Mills KC, Keene BJ, Brooks RF, Shirali A. (1998), “Marangoni effects in

- welding”, *Phil. Trans. R. Soc. Lond. A.*, **356**, 911-925
148. Turkdogan ET. (1996), “Fundamentals of steelmaking, the institute of materials”, 1996, The University press, Cambridge, p112
149. Arora A, Roy GG, DebRoy T. (2009), “Unusual wavy weld pool boundary from dimensional analysis”, *Scripta. Mater.* **60(2)**, 68-71
150. Belton GR. (1976), “Langmuir adsorption, the Gibbs adsorption isotherm, and interracial kinetics in liquid metal systems”, *Metal. Trans. B.* **7B**, 35-42
151. Xu G, Hu J, Tsai HL. (2008), “Three-dimensional modeling of the plasma arc in arc welding”, *J. Appl. Phys.* **104**, 103301
152. Mishra S, Debroy T. (2005), “A heat-transfer and fluid-flow-based model to obtain a specific weld geometry using various combinations of welding variables”, *J. Appl. Phys.* **98**, 044902
153. Anderson TD, DuPont JN, DebRoy T. (2010), “Origin of stray grain formation in single-crystal superalloy weld pools from heat transfer and fluid flow modelling”, *Acta. Mater.* **58 (4)**, 1441-1454
154. Cohen Stuart MA, Elmendorp JJ, Troian SM. (1990), “Dynamics of wetting: experimental findings in Hydrodynamics of dispersed media”, edited by Hulin JP, Cazabat AM, Guyon E, Carmona F. North-Holland, 29-43
155. de Gennes P. (1985), “Wetting: statics and dynamics”, *Rev. Mod. Phys.* **57**, 827-863
156. Teletzke GF, Davis HT, Scriven LE. (1987), “How liquids spread on solids”, *Chem. Eng. Commun.*, **55**, 1-6
157. Tanner LH. (1979), “The spreading of silicone oil drops on horizontal surfaces”, *J. Phys. D.* **12**, 1478-84
158. Lopez J, Miller CA, Ruckenstein E. (1976), “Spreading kinetics of liquid drops on solids”, *J. Colloid Interface Sci.* **56**, 460-468
159. Ralston J, Popescu M, Sedev R. (2008), “Dynamics of Wetting from an Experimental Point of View”, *Annual Review of Materials Research*, **38**, 23-43
160. Marmur A, Lelah MD. (1981), “The spreading of aqueous surfactant solutions on glass”, *Chem. Eng. Commun.* **13**, 133-143
161. Matar OK, Troian SM. (1999), “Spreading of a surfactant monolayer on a thin liquid film: onset and evolution of digitated structures”, *Chaos*, **9(1)**, 141-153
162. Matar OK. (1998), Ph.D. thesis, Princeton University, Princeton, NJ, USA
163. Afsar-Siddiqui AB, Luckhan PF, Matar OK. (2003), “The spreading of surfactant solutions on thin liquid films”, *Adv. Coll. Inter. Sci.*, **106**, 183-236

164. Cazabat AM, Heslot F, Troian SM, Carles P. (1990), "Fingering instability of thin spreading films driven by temperature-gradients", *Nature*. **346**, 824-826
165. Huppert HE. (1982), "Flow and instability of a viscous current a slope", *Nature*. **300**, 427-429
166. Williams R. (1977), "Advancing front of a spreading liquid", *Nature*. **266**, 153-154
167. DiPietro ND, Huh C, Cox RG. (1978), "The hydrodynamics of the spreading of one liquid on the surface of another", *J.Fluid.Mech.* 84,529
168. Carles P, Troian SM, Cazabat AM, Heslot FJ. (1990), "Hydrodynamic fingering instability of driven wetting films-hindrance by diffusion", *Phys. Condens. Matter*. **2**, 477-482
169. Barenblatt GI, Beretta E, Bertsch M. (1997), "The problem of the spreading of a liquid film along a solid surface: A new mathematical formulation", *Proc. Natl. Acad. Sci. UAS*, **94**, 10024-10030
170. Saffman PG, Taylor GI. (1958), "The penetration of a fluid into a porous medium or Hele shaw cell containing a more viscous fluid", *Proc. Royal Society*, 245, 312-329
171. Keller DL, McDonald MM, Heiple CR, Johns WL, Hofmann WE. (1990), "Wettability of brazing filler metals", *Weld. J.* **69(10)**, 31-34
172. Benhassine M, Saiz E, Tomsia AP, De Coninck J. (2010), "Role of substrate commensurability on non-reactive wetting kinetics of liquid metals", *Acta. Mater.* **58(6)**, 2068-2078
173. Klinger AJ, Leon-Patino CA, Drew RAL. (2010), "Wetting phenomena of Al-Cu alloys on sapphire below 800 degrees", *Acta. Mater.* **58(4)**, 1350-1360
174. Straumal BB, Kogtenkova O, Zieba P. (2008), "Wetting transition of grain-boundary triple junctions", *Acta. Mater.* **58(4)**, 36056(5), 925-933
175. Verhaeghe F, Craeghs T, Heulens J, Kruth JP. (2009), "A pragmatic model for selective laser melting with evaporation", *Acta. Mater.* **57(20)**, 6006-6012
176. Shen P, Fujii H, Nogi K. (2006), "Wettability of polycrystalline rutile TiO₂ by molten Al in different atmospheres", *Acta. Mater.* **54(6)**, 1559-1569
177. Hier-Majumder S, Leo PH, Kohstedt DL. (2004), "On grain boundary wetting during deformation", *Acta. Mater.* **52(12)**, 3425-3433
178. Dezellus O, Hodaj F, Rado C, Barbier JN, Eustathopoulos N. (2002), "Spreading of Cu-Si alloys on oxidized SiC in vacuum: experimental results and modelling", *Acta. Mater.* **50(5)**, 979-991
179. Levi G, Kaplan WD. (2002), "Oxygen induced interfacial phenomena during wetting of alumina by liquid aluminium", *Acta. Mater.* **50(1)**, 75-88

180. Frage N, Froumin N, Dariel MP. (2002), "Wetting of TiC by non-reactive liquid metals", *Acta. Mater.* **50(2)**, 237-245
181. Wynblatt P. (2000), "The effects of interfacial segregation on wetting in solid metal-on-metal and metal-on-ceramic systems", *Acta. Mater.* **48(18-19)**, 4439-4447
182. Voué M, De Coninck J. (2000), "Spreading and wetting at the microscopic scale: recent developments and perspectives", *Acta. Mater.* **48(18-19)**, 4405-4417
183. Swiler TP, Loehman RE. (2000), "Molecular dynamics simulations of reactive wetting in metal-ceramic systems", *Acta. Mater.* **48(18-19)**, 4419-4424
184. Rado C, Drevet B, Eustathopoulos N. (2000), "The role of compound formation in reactive wetting: the Cu/SiC system", *Acta. Mater.* **48(18-19)**, 4483-4491
185. Nakae H, Inui R, Hirata Y, Saito H. (1998), "Effects of surface roughness on wettability", *Acta. Mater.* **46(7)**, 2313-2318
186. Landry K, Rado C, Voitovich R, Eustathopoulos N. (1997), "Mechanism of reactive wetting: the questions of triple line configuration", *Acta. Mater.* **45(7)**, 3079-3085
187. Landry K, Eustathopoulos N. (1996), "Dynamics of wetting in reactive metal/ceramic systems: Linear spreading", *Acta. Mater.* **44(10)**, 3923-3932
188. Zhou XB, DeHosson JTM. (1996), "Reactive wetting of liquid metals on ceramic substrates", *Acta. Mater.* **42(2)**, 421-426
189. Rabkin E, Snapiro I. (2000), "Wetting of the low-angle grain boundaries", *Acta. Mater.* **48(18-19)**, 4463-4469
190. Palasantzas G, de Hosson JTM. (2001), "Wetting on rough surfaces", *Acta. Mater.* **49(17)**, 3533-3538
191. Dezellus O, Hodaj F, Eustathopoulos N. (2002), "Chemical reaction-limited spreading: the triple line velocity versus contact angle relation", *Acta. Mater.* **50(19)**, 4741-4753
192. Passerone A, Muolo ML. (2004), "Metal-ceramic interfaces: wetting and joining", *Int.J.Mater.Prod.Tec.* **20(5/6)**, 420-439
193. Saiz E, Tomsia AP, Cannon RM. (1998), "Wetting and work of adhesion in oxide/metal systems", *Ceramic Microstructure: Control at the atomic level*, Edited by Tomsia AP and Glaeser A. Plenum Press, New York
194. Saiz E, Tomsia AP, Cannon RM. (1998), "Ridging effects on wetting and spreading liquids on solids", *Acta. Mater.* **46(7)**, 2349-2361,
195. Saiz E, Tomsia AP, Cannon RM. (2001), "Triple line ridging and attachment in high temperature wetting", *Scripta. Mater.* **44**, 159-164

196. Saiz E, Tomsia AP. (2005), "Kinetics of high-temperature spreading", *Curr. Opin. Solid. St. M.* **9**, 167-173
197. Saiz E, Cannon RM, Tomsia AP. (2000), "Reactive spreading: Adsorption, ridging and compound formation", *Acta. Mater.* **48**, 449-4462
198. For most high temperature system, the experimental temperature are typically $\geq 0.2 - 0.5T_m$ which leads to local diffusion. Under these conditions, a small ridge generated by local deformation of the solid surface, will eventually develop at the triple junction, the ridge is a small sharp 'bump' like shape (see solid shape at the triple line of Figure 6-1b). The mechanism is analogous to the grooves found at the grain boundaries.
199. Yin L. et.al (2009), "Reactive wetting in metal-metal system", *J. Phys. Condens. Matter.* **21**, 414120
200. Rauch N. (2005), High-temperature spreading kinetics of metals (Ph. D thesis), University Stuttgart.
201. Young T. (1805), "An essay on the cohesion of fluids", *Philos. Trans. Roy. Soc. London.* **95**, 65-87
202. Smith CS. (1948), "Grains, phases and interfaces: An interpretation of microstructure", *Trans. AIME.* **175**, 15-51
203. Ahmad J., Hansen RS. (1972) *J. Colloid. Int. Sci.* **38**, 601 and Borgas ME, Grotberg JB. (1988) *J. Fluid. Mech.* **193**, 151; $n=1/4, 1/2$ shown in Gaver DP, Grotberg JB. (1992), *J. Fluid. Mech.* **240**, 259; and $n=1/4$ was validated in Dussaud AD, Matar OK, Troian SM. (2005), *J. Fluid. Mech.* **544**, 23; $n=1/2, 1/3, 1/4$ predicted in Jensen OE, Grotberg JB. (1993) *Phys. Fluids* **A5**, 58. agree with Espinosa FF. (1991) *Adv. Biochem. ASME* **20**, 571. and $n=1/4$ in Melo F, Joanny JF, Fauve S. (1989) *Phys. Rev. Lett.* **63**, 18.
204. Mullins WW. (1956), "Two-Dimensional motion of idealized grain boundaries", *J. Appl. Phys.* **27(8)**, 900-904
205. Mullins WW. (1957), "Theory of thermal grooving", *J. Appl. Phys.* **28(3)**, 333-339
206. Mullins WW. (1958), "The effect of thermal grooving of grain boundary motion", *Acta. Metal.* **6**, 414-427
207. According to the kinetics of segregation by McLean's approach, solute atoms are assumed to segregate to a grain boundary from two infinite half crystal of uniform solute content or to a surface from on infinite half crystal. In Mclean D. (1957), *Grain boundaries in metal*, (Oxford Univ. Press).
208. Marmur A, Lelah MD. (1981), "The spreading and aqueous surfact solutions on glass", *Chem. Eng. Commun.* **13**, 133-143
209. Troian SM, Wu XL, Safran SA. (1989), "Fingering instability in thin wetting

Reference

- films”, *Phys. Rev. Lett.* **63**, 1496-1499
210. Troian SM, Herbolzheimer E, Safran S. (1990), “Model for the fingering instability of spreading surfactant drops”, *Phys. Rev. Lett.* **65**, 333-336
211. Cazabat AM, Heslot F, Troian SM, Carles P. (1990), “Fingering instability of thin spreading films driven by temperature gradients”, *Nature*. **346**, 824-826
212. Carles P, Cazabat AM, Kolb E. (1993), “The spreading of films by surface tension gradients”, *Colloids surface A*. **79**, 65-70
213. Matar OK, Craster RV. (2009), “Dynamics of surfactant-assisted spreading”, *Soft. Matter*. **5**, 3801-3809
214. Ludviksson V, Lightfoot EN. (1971), “The dynamics of thin liquid films in the presences of surface-tension gradients”, *AICHE J.* **17**, 1166-1173
215. Iwamoto C, Tanaka SI. (2002), “Atomic morphology and chemical reactions of the reactive wetting front”, *Acta. Meter.* **50**, 749-755
216. Nomura M, Iwamoto C, Tanaka SI. (1999), “Nanostructure of wetting triple line in a Ag-Cu-Ti/Si₃N₄ reactive system”, *Acta. Meter.* **47**, 407-41
217. Qian H, Luo J. (2008), “Nanoscale surficial films and a surface transition in V₂O₅-TiO₂-based ternary oxide systems”, *Acta. Meter.* **56(17)**, 4702-4714
218. Saiz E, Tomsia AP. (2004), “Atomic dynamics and Marangoni films during liquid-metal spreading”, *Nature*. **3**, 903-909
219. Saffman PG, Taylor GI. (1958), “The penetration of a fluid into a porous medium or Hele_shaw cell containing a more ciscous fluid”, *Proc. Royal Society*, 245, 312-329

Summary

Understanding the fluid flow in weld pools contributes significantly toward controlling the heat distribution in the base material and the mass distribution of molten base and additive materials. Currently, most investigations focus primarily on numerical models, due to the experimental difficulties associated with the challenging environment in and around the weld pool. Numerical simulations based on computational fluid dynamics are currently addressing the dynamic behaviour of weld pools, such as melting, solidification, temperature and velocity fields; these results provide information about conditions inside the weld pool that is impossible to gain experimentally. However, there is still a shortage of experimental validation to support these models. In this thesis, experimental methods are applied to study the fluid flow of the weld pool in both arc and laser generated weld pools.

Experimental measurements based on visualization of the weld pool surface have been undertaken to provide both the flow patterns and velocity fields. A high-speed visualization system was built to observe the dynamic development of weld pools. In order to avoid extraneous influences due to the addition of tracking particles, the natural oxide particles on the metal surface were used to visualize the surface flow motion. Compared with traditional methods that only track a few particles, the partial image velocimetry (PIV) approach adopted in this work can provide the whole velocity field on the surface. Results indicate that particle image velocimetry can successfully be applied to compute the quantitative flow velocities on the weld pool.

Although particle image velocimetry works well for a flat surface, errors arise when strong surface curvature or oscillation occur; for example, when inward flow induces a highly concave surface in the middle of the weld pool during laser spot welding. Thus, three-dimensional measurement is required for some cases. To obtain three-dimensional information, at least two synchronized images are required from two different viewpoints. In order to avoid the complexities and high cost of a multi-camera experimental system, two groups of mirrors were added in front of a single high-speed camera. A mathematical transform based on a pinhole model is used to reconstruct the three-dimensional partial displacements. The case tested for a laser spot weld provides a new method to measure the flow velocities on a strongly curved surface.

Welding conditions examined include cases both with and without surface active agents. For stainless steel arc welding without a surface active agent, the flow is mainly outward, but shows strong oscillations. For stainless steel arc welding in the presence of a surface-active agent, an inward flow is generated leading to the formation of an interface where liquid from the weld pool boundary converges. The interface is quite unstable and induces frequent vortex shedding at the rear of a travelling weld pool.

For arc welding, there are four kinds of forces that influence liquid metal flow; they are the Lorentz, Marangoni, arc shear, and buoyancy forces; of these, surface tension (Marangoni force) plays the dominant role for the liquid iron system. These forces work

together to induce quite complex flow motion and it is difficult to separate individual contributions by experimental means. To minimize the number of significant forces, a stationary laser spot weld was adopted to examine the influence of Marangoni driven flow. A defocused laser spot was used to heat a small piece of stainless steel whilst avoiding keyhole formation or weld pool disturbance due to excessive vaporisation.

Normally, two kinds of flow directions occur during welding, they are an outward flow, driven by a negative surface tension gradient and an inward flow driven by a positive surface tension gradient. These two basic flow directions can produce complex patterns, such as multi-cellular flows and vortex flows when subject to appropriate boundary conditions.

The surface tension of liquid stainless steel and its temperature coefficient are a function of temperature and surface active agent concentration. Sulphur and oxygen are two common active agents of interest during welding; they play a similar role in influencing surface tension and its temperature coefficient. Sulphur is found in the base metal or in the filler materials, whilst oxygen comes mainly from the ambient environment or the shielding gas. The influence of sulphur has been studied extensively elsewhere for both similar and dissimilar metal welding; however, in the present study sulphur is considered to have a constant concentration in the liquid metal system (~0.004 wt. %) exerting only minimal influence on the surface tension or surface tension gradient. Oxygen influences convection and diffusion as well as oxidation and its interaction with the weld pool is thus more complex than that of sulphur. Despite this, in most reported works the assumption is made that oxygen concentration is constant. In this work, the oxygen influence is studied by controlling the oxygen additions to the shielding environment, where the level can be controlled from a few parts per million to atmospheric levels. A high-speed camera system was employed to examine the dynamic development of the weld pool.

Some interesting phenomena were observed when different oxygen levels were examined under the same laser illumination conditions. A flow transition from outward to inward flow is observed with increasing oxygen concentration in the shielding environment. This is related to the variation of the temperature coefficient of surface tension, which is increased from negative to positive. In addition, experimental results show that the flow transition only occurs when the oxygen concentration in the environment is higher than some critical value. Oxidization changes the surface absorption coefficient and leads to increased energy absorption at higher levels of oxidation. Experiments show that high oxygen levels result in a larger weld pool and the weld pool is deeper when inward flow occurs. The time to onset of melting for a lower oxygen concentration is greater.

Experimental observations also indicate that the flow is quite unstable and asymmetric, especially during inward flow when the oxygen concentration is high enough to generate a positive surface tension temperature coefficient. Inward flow brings liquid to the center of the weld, any slight disturbance can generate asymmetry and rotational flow. Visualizations show that the rotation can be clockwise or counter clockwise. Such behaviour has not been considered in the published numerical models.

The Peclet number of a weld pool is in the order of 10^6 - 10^8 , indicating that the oxygen distribution is mainly influenced by convection rather than diffusion. Post solidification measurement of the oxygen distribution by Electron Probe Microanalysis indicates that oxygen is almost homogeneously distributed in the weld pool in most of cases.

Fluid flow in the weld pool is influenced by the closely coupled evolution of oxygen concentration and temperature. Individual contributions are separated mathematically in the present work, which considers three different development paths of the oxygen concentration and temperature. It is shown that variation of oxygen concentration always makes a much larger contribution than temperature on the surface tension gradient. Thus, variations in oxygen concentration play the main role in changing the flow pattern from an outward to an inward flow.

An unavoidable occurrence during any welding is the appearance of a triple line; *i.e.*, the contact line between the solid, liquid and vapour phases. Normally, the position of the triple line is the weld pool boundary. However, this can change when the laser energy density is low. A number of cases were examined with increasing oxygen concentration in the shielding environment. Experimental measurements on these solidified samples suggest that the melting starts from grain boundaries. A liquid net can be generated when the bulk liquid spreads on the partly melted surface. With increasing oxygen concentration in the shielding environment, the wettability of liquid metal is also improved and finally, the liquid net merges to form a thin film. Experimental visualization shows that a thin film with a thickness of around 3 microns can spread far ahead of the bulk liquid, and the triple line spreads much faster than the boundary of the weld pool.

Following the thin precursor film, bulk liquid spreading on the film can generate finger-like flows around the interface of the weld pool and precursor film. This phenomenon is very similar to fingering instabilities occurring in organic systems at low temperatures, which has been explained in terms of applied forces, surface shear stresses and / or surfactant diffusion.

Fingering instability had not previously been reported for a high-temperature liquid metal system. The experimental results obtained in the present work are ascribed to opposing Marangoni forces, which appear at the interface between the bulk liquid and the precursor film. The liquid metal flows outward in the bulk area, where a negative surface tension gradient is induced by temperature differences between the centre and the edge of the melt pool. However, within a very small area outside the bulk liquid, the liquid metal flows inward due to a large gradient in the oxygen concentration. Measurements indicated that the oxygen concentration in the precursor film is much higher than that in the bulk liquid area. This is explained by oxygen redistribution in the larger volume of the weld pool by convection. The rate of oxygen concentration increase in the precursor film is higher than that of the bulk liquid due to the absence of such a substantial convection.

The thickness of the precursor film rules out consideration of van der Waals forces, so the Marangoni forces acting on the interface of bulk liquid and precursor film are the main factors influencing fingering instabilities in this liquid metal system. Further investigations are needed to understand the mechanism in greater detail.

The general conclusions from the experimental study provides some suggestions for understanding the fluid flow in the weld pool, such as flow asymmetry, rotational flow and interface instabilities. For example, the interface instabilities can affect the energy and mass distribution. Describing these instabilities numerically requires three dimensional flow models. Moreover, the current experimental results question the validity of works where the surfactant concentration is assumed to be constant in the weld pool without consideration of dynamic diffusion and convection. This work has focused on experimental measurement of the fluid dynamics of weld pools, and current results provide a number of validation cases for further numerical simulations.

Samenvatting

Het begrijpen van de vloeistofstroming in lasbaden draagt bij tot een betere controle over de warmteverdeling in het basismateriaal en het menggedrag van gesmolten basismateriaal en toevoegmateriaal. Momenteel concentreert het meeste onderzoek zich op het numeriek modelleren van deze aspecten. Dit is te wijten aan de experimentele moeilijkheden gerelateerd aan de uitdagende omgeving in en rond het lasbad. Numerieke simulaties gebaseerd op vloeistofdynamica richten zich op het dynamische gedrag van het lasbad, zoals het smelten en stolling, en de temperatuur- en snelheidsvelden in het lasbad. De resultaten verschaffen informatie over de omstandigheden in het lasbad die onmogelijk experimenteel bepaald kunnen worden. Er is echter nog steeds een gebrek aan experimentele onderbouwing van deze modellen. In dit onderzoek zijn experimentele methoden toegepast om vloeistofstromingen in het lasbad, zowel voor boog- als voor laserlassen, te bestuderen.

Experimentele metingen gebaseerd op visualisatie van het lasbadoppervlak zijn uitgevoerd om stromingspatronen en snelheidsvelden te bepalen. Een hoge-snelheid visualisatie systeem is opgebouwd om de dynamische ontwikkeling van het lasbad te observeren. Om de invloed van externe 'tracking' deeltjes op de vloeistofstroming te voorkomen, zijn de natuurlijk aanwezige oxydedeeltjes op het lasbadoppervlak gebruikt om de oppervlaktestroming te visualiseren. Vergeleken met traditionele methoden, die slechts een klein aantal deeltjes volgen, kan de in dit onderzoek toegepaste 'patial image velocimetry' methode het gehele snelheidsveld aan het oppervlak bepalen. De resultaten tonen dat 'patial image velocimetry' succesvol kan worden toegepast om de kwantitatieve stromingssnelheden aan het lasbadoppervlak te kunnen berekenen.

Hoewel 'patial image velocimetry' goed werkt voor vlakke oppervlakken, ontstaan fouten ten gevolge van oppervlaktekromming of door het optreden van oscillaties. Dit is bijvoorbeeld het geval bij een naar binnen gerichte stroming tijdens laserpuntlassen, waarbij een zeer concaaf oppervlak ontstaat in het midden van het lasbad. Daarom is een driedimensionale meting onder bepaalde/sommige omstandigheden noodzakelijk. Om driedimensionale informatie te verkrijgen, zijn tenminste twee gesynchroniseerde beelden vanuit twee verschillende gezichtspunten nodig. Om de complexiteit en de hoge kosten van een multi-camerasysteem te vermijden zijn twee groepen spiegels geplaatst voor één enkele hoge-snelheidscamera. Een mathematische transformatie, gebaseerd op een 'pinhole' model, is toegepast om driedimensionale partiële verplaatsingen te kunnen reconstrueren. Dit levert een nieuwe methode op om stromingssnelheden te meten voor sterk gekromde oppervlakken. Dit is getest tijdens tijdens het laserpuntlassen.

De bestudeerde lasomstandigheden omvatten zowel het lassen zonder als met het gebruik van oppervlakte-actieve elementen. Tijdens het booglassen van roestvast staal zonder oppervlakte-actieve stoffen is de stroming hoofdzakelijk naar buiten gericht. Als roestvast staal wordt gelast in de aanwezigheid van oppervlakte-actieve elementen, wordt een naar binnen gerichte stroming verkregen. Deze naar binnen gerichte stroming leidt tot de

vorming van een grensvlak op de plaats waar de vloeistof van de lasbadgrenslaag samenkomt. Het grensvlak is nogal instabiel en induceert regelmatig wervelingen, die zich verspreiden naar de achterzijde van een voortbewegend lasbad.

Bij het booglassen beïnvloeden vier krachten de vloeistofstroming. Dit zijn de Lorentzkracht, de Marangonikkracht, een afschuifkracht van de boog en de opwaartse kracht (kracht ten gevolge van verschillen in dichtheid). Van deze krachten speelt de oppervlaktespanning (Marangonikkracht) een dominante rol in het vloeibaar ijzer systeem. Al deze krachten genereren gezamenlijk een complexe vloeistofstroming, waarvan de individuele bijdragen moeilijk te scheiden zijn door experimentele middelen. Om het aantal betrokken krachten te verminderen is het laserpuntlassen uitgevoerd in een stationair situatie, waardoor de invloed van de marangonistroming bestudeerd kan worden. Een gedefocuseerde laserspot is toegepast om een klein gedeelte van het roestvast staal te smelten, waarbij de verstoring van het lasbad door de vorming van een sleutelgat (key hole) of door excessieve verdamping voorkomen is/werd.

Normaal gesproken kunnen twee stromingsrichtingen tijdens het lassen optreden: een naar buiten gerichte stroming door een negatieve oppervlaktespanningsgradient en een naar binnen gerichte stroming door een positieve oppervlaktespanningsgradient. Deze twee basisstromingsrichtingen kunnen onder bepaalde randvoorwaarden complexe patronen opleveren, zoals meervoudige cellulaire stromingen en wervelingen.

De oppervlaktespanning van vloeibaar roestvast staal en haar temperatuurcoëfficiënt zijn een functie van de temperatuur en de concentratie van oppervlakte-actieve elementen. Zwavel en zuurstof zijn twee algemene actieve elementen die van belang zijn voor het lassen; zij spelen een gelijke/gelijkwaardige rol ten aanzien van de beïnvloeding van de oppervlaktespanning en haar temperatuurcoëfficiënt. Zwavel wordt aangetroffen in het basismateriaal of in het toevoegmateriaal, terwijl zuurstof hoofdzakelijk uit de omgeving of het beschermgas komt. De invloed van zwavel is veelvuldig bestudeerd voor zowel het lassen van gelijksoortige als ongelijksoortige metalen. In de huidige studie is echter verondersteld dat het zwavelgehalte (~0.004 wt. %) constant is in het vloeibare metaal en dat het slechts een minimaal effect heeft op de oppervlaktespanning of de oppervlaktespanningsgradiënt. Zuurstof beïnvloedt zowel convectie en diffusie als oxydatie en de interactie hiervan met het lasbad en is daarom meer complex dan de invloed van zwavel. Ondanks dat, wordt in het merendeel van het gepubliceerde werk aangenomen dat het zuurstofgehalte constant is. In dit onderzoek is de invloed van zuurstof bestudeerd door gecontroleerde zuurstoftoevoegingen aan het beschermgas. Het gehalte is gevarieerd van een paar deeltjes per miljoen tot atmosferische concentraties. Een hoge-snelheid camera systeem is gebruikt om de dynamische ontwikkeling van het lasbad te bestuderen.

Enkele interessante fenomenen werden waargenomen bij het bestuderen van het effect van verschillende zuurstofgehalten bij gelijke laserbelichtingscondities. Een overgang van een naar buiten naar een naar binnen gerichte stroming wordt waargenomen bij hogere zuurstofgehalten in het beschermgas. Dit is gerelateerd aan de variatie van de temperatuurcoëfficiënt van de oppervlaktespanning, die verandert van negatief naar positief. Tevens laten de experimenten zien dat de omkering van de vloeistofstroming

alleen plaats vindt als een bepaalde kritische waarde van de concentratie wordt overschreden. Oxydatie verandert de oppervlakteabsorptiecoëfficiënt en leidt tot een verhoogde energieopname met toenemende oxidatiegraad. Experimenten tonen aan dat hogere zuurstofniveaus resulteren in een groter lasbad, dat tevens dieper is als een naar binnen gerichte stroming optreedt. De tijdduur tot smelten is langer bij lagere zuurstofconcentraties.

Experimentele waarnemingen wijzen er tevens op dat de stroming instabiel en asymmetrisch is, vooral bij een naar binnen gerichte stroming als de zuurstofconcentratie voldoende hoog is om een positieve oppervlaktespansingsgradiënt te bewerkstelligen. Als de vloeistofstromen convergeren in het centrum van het lasbad, kan elke kleine verstoring asymmetrie of een rotationele stroming veroorzaken. Er zijn zowel (rechtsom als linksom draaiende) stromingen met de wijzers van de klok mee, als tegen de wijzers van de klok in waargenomen. Dit gedrag wordt niet in overweging genomen in de gepubliceerde numerieke modellen.

Het Peclet getal van een lasbad ligt in de orde van grootte van 10^6 - 10^8 , hetgeen impliceert dat de zuurstofverdeling hoofdzakelijk wordt beïnvloed door convectie in plaats van diffusie. Metingen van de verdeling van het zuurstofgehalte na stolling, door middel van Electron Probe Microanalyse, geven in bijna alle gevallen een homogene verdeling van zuurstof in het lasbad aan.

De vloeistofstroming in een lasbad wordt beïnvloed door het sterk gekoppelde effect van de ontwikkeling van de zuurstofconcentratie en de temperatuur. Individuele bijdragen zijn in deze studie afzonderlijk berekend. Deze berekeningen beschouwen drie verschillende trends van de zuurstofconcentratie in combinatie met de temperatuur. Het is aangetoond dat de variatie in zuurstofconcentratie in vergelijking tot de temperatuur altijd een veel grotere bijdrage levert op de oppervlaktespansingsgradiënt. De variatie in zuurstofconcentratie speelt dus de belangrijkste rol in de verandering van het stromingspatroon van een naar buiten gerichte naar een naar binnen gerichte stroming.

Het optreden van een driefasenlijn, de contactlijn tussen de vaste, de vloeibare en de dampfase, is bij het lassen onvermijdelijk. Normaal gesproken is de positie van deze contactlijn op het grens van het lasbad. Dit kan echter veranderen als de vermogensdichtheid van de laser laag is. Een aantal gevallen is onderzocht waarbij de zuurstofconcentratie in het beschermgas is verhoogd. Metingen aan de gestolde proefstukken tonen dat smelten start aan de korrelgrenzen. Een vloeibaar netwerk kan gevormd worden als de bulkvloeistof zich uitspreidt over de gedeeltelijk gesmolten zone. Bij toename van de zuurstofconcentratie in het beschermgas zal de bevochtiging van het vloeibare metaal ook toenemen en zal het vloeistofnetwerk een dunne laag gaan vormen. Experimenteel is aangetoond dat een dunne vloeistoffilm, met een dikte van 3 micron, zich ver voor het bulk van de vloeistof vormt en dat de driefasenlijn zich sneller uitspreidt dan de grens van het lasbad.

De vorming van de vloeistoffilm wordt gevolgd door het optreden van vingervormige stromingen aan het grensvlak van het lasbad en de film. Dit fenomeen is eender aan de vingervormige instabiliteiten die optreden in organische systemen bij lage temperatuur en worden verklaard in termen van opgelegde kracht, schuifspanningen en/of diffusie aan het

oppervlak.

Vingervormige instabiliteiten zijn nog niet gerapporteerd voor vloeibare metalen op hoge temperatuur. De experimentele resultaten van het huidige onderzoek worden toegeschreven aan elkaar tegenwerkende Marangonikrachten, die optreden aan het grensvlak tussen de bulkvloeistof en de film. De vloeistof is naar buiten gericht in de bulk, waar een negatieve oppervlaktespanningsgradiënt wordt verkregen door het temperatuurverschil tussen het centrum en de rand van het lasbad. In de zeer smalle zone buiten de bulkvloeistof is de vloeistofstroming echter naar binnen gericht ten gevolge van de hoge gradiënt in de zuurstofconcentratie. Metingen tonen dat de zuurstofconcentratie in de film veel hoger is dan in de bulkvloeistof. Dit kan worden verklaard door de herverdeling van zuurstof in het grote volume van het lasbad door convectie. De snelheid waarmee de zuurstofconcentratie in de film toeneemt is groter dan die in de bulkvloeistof door de afwezigheid van substantiele convectie.

De dikte van de film sluit een overweging met betrekking tot de invloed van van der Waalskrachten uit. De Marangonikrachten die op het grensvlak van de bulkvloeistof en de film werken zijn de belangrijkste invloedsfactoren ten aanzien van de vingervormige instabiliteiten in dit vloeistofstelsel. Verder onderzoek is noodzakelijk om dit mechanisme in meer detail te begrijpen.

De algemene conclusies van deze experimentele studie geven enkele aanwijzingen voor het begrijpen van de vloeistofstroming in het lasbad, zoals asymmetrie, rotationele stroming en grensvlakinstabiliteiten. De grensvlakinstabiliteiten kunnen bijvoorbeeld de energie- en massaverdeling beïnvloeden. Het numeriek beschrijven van deze instabiliteiten vereist driedimensionale stromingsmodellen. Tevens trekken de huidige experimentele resultaten de geldigheid van onderzoek in twijfel, waarbij de concentratie van oppervlakte-actieve elementen in het lasbad als constant worden verondersteld zonder dynamische diffusie of convectie te overwegen. Dit onderzoek heeft zich gericht op experimentele metingen van de vloeistofdynamica van lasbaden en de resultaten geven een aantal cases voor validatie van toekomstige numerieke simulaties.

List of publications

Journal articles:

Zhao CX, Song GM, Richardson IM, Saldi Z, Kenjeres S, Kleijn CR. (2011) Marangoni film spreading and fingering instabilities of liquid metal, (Submitted)

Song GM, Li SB, Zhao CX, Sloof WG, Van der Zwaag S, Pei YT, De Hosson J Th M, (2011) Ultra-high temperature ablation behavior of Ti₂AlC ceramics under an oxyacetylene flame, *J. Eur. Ceram. Soc.*, **31**:855

Zhao CX, Kwakernaak C, Pan Y, Richardson IM, Saldi Z, Kenjeres S, Kleijn CR. (2010) The effect of oxygen on transitional Marangoni flow in laser spot welding. *Acta Mater.* **58**(19):6345

Zhao C.X., Richardson I.M., Kenjeres S., Kleijn C.R., Saldi Z. (2009) A stereo vision method for tracking particle flow on the weld pool surface, *J.Appl.Phys.*, **105**:123104

Zhao CX, Richardson IM, Pan Y, (2009) Liquid metal flow behaviour during conduction laser spot welding, *Welding in the World*, **53**:217

Zhao CX, Steijn VV, Richardson IM, Kleijn CR, Kenjeres S, Saldi Z. (2009) Unsteady interfacial phenomena for weld pool inward flow with an active surface oxide *Sci.Technol.Weld.Joi.*, **14**(2):132

Xu JL, Zhao CX. (2007), Two-dimensional numerical simulations of shock waves in micro convergent–divergent nozzles, *Int.J.Heat.Mass.Tran.*, **50**:2434

Conference articles:

Song GM, Li SB, Zhao CX, Sloof WG, van der Zwaag S, Pei YT, Th. M. De Hosson J. (2010) Characterization of Ultra-High Temperature Ablation of Ti₂AlC Ceramics under Oxyacetylene Flame, Proceeding of 7th International Conference on High Temperature Ceramic Matrix Composites (HT-CMC7), September 20–22, Bayreuth, Bavaria, Germany

Saldi Z, Kidess A, Kenjeres S, Kleijn C, Zhao C, Richardson IM. (2010), Marangoni driven free surface microflows in liquid metal weld pools, Proceedings of the 2nd european conference on microfluidics, December 8-10, Toulouse, France

Zhao CX, Richardson IM, Song GM, Pan Y, Kenjeres S, Saldi ZS, Kleijn CR. (2010) Unstable contact line spreading o liquid stainless steel, Triple lines in metals and ceramics-a symposium in honor of Nicolas Eustathopoulos, Center de Physique des Houches, May 25-28, des Houches, France

Zhao CX, Richardson IM. (2009) Complex flow motions in laser welding, 40th AIAA plasma dynamics and lasers conference, June 22-25, San Antonio, Texas, USA

Saldi ZS, Zhao C, Kenjeres S, Richardson IM, Kleijn CR. (2009) Numerical and experimental investigations of marangoni driven flow reversals in liquid steel welding pools. 7th World Conference on Experimental Heat Transfer, Fluid Mechanics and Thermodynamics, June 28–July 03, Krakow, Poland

Saldi ZS, Zhao C, Kenjeres S, Richardson IM, Kleijn CR. (2009) Numerical and experimental studies of free surface flow reversals in liquid steel welding pools. 9th internal seminar numerical analysis of weldability, September 28-30, Graz, Austria

Zhao CX, Richardson IM, Kleijn C, Kenjeres S, Saldi Z. (2008), A stereo vision visualization method in welding, International conference of numerical analysis and applied mathematics, September 16-20, Kos, Greece

Zhao CX, Steijn VV, Richardson IM, Saldi Z, Kleijn CR. (2008) Experimental observation for weld pool surface velocity field of GTAW, 8th Trend in welding research conference, 201-210 June 1-6, Pine mountain, Georgia, USA

Acknowledgements

During the past four years, I have been supported by lots of kind people, this thesis would have never been finished without their help. Here I can thank everyone that made this thesis possible.

First of all, I express my deep appreciation to my supervisor Prof. Ian M Richardson, who brought me into this totally new research field, and taught me how to understand the complex mechanisms behind the experimental phenomena. I also give my special thanks to Prof. Chris R Kleijn and Dr Sasa Kenjeres, whose suggestions and comments always lead me to the theoretical analysis.

Many thanks for the cooperation with Zaki S Saldi, who has worked with me on this project during the last four years; it is the longest cooperation I have ever participated in. I hope we will have chance to cooperate with each other in the future. Thanks for the help from Dr. Volkert van Steijn, who applied the PIV method to measure the weld pool flow. I obtained the optical visualisation method under the help of Dr. Yudodibroto, thanks for his kind explanation and introduction.

Dr. Marcel Hermans gave many useful comments on this project in the last four year, his kind comments made this work deeper. I also express my thanks to Dr. Kees Kwakernaak on EPMA measurements, and Dr. Guiming Song on SEM-EDS measurements, their contributions on element distributions made this work stronger.

Our industrial partner Tata steel supported this project; I express my appreciation for the comments from Dr. Rene Duursma, Dr. Tony van der Veldt, Dr. Ellen van de Aa, Mr. Nick den Uijl, Dr. Dirk van der Plas, Dr. Eelco van Vliet, Dr. Andrew Norman and Dr. Sullivan Smith.

My thanks are also given to Jurriaan Slingerland for his technical support in the past four years, his continuous support contributes to every part of this thesis; and thanks to Frans Bosman who built up the gym in our department, where I can relax and come back to work with full energy. Our secretary Anneke van Veen provides me with lots of good tips on how to adapt to life quickly in Holland.

I am proud of the warm friendship from my colleagues Lucia Nicola, Ton Riemslog, Michael Janssen, Xu Cheng, Jianjun Ding, Menas Wibowo, Yu Pan, Masoud Pazooki, Sepideh Ghodrat, Martin Janssen, Murugaiyan Amirthalingam, Vera Popovich, Wei Ya, Yunhe Zhang, Fengwei Sun, Rangan Kaushik Dutta, He Gao, Aristeidis Katsiorchis, Liliang Wang, Zhan Zhang, Qingshi Song, Yingxia Qu and Zhiguang Huan.

Last but not the least, I express my faithful thanks for the love and support from my family, especially to my wife Hui Li, who always gives me encouragement and advice.

Chuangxin Zhao

Delft, March, 2011

Curriculum Vitae

Chuang-Xin Zhao was born on Oct 22nd, 1980 in Shangdu, Inner Mongolia, China. He received his primary education in Wuyegou. After finishing his secondary education in Shangdu he started his college education at Central South University, Changsha, Hunan, where he received his Bachelor degree in Thermal Engineering in 2003. From 2003 to 2004, he spent one year on a master education in University of Science and Technology of China, Hefei, China. His master thesis was done in Guangzhou Institute of Energy Conversion, Chinese Academy of Sciences, Guangzhou, Guangdong.

From Oct 2006, he was enrolled as a PhD employee by the Material Innovation Institute (M2i), the former Netherlands Institute for Metal Research (NIMR), and started his research in experimental fluid dynamics of weld pools under the supervision of Prof. Ian. M. Richardson at Delft University of Technology, The Netherlands.